ABSTRACT

CHARACTERISTICS OF NANOCOMPOSITES AND SEMICONDUCTOR HETEROSTRUCTURE WAFERS USING THz SPECTROSCOPY

by
Hakan Altan

All optical, THz-Time Domain Spectroscopic (THz-TDS) methods were employed towards determining the electrical characteristics of Single Walled Carbon Nanotubes, Ion Implanted Si nanoclusters and $Si_{1-x}Ge_x$, HFO_2, SiO_2 on p-type Si wafers.

For the nanoscale composite materials, Visible Pump/THz Probe spectroscopy measurements were performed after observing that the samples were not sensitive to the THz radiation alone. The results suggest that the photoexcited nanotubes exhibit localized transport due to Lorentz-type photo-induced localized states from 0.2 to 0.7THz. The THz transmission is modeled through the photoexcited layer with an effective dielectric constant described by a Drude + Lorentz model and given by Maxwell-Garnett theory. Comparisons are made with other prevalent theories that describe electronic transport. Similar experiments were repeated for ion-implanted, 3-4nm Si nanoclusters in fused silica for which a similar behavior was observed.

In addition, a change in reflection from $Si_{1-x}Ge_x$ on Si, 200mm diameter semiconductor heterostructure wafers with 10% or 15% Ge content, was measured using THz-TDS methods. Drude model is utilized for the transmission/reflection measurements and from the reflection data the mobility of each wafer is estimated. Furthermore, the effect of high-κ dielectric material (HfO_2) on the electrical properties of p-type silicon wafers was characterized by utilizing non-contact, differential (pump-pump off)

spectroscopic methods to differ between HfO_2 and SiO_2 on Si wafers. The measurements are analyzed in two distinct transmission models, where one is an exact representation of the layered structure for each wafer and the other assumed that the response observed from the differential THz transmission was solely due to effects from interfacial traps between the dielectric layer and the substrate. The latter gave a more accurate picture of the carrier dynamics. From these measurements the effect of interfacial defects on transmission and mobility are quantitatively discussed.

CHARACTERISTICS OF NANOCOMPOSITES AND SEMICONDUCTOR HETEROSTRUCTURE WAFERS USING THz SPECTROSCOPY

by
Hakan Altan

A Dissertation
Submitted to the Faculty of
New Jersey Institute of Technology and
Rutgers, The State University of New Jersey - Newark
in Partial Fulfillment of the Requirements for the Degree of
Doctor of Philosophy in Applied Physics

Federated Physics Department

January 2005

APPROVAL PAGE

CHARACTERISTICS OF NANOCOMPOSITES AND SEMICONDUCTOR HETEROSTRUCTURE WAFERS USING THz SPECTROSCOPY

Hakan Altan

Dr. John F. Federici, Dissertation Advisor — Date
Professor of Physics, NJIT, Newark, NJ

Dr. Haim Grebel, Committee Member — Date
Professor of Electrical and Computer Engineering and Director, Electronic Imaging Center, NJIT, Newark, NJ

Dr. Andrei Sirenko, Committee Member — Date
Assistant Professor of Physics, NJIT, Newark, NJ

Dr. Zafar Iqbal, Committee Member — Date
Research Professor of Chemistry and Environmental Sciences, NJIT, Newark, NJ

Dr. Oleg Mitrofanov, Committee Member — Date
Member of Technical Staff, Bell Laboratories, Lucent Technologies, Murray Hill, NJ

Dr. Martin Schaden, Committee Member — Date
Assistant Professor of Physics, Rutgers, The State University of New Jersey – Newark, NJ

BIOGRAPHICAL SKETCH

Author: Hakan Altan

Degree: Doctor of Philosophy

Date: January 2005

Undergraduate and Graduate Education:

- Doctor of Philosophy in Applied Physics,
  New Jersey Institute of Technology, Newark, NJ, 2005

- Dual Bachelor of Science in Physics and Astronomy,
  State University of New York at Stony Brook, Stony Brook, NY, 1998

Major: Applied Physics

Presentations and Publications:

H. Altan, A. Lan, F. Huang, J. F. Federici, and H. Grebel, "Optical and electronic characteristics of single walled carbon nanotubes and silicon nanoclusters by terahertz spectroscopy," J. Appl. Phys 96 (11), 6685 (2004).

H. Altan, A. Sengupta, J. F. Federici, and H. Grebel, "Characteristics of 200mm diameter HfO_2 and SiO_2 on p -type silicon wafers using THz spectroscopy," (Under Review).

H. Altan, J. F. Federici, and H. Grebel, "Hole Mobility of 200mm Diameter $Si_{1-x}Ge_x$ Wafers using THz Spectroscopy," (Under Review).

H. Altan, A. Lan, F. Huang, J. F. Federici, and H. Grebel, "Characteristics of Nanocomposites using THz spectroscopy," CThP3, CLEO 2004.

F. Huang, B. Schulkin, H. Altan, J. F. Federici, D. Gary, R. Barat, D. Zimdars, M. Chen and D. Tanner, "Terahertz Study of 1,3,5-Trinitro-s-triazine (RDX) by Time Domain Spectroscopy and FTIR," (Submitted to Appl. Phys. Lett.).

H. Altan, A. Lan, F. Huang, J. F. Federici, and H. Grebel, "Characteristics of Nanocomposites using THz spectroscopy," Proc. SPIE 5268, 53 (2004).

H. Altan, A.Lan, F.Huang, J. F. Federici, and H. Grebel, "Characteristics of Nanocomposites using THz spectroscopy," Proc. SPIE 5070, 53 (2003).

J. F. Federici, D. Gary, B. Schulkin, F. Huang, H. Altan, R. Barat, and D. Zimdars, "Terahertz imaging using an interferometric array," Appl. Phys. Lett. 83, 2477 (2003).

J. F. Federici, H. Altan, F. Huang, and H. Grebel, "Characteristics of nano-scale composites at THz and IR spectral regions," The International Symposium on Spectral Sensing Research (ISSSR) 2003, Santa Barbara, CA June 2003.

J. F. Federici, D. Gary, B. Schulkin, F. Huang, H. Altan, and R. Barat, "THz imaging using an interferometric array," The International Symposium on Spectral Sensing Research (ISSSR) 2003, Santa Barbara, CA June 2003.

K. M. Lanzetta, A. M. Wolfe, H. Altan, X. Barcons, and H. Chen, "Damped Lyα Absorption Associated with an Early Type Galaxy at Redshift z=0.16377," AJ 114, 4, 1337 (1998).

G. Leussis, J. Faber, H. Altan, Z. Colon, A. Hervias, J. Janis, J. Mallozzi, J. Thomas, C. Wilson, & F.M. Walter, "Rotation Periods of the Low Mass Pre -Main-Sequence Stars near Epsilon Orionis", ASNY-Proceedings (1997).

To My Parents, Aysen and Gunes Altan

ACKNOWLEDGMENT

I would like to thank my advisor Dr. John F. Federici for his support of my efforts here at NJIT since I began working with him in July of 2001. His ideas and discussions have been an integral part of my learning and research. I would also like to thank Dr. Haim Grebel for supporting me as well through these years. His samples provided the basis for my research. Special thanks go to Dr. Aidong Lan and other graduate students of Dr. Haim Grebel for doing their best in preparing the nanocomposite samples. And also special thanks go to Dr. Daniel Pham and his colleagues for sending us various semiconductor wafers.

I also would like to acknowledge the help of Dr. Oleg Mitrofanov who opened his lab at Lucent Technologies, Murray Hill, NJ, to me and supported my research efforts here at NJIT by providing the facilities to manufacture the photoconductive LTG-GaAs antennas so necessary for my research.

I would also like to thank the rest of my committee members, Dr. Andrei Sirenko, Dr. Zafar Iqbal, Dr. Zhen Wu and Dr. Martin Schaden for their support in my research efforts.

Throughout my education my number one support has been my family and friends. My love, Jeannette, my sister and my brother-in-law have all been with me through thick and thin so they deserve and receive my utmost respect and gratitude.

TABLE OF CONTENTS

TABLE OF CONTENTS
(Continued)

TABLE OF CONTENTS
(Continued)

TABLE OF CONTENTS
(Continued)

TABLE OF CONTENTS
(Continued)

LIST OF TABLES

LIST OF FIGURES

LIST OF FIGURES
(Continued)

Figure **Page**

LIST OF FIGURES
(Continued)

Figure **Page**

LIST OF FIGURES
(Continued)

Figure **Page**

LIST OF FIGURES
(Continued)

Figure **Page**

LIST OF FIGURES
(Continued)

Figure **Page**

LIST OF FIGURES
(Continued)

Figure **Page**

LIST OF FIGURES
(Continued)

Figure **Page**

LIST OF FIGURES
(Continued)

Figure **Page**

CHAPTER 1

INTRODUCTION

1.1 Objective

The objective of this dissertation is to determine the opto-electronic characteristics of a variety of nanocomposites as well as various device specific semiconducting materials using THz spectroscopy.

Nanocomposites like Single Walled Carbon Nanotubes on Quartz and Ion implanted Silicon Nanoclusters in fused silica were examined in the range of 0.2 to 0.7THz. Their electronic characteristics were analyzed using standard and modified free-carrier conduction models.

200mm diameter $Si_{1-x}Ge_x$ wafers with varying Ge content and 200mm diameter Oxide (SiO_2 or HfO_2) coated p-type Silicon wafers were analyzed so as to extract their electronic properties. Additional experiments on the dielectric coated wafers revealed that the effect of oxide on conduction can be quantified in the 0.2 to 1 THz range. Free-carrier based models were applied in novel ways to infer these properties.

1.2 Why Study Nanomaterials?

With the advent of numerous techniques developed to pattern and create materials on the nanometer scales, a need developed to be able to accurately predict and measure their intrinsic electrical properties. While imaging methods can tell a great deal of the structure

down to the atomic scales, the electrical properties have remained a challenge. In measuring such a property one would assume that a measuring device would need to be on the same scale as the nanoscale structure. In this regard, techniques have been developed in the last few years to pattern contacts or create probe tips on such small structures [1].

The majority of the methods that have been developed mostly yielded information concerning the interaction of the nanomaterial structure with different environments and not the structure's intrinsic properties [2]. Nanomaterials on small scales have intrigued scientists because of the fundamental challenge they impose on our well-established understandings of the electronic behavior of their bulk counterparts. For example, how are the electronic properties different in silicon nanostructures (< 10nm) as compared to the silicon wafer (bulk material size on order of microns)? In this respect, one would like to find out what happens to the electrical conductivity when the size of the device is on the order of the mean free path (the characteristic distance over which carriers scatter and lose their energy)? Our hope before we engaged in this research was to answer these questions and investigate the conduction mechanisms involved in nanomaterials, in particular single walled carbon nanotubes.

1.3 Nanocomposites

To date, nano-sized structural formations have been obtained from a variety of bulk samples that are metallic, semi-metallic or non-metallic in elemental form. Characteristics of each structure can further change due to different crystal structures that have been observed for the same material on the nanoscale, some examples include

hexagonal or tetrahedral silicon both derived from silicon, as well as the bucky ball (fullerene), single walled carbon nanotube (swcnt), or multi-wall cnt (mwcnt), all based on carbon. Among the many different types of structures, we can further classify them by the way they are grown. Some nanomaterials are grown from a parent substrate, some are grown individually from atomic constituents and some are used to tailor the properties of a host material. The latter group is usually referred to as nanocomposites or artificial dielectrics – manmade composite materials consisting of a dielectric matrix (host) containing clusters of another material (guest).

Initially, artificial dielectrics were to be used in the construction of lenses that could focus microwave radiation [3]. In this case metallic particles, in any form such as spheres or wires, with dimensions on the order of millimeters, were embedded in a dielectric substrate. The index of refraction of the resulting dielectric was modified; in essence it was defined by the electric or magnetic dipoles induced in the conducting particles. This had profound implications. The scientific community by now has realized the great potential that could be gained by exploring interactions between light and matter in the optical frequency domain where sub micron size particles are required [4,5,6,7,8,9]. As different sets of material interactions were explored researchers realized that the effect of the material on the host could be further enhanced in the presence of light. From these investigations new classes of materials were born, ones whose properties can be conditioned by the presence of light and hence were called conditional artificial dielectrics (CADs). For example, a system of semiconductor particles embedded in a glass matrix may be brought to a conductive state by absorbed photons having energy above the bandgap energies of the particulate. The material can be characterized

as semi-conducting or semi-insulating depending on the energy of the incoming photons and the application. One needs to note that the embedded particulate/clusters have to be smaller than the wavelength (λ) of the radiation, due to scattering effects which increase as λ^{-4}. Furthermore, these materials not only exhibit linear interactions. In particular, upon photo doping (shining light), strong non-linear interactions can be observed due to optically activated dipoles between semiconductor clusters. Such composites could be exploited for novel device applications.

1.4 THz on Nanocomposites

These different behaviors define the electrical properties of the resulting medium (AD). To better understand these properties, methods need to be developed that can extract information related to the composite materials electrical permittivity or its dielectric constant, given that we know the properties of the embedded conducting particles and the host dielectric material. As mentioned earlier, a non-contact technique, such as spectroscopy can be used to analyze the material properties. Since the absorption properties of the medium depend on the cluster size and conductivity [4], probing wavelengths in the THz frequency region is advantageous due to two reasons:

- The wavelengths are much larger than the cluster sizes (sub-mm to mm), so that scattering effects can be ignored.
- The conduction band of the semiconducting medium under photodoping is no longer continuous, the state separations lie in the THz frequency range.

The latter is the consequence of the photo-generated carriers. Their presence, in general, increases the refractive index of the host medium [3]; thus the dielectric properties at

other frequency regions (THz region) have changed and can be determined through Kramers-Kronig's relation. The conduction energy bands split into discrete states, which is an indication of quantum confinement. It has been shown that the states' separation is in the THz frequency region for cluster sizes on the order of tens of nanometers [10]. By probing the sample with a THz source, the underlying physical processes of carrier transport within these structures can be understood, and this can aid in the development of device design and applications.

Time-resolved studies can also reveal fundamental carrier transport properties within these clusters. Recently, there have been many investigations into the ultrafast (picosecond or shorter) carrier dynamics of nano-sized clusters [11] using THz pulsed-spectroscopy. The mobility, inter-valley scattering, carrier relaxation times, and mean-free path are important parameters for assessing the electronic and optical properties. Time resolved spectroscopy where one color (visible) of pulsed radiation excites the sample and the other color (pulsed THz) probes the sample could be used to measure these parameters.

An additional aspect that we can explore with the above technique deals with non-linear effects that have been observed for some nanocomposites [12,13,14]. Little is known about the interactions between individual clusters or nano-structures. We can explore interactions if any between varying density nano-clusters in the composite material using THz spectroscopy, and quantify the nature of any non-linear behavior.

1.5 200mm Heterostructure Wafers

The ability to measure the mobility as well as other electrical parameters using an all-optical method such as THz spectroscopy, with the added benefit of being able to probe "deep" layers, is also an appealing prospect from the viewpoint of the semiconductor industry. The need for higher speeds in electronic signal transport has driven this industry to explore novel materials based on the old-industry workhorse, silicon. These novel materials are a composite of silicon with some other material that would enhance its mobility and other electrical parameters. These composites can be analyzed the same way as the nanocomposites, by using THz spectroscopy.

The other trend in the industry is towards smaller devices, which in turn means smaller in-scale dielectric materials to shield one device from another. In this arena novel dielectric materials are being developed to replace SiO_2, which is the current standard for many devices. It is imperative that the effects of other dielectrics are known on the electrical parameters of the device medium. We can use the low-THz radiation energies to probe the effective number of free-carriers, which contribute to the materials mobility. The benefit of a non-contact technique to measure electrical quality of 200mm diameter wafers, which in turn will be used to manufacture devices, is immeasurable to the semiconductor industry.

With the use of the aforementioned techniques we applied our THz-time resolved spectroscopic method in determining the linear and non-linear (non-equilibrium) electrical transport properties in nanocomposites such as SWCNTs on quartz and ion-implanted Si nanoclusters in fused silica. We also applied THz spectroscopy to measure the mobility of semiconductors such as $Si_{1-x}Ge_x$ 200mm diameter composite wafers and

SiO_2 and HFO_2 coated 200mm diameter Si wafers. Through the use of visible pump/ THz probe spectroscopy, we tried to deduce the nonlinear electronic properties of the nanostructures. In the longer term, these investigations of nanoscale structures could lead to all optical high-speed communication switches and novel optically controlled THz/millimeter wave devices. The techniques we developed and results we obtained for numerous 200mm semiconducting wafers based on THz spectroscopy can lead to the development of industrial tools which use THz radiation to characterize electrical properties.

This work is presented in 5 chapters including an introduction and conclusion, in addition to two appendices. THz spectroscopic methods are discussed in detail in Chapter 2, with emphasis given to our experimental set-up. In Chapter 3 we present the experiments we've conducted on Single Walled Carbon Nanotubes, and Ion-Implanted nanocrystalline Si using visible-pump/THz probe techniques, as well as discussing experiments on a variety of other nanomaterials for which no response was measured. In Chapter 4 we present work developed in conjunction with a leading semiconductor manufacturer in characterizing $Si_{1-x}Ge_x$ composite and HfO_2 and SiO_2 coated wafers using the techniques we outlined in Chapter 2. Appendix A discusses in detail the steps we took in manufacturing the photoconductive transmitter/receiver pair used to generate and detect THz. Appendix B discusses preliminary measurements on hexagonal silicon and carbon nanotubes on either quartz or in polymer on quartz, all acquired recently in the summer of 2004.

CHAPTER 2

THz-TDS

2.1 Overview

In Chapter 2, the THz-TDS technique is explored. We discuss THz generation/detection methods we employ as well as instrumentation used in our experiments. A variety of THz spectroscopic techniques and conduction models are given and limitations are addressed. The Visible Pump/THz spectroscopy technique is demonstrated by applying it towards analyzing Low temperature Grown (LTG)-GaAs, whereafter results are discussed extensively.

2.2 CW and Pulsed THz Sources

The THz region of the electromagnetic spectrum has gained much attention in the recent past. The THz regime compared to the electromagnetic spectrum is very narrow only spanning from the far-infrared region to the millimeter wave region (30μm-10mm, see Figure 2.1). Even so, it is very important in optical and solid state physics because of the many interesting phenomena that fall directly in to this region. These range from lattice vibrations and free-carrier absorption in dielectrics [15], to rotational and vibrational absorption of molecules in liquid and gas phases [16,17]. Government and private sectors have primarily fueled the development of THz sources and detectors for applications that range from spectroscopy/imaging to communications and radar. The small energies

associated with THz waves allow them to pass through most non-metallic, non-polar materials (metals are perfect reflectors in the far-IR) enabling spectroscopic detection and imaging of subsurface layers. Concurrently, larger bandwidths associated with THz (10^{12} Hz) waves make them an attractive tool for space-based (primarily due to the fact that water absorption is dominant in the THz region) communication methods, where large data transfer rates are now being realized [18].

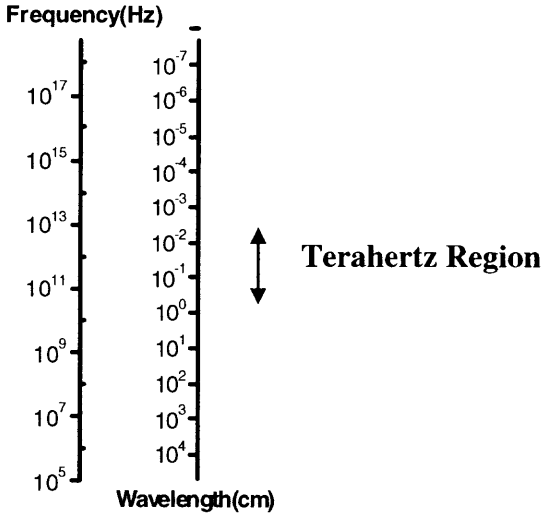

Figure 2.1. Terahertz region of the electromagnetic spectrum. It roughly spans the range from 100GHz to 30THz in frequency. 300μm=1THz=33cm^{1}=4.1meV.

These interests have driven development of THz sources that can be characterized into two categories: continuous and pulsed. Incoherent broadband THz emission can be generated with mercury arc lamps, while there are numerous designs being developed for coherent THz sources, such as CW [19] or pulsed THz lasers [20]. The difficulty with compact CW sources is that they are still relatively low power (< 100mW), however, few watts CW THz sources seems to be a reasonable expedition [20] in the near future. Other continuous sources are based on electron beams such as the ones used with Free Electron

Lasers (FEL). They are tunable and generate THz radiation for short periods of time with really high peak output power (up to 1kW).

Here at NJIT we used a pulsed-THz source in our experiments. Pulse THz generation usually require mechanisms that employ some medium (semiconducting) triggered by an ultrafast visible laser pulse. The first mechanisms used to generate THz pulses/transients were based on photoconductive switches triggered by ~100fs laser pulse from a dye laser [21]. The photogenerated carriers are accelerated in an external field, i.e. applied bias, radiating into free-space or some non-metallic medium. Other mechanisms known to generate THz transient radiation include Optical Rectification [22,23] and THz generation due to the displacement rather than the transient current [24]. In our system, the transmitter (as well as the detector) is based on a photoconducting (Low Temperature grown GaAs) antenna due to its efficiency in generating THz power compared to the aforementioned methods.

2.3 THz-TDS

After obtaining a means to generate the THz transient, THz spectroscopy systems constructed from optical components were used to perform spectroscopic/imaging analysis on various samples. One of the most common configurations, and the one, on which our set-up (Figure 2.2) is based, is the method of THz-Time Domain Spectroscopy (THz-TDS). THz time-domain spectroscopy has been prevalent for the last twenty or so years dating back to the introduction of femtosecond duration pulsed lasers. Experiments can be characterized into transmission or reflection spectroscopy and pump-probe spectroscopy. The former, transmission spectroscopy, is probably the most widespread

method used in the THz region. It has been used for studying a great variety of materials, including dielectrics [15], semiconductors [25,26,27,28], superconductors [29], organic materials [30], liquids [16], gases [31] and flames [32]. The advantage of this method compared to conventional methods like optical spectroscopy is that one is able to measure the time-dependent THz electric field. This means that both the amplitude and the phase of the Fourier components of the transmitted THz pulse are determined and thus the complex refractive index of the sample can be calculated, without the need for Kramers-Kronig based calculations.

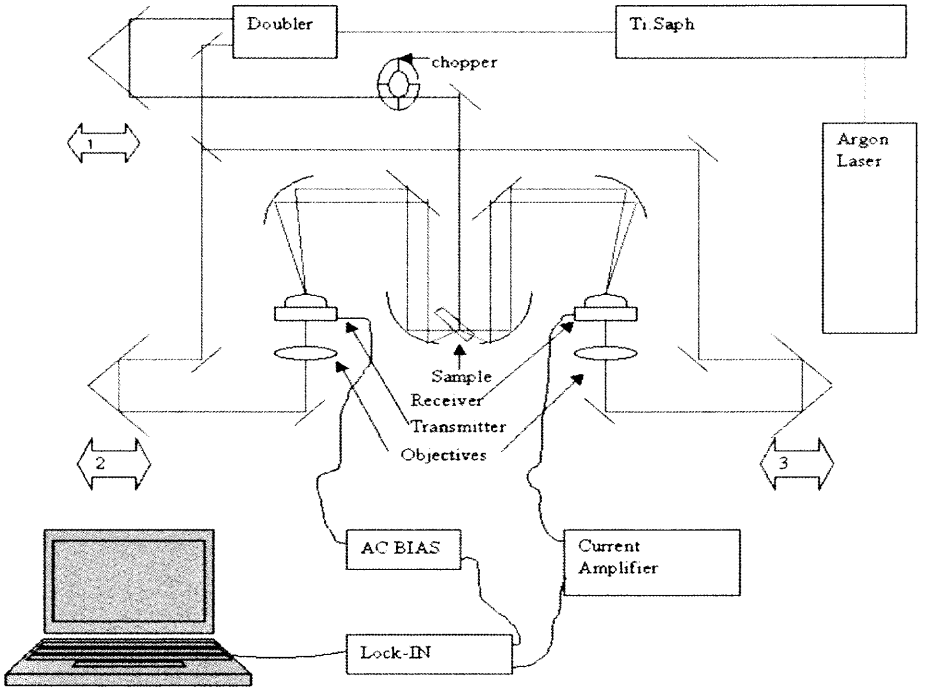

Figure 2.2. Schematic of the set-up we use to perform all the experiments outlined in this dissertation. In the above configuration the sample is placed at the focus of the THz beam (aided by off-axis parabolic reflectors) at a 45° angle allowing for Visible Pump/THz Probe measurements. The visible pump beam is obtained by frequency doubling the pulse train from the Ti:Sapphire. It is then mechanically chopped. The THz pulse train is generated and detected by the aid of two similar photoconductive antennas. The modulated signal is detected through a current amplifier and a lock-in, allowing for the waveform to be displayed on the computer monitor. There are three delay lines, and depending on the experiment, one or more are translated so as to acquire the data (See Table 2.1).

The THz-TDS set-up, which is configurable for transmission, reflection and visible pump/THz probe spectroscopy (see Table 2.1), is shown in Figure 2.2. A femtosecond Ti-Sapphire laser (*NJA-4, Clark-MXR Technologies*) at an 82MHz rep-rate drives the whole spectrometer. An ultrafast pulse (τ~80fs, measured with an Optical Spectrum Analyzer), p-polarized, from the laser is divided into two parts by a beam splitter. The first part (probe pulse) irradiates the transmitter, generating a THz electric transient. The second part (called gating or sampling pulse) gates the detector, i.e. the detector measures, what was the instantaneous THz field at the moment of the gating pulse arrival. In essence, THz time-domain spectroscopy is the process of measuring the shape of the whole THz pulse by delaying the gating pulse.

Table 2.1: Experimental Configurations for our THz-TDS Set-Up (Figure 2.2)

Type of Experiment	*Fix*	*Move*	*Reference (chop)*
Reflection/Transmission	1 (off)	2 or 3	2
Visible Pump/ THz Probe[a]	1 and 3	2 for diff. fixed pos. of 1	2 or 1
Visible Pump/ THz Probe[b]	1 and 3	2	1
THz Emission Spectroscopy	2 and 3	1	1

[a] Time-resolved pump transmission to probe recombination lifetime

[b] For peak carrier density corresponding to peak average optical excitation intensity, to generate THz waveform due to excited carriers.

2.3.1 THz Generation

The photoconducting antenna is based on a design pioneered by D. H. Auston (1984) and refined by my predecessors here at NJIT, Yi Cai (1997) and Oleg Mitrofanov (2001). We manufactured the antennas used in our experiments with Oleg Mitrofanov at Bell Labs-Lucent Technologies, Murray Hill, NJ. The antenna is basically a metal transmission line structure deposited on LTG-GaAs substrate (Figure 2.3). LTG-GaAs is obtained by growing epitaxial layers of GaAs using Molecular Beam Epitaxy (MBE) and is annealed at low temperatures (~600°C, see Appendix A for a brief description of the

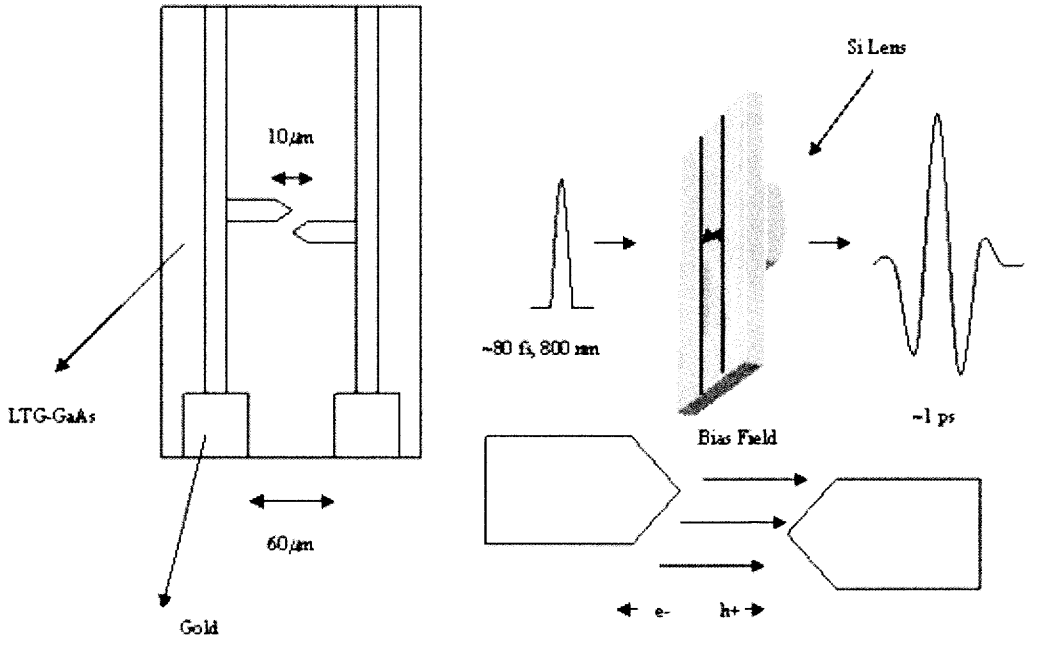

Figure 2.3. After the sub-100fs visible (λ~800 nm) pulse is focused on the gap(~10 μm) of dipole structure under a DC or AC bias, a THz pulse/transient is emitted and defocused onto a off-axis parabolic reflector with the aid of a silicon hemisperical lens on the backside of the antenna substrate. The antenna is comprised of gold transmission lines deposited on a LTG-GaAs substrate.

manufacturing process). The transmission lines each are 10 microns wide and are separated by 60-100 microns. There is a dipole structure with a gap of 5-10 microns to which the visible pulse is focused on to at a spot size of about 10 microns.

An alternating (AC) or constant (DC) bias is applied to the transmission line structure in order to accelerate created electron-hole pairs. It is important to note however that a surface depletion field can also act as the bias for the carrier acceleration [33]. In this case, the electric field is perpendicular to the surface of the transmitter contrary to the former where it is parallel. After the visible pulse with energy above the semiconductor bandgap arrives, carriers are excited in to the conduction bands. These free-carriers or electron-hole pairs are generated at a rate that is proportional to the intensity profile of the incident pulse. The generation rate corresponding to the electron-hole pairs rises rapidly also in part due to the external bias (Figure 2.4). The fast rise of the transient current results in a THz pulse (few picoseconds in duration) being radiated into free space. The photogenerated carriers then recombine, and the current in the dipole returns to its initial value. This whole process repeats with the arrival of the next optical pulse. The pattern of the radiation emitted into free space is complicated due to the thickness of the substrate as well as the silicon lens on the backside used to collimate the THz radiation. The dipole structure of the antenna predicts that the far-field on-axis radiation would follow the expression:

$$E(t) = \frac{1}{4\pi\varepsilon_o rc^2}\frac{\partial^2 p(t)}{\partial t^2} \qquad (2.1)$$

Where, $p(t)$ is the dipole moment, c the speed of light, ε_o, permittivity of free space, and r is the distance from the dipole. Assuming the length of the dipole to be a,

$$I(t) = a\frac{\partial p(t)}{\partial t} \tag{2.2}$$

then,

$$E(t) \propto \frac{\partial I(t)}{\partial t} \tag{2.3}$$

In addition, the radiated field also depends on the photoexcited static charge density. A detailed explanation of the characteristics of the radiated filed and its transient current dependency has been given before [34]. It has been pointed out [34] that the THz Electric field strength radiated away can increase if the visible pulse is focused close to the

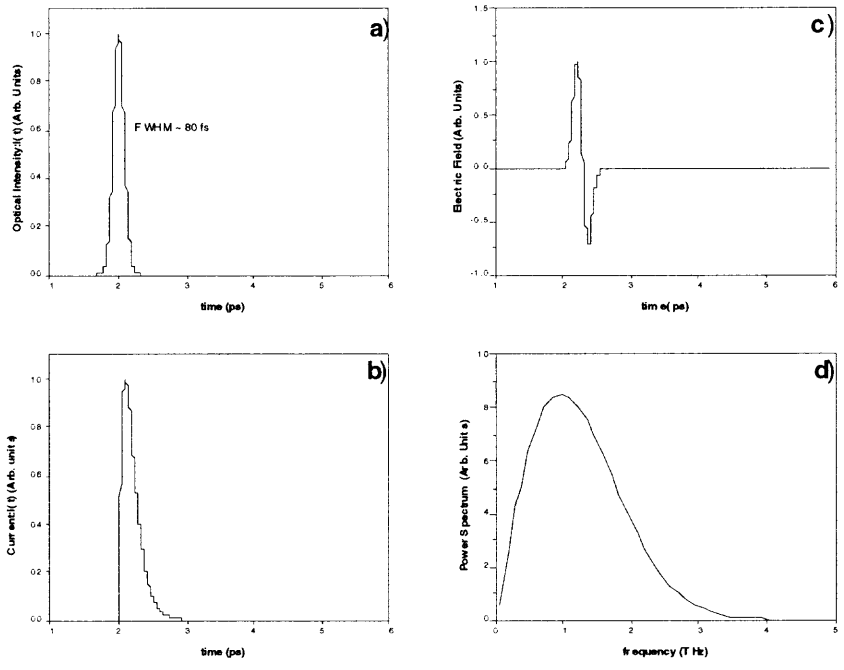

Figure 2.4. Dynamics of the emitter/photoconductive antenna under bias resulting In the generation of the THz transient. a) Optical intensity as the 80fs visible pulse leads to a fast response b) generated current which decays with recombination lifetime. The fast rise of the current leads to the generation of a THz transient as shown in c). When detected as outlined in the discussion, the time-domain waveform can be transformed using FFT methods to obtain the frequency domain spectrum.

electrode end. This type of variability in THz electric field strength due to the position

and shape of the focus of the visible pulse has prompted many to fabricate THz-fiber coupled emitters, where the position of the visible beam is always the same on the dipole [35]. In our set-up, the average generated THz power is estimated to be on the order of a few microwatts with a horizontal to vertical polarization ratio of 4:1 [35].

2.3.2 THz Detection

The eloquence of the THz-TDS method is even better realized with the fact that the transmitter structure duplicates as a receiver/detector. Here the relative arrival of the THz

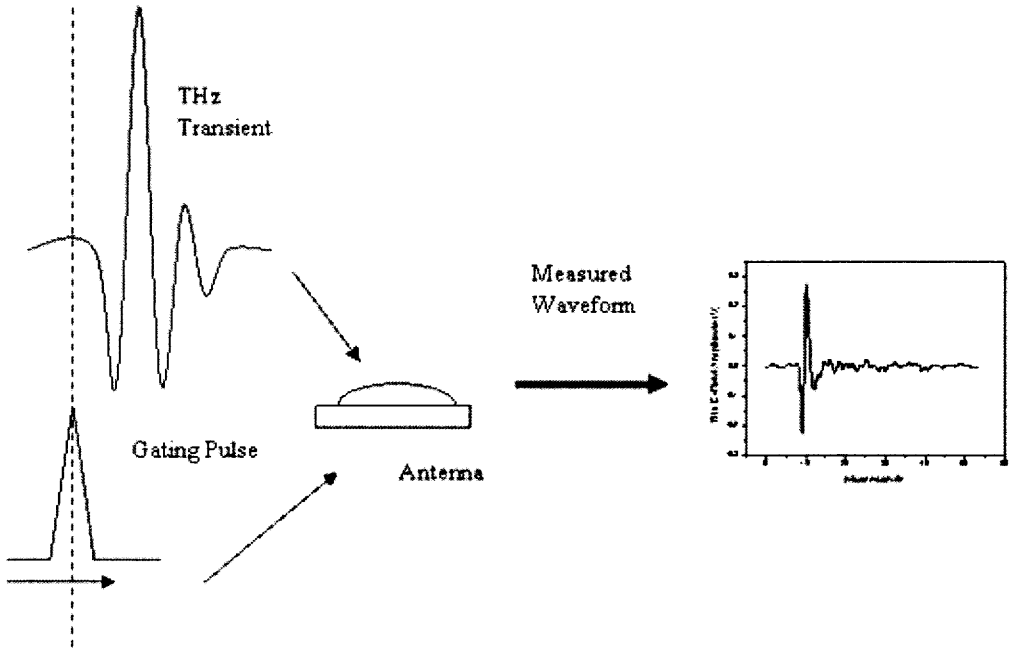

Figure 2.5. The THz transient is detected through the backside of an identical or almost identical to the emitter structure photoconductive antenna with the aid of an off-axis parabolic mirror. The beam is focused on to the hemisperical silicon lens which focuses again to the dipole antenna. The gating pulse (arriving in same phase at the dipole with the THz pulse since it is split from the same visible pulse train used to generate the THz through the emitter) probes the THz waveform amplitude. Any point on the THz waveform acts like the bias in the emitter strucuture allowing for the charge to flow across the dipole gap at a magnitude that's proportional to the amplitude of the THz transient at that point. By delaying the time separation between visible gating pulse and THz pulse we can map out the entire THz waveform in time-domain, this is the essence of THz-TDS. Note: We could have used electrooptic detection (ZnTe crystal instead of photoconducting antenna).

transient and the gating optical pulse are varied in time so that the entire THz waveform can be mapped out (Figure 2.5). This detection method allows one to measure both the amplitude and phase of the THz field unlike square-law ($Signal \propto E^2 \propto I$) detectors that measure intensity only. Nonetheless, due to the response function of the detector, the measured THz waveform is not exactly the same as the generated one, and depending on the experiment this has to be taken into consideration.

The detection method is based on a similar mechanism to the transmitter. Since the carrier recombination rate (200-300fs, [34]) is much shorter than the THz transient is (~few ps), the detector works like a sampling gate. The antenna is activated by the arrival of the optical pulse focused onto the gap, which generates electron-hole pairs and the resistance of the medium drops. The THz-transient electric field is focused onto the same gap, and acts as a bias, allowing current to flow through the dipole. The total amount of the transported charge is proportional to the instantaneous THz electric field.

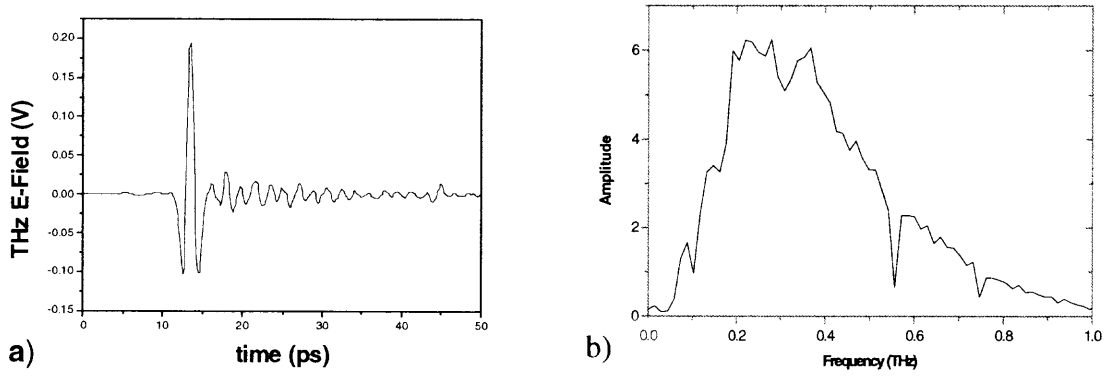

Figure 2.6. THz-TDS of Air. A) Time-Domain scan, b) FFT of a, showing main water absorption features at 0.57, 0.78 THz. Note that electric field is measured in volts through our detection scheme (lock-in), and even though spectrum is terminated at 1THz, signal amplitude has very much decreased after 0.75THz.

Since the visible pulses used to generate and detect the THz field come from the same source, they arrive at the detector with the same phase so that we can delay one pulse with respect to another to map out the entire THz waveform (Figure 2.6).

The bandwidth of the detector is determined by two factors: The photoconductive response to optical excitation and the frequency dependent response of the antenna structure. The detector response imposes the high frequency limit, due to the finite duration of the sampling intervals (carrier lifetime in LTG-GaAs).

The second factor that limits the bandwidth is the resonance properties of the dipole antenna, due to the length of the dipole. Its length determines a resonance frequency to which the spectrum peaks, thus the central frequency of the obtained spectrum can be tuned by varying the length of the dipole. This is eliminated when the sample spectrum is normalized to a reference spectrum (discussed in next section) measured with similar receiver/transmitter pair of antennas. The transmitter we used was 60μm-10μm (Distance between transmission lines-gap width), and the receiver was 60μm-5μm. Cai (1997) has discussed the use of different dipole-length receiver/ transmitter pairs in detail. With our pair, we achieve an upper limit for the bandwidth to about 1THz.

Parabolic mirrors are used to collimate and transmit the generated THz pulse through a path length of approximately .85m (Figure 2.2). In most instances, we placed an enclosure around this region and purged the air inside with dry nitrogen. This effectively reduces the absorption by water (Figure 2.6). Once the THz pulse is received at the detector, the current (few picoamps) is detected through a current amplifier (*Ithaco Model 1211*), and the waveform is plotted through a lock-in amplifier phased with respect

to modulation of the THz transient. This modulation can be achieved either by mechanically chopping the visible beam focused onto the transmitter or by applying an AC bias with a digital function generator (*HP 38120A*) on the transmitter. The THz waveform is then mapped out by varying a mechanical delay line and recorded though software routines written in LabView™ on a personal computer.

2.4 THz Spectral Analysis

Optical properties of the medium are directly obtained from the time domain measurements. The time-dependent THz electric field is given by:

$$E(t) = \frac{1}{\sqrt{2\pi}} \int_{-\infty}^{\infty} E(\omega) \cdot e^{-i\omega t} d\omega \tag{2.4}$$

thus, in the frequency domain

$$E(\omega) = \frac{1}{\sqrt{2\pi}} \int_{-\infty}^{\infty} E(t) \cdot e^{-i\omega t} dt \tag{2.5}$$

this is complex and can be expressed as,

$$E(\omega) = A(\omega) e^{i\varphi(\omega)} \tag{2.6}$$

where, $A(\omega)$ is the magnitude. The above equation states that the spectrum obtained by utilizing the THz-TDS technique has the advantage of providing phase information of the propagating pulse. Most materials are dispersive, i.e. the dielectric constant is a function of frequency ($\varepsilon(\omega)$). THz-TDS allows the imaginary and real parts of the index of refraction of the sample in question to be extracted since changes in the THz waveform describe absorption and dispersion from the media. If the complex index of the media

under examination is given by:

$$\tilde{n} = n + ik \tag{2.7}$$

Then, the THz E-field is modified after traveling a distance (d) through the dispersive medium to:

$$E(t,d) = \frac{1}{\sqrt{2\pi}} \int_{-\infty}^{\infty} E(\omega) \cdot e^{i\frac{\omega n d}{c}} e^{-\frac{\omega k d}{c}} e^{-i\omega t} d\omega \tag{2.8}$$

Absorption changes the shape of the waveform by incorporating "ringing"-long lasting electric field oscillations, which follow the main transient pulse as well as reduction in the measured amplitude. These changes can be quantified by analyzing the time-domain scans in the frequency domain and referencing them to a scan (spectral analysis requires a Fast-Fourier Transform (FFT) applied to the time domain data) where the sample is not present. Noise and spectral measurement parameters limit the sensitivity of these measurements.

2.5 Sensitivity and Measurement Uncertainty

Noise can be characterized as a background/white noise-due to the detector and instruments and a systematic noise due to the optical pulses gating the transmitter and receiver. While the LTG-GaAs antennas have very high power sensitivity per square root frequency, the carrier lifetime due to the gating pulse that defines the maximum detectable frequency of the THz transient limits the signal measurements. The stability of optical pulses generated through the Ti:Sapphire laser, i.e. amplitude, spectral variations over time, depends on a large part on the stability of the argon laser. These effects

become important when performing measurements that require long time intervals between each time step of the mechanical delay line (a delay of roughly the 1/e value-3 times the measurement time window-of the lock-in to ensure that it will precisely measure the signal as the delay line is stepped). However, most of the noise is probably due to the instruments. Specialized current amplifiers that are constructed right near the antenna structure and that can detect down to femtoampere levels can be used to increase sensitivity. After we built such a device, we found that the signal strength (lower gain) decreased and there was no change in the signal to noise, prompting us to continue use of our existing configuration. In the end, at best we were able to achieve signal to noise measurements on the order of 500:1. While this is acceptable it's far less than other reported levels of 1000:1 to 10000:1 [35] and even up to 1000000:1 [35].

The length of the waveform determines the spectral resolution of the instrument. To obtain high-resolution spectra a long time-domain scan is required. Contrary, a narrow time window allows for the detection of broad spectral peaks and can also be used to eliminate the Fabry-Perot type interference effects that can be incurred from multiple reflections as the pulse propagates through the sample. These interference effects can also be removed numerically in the post-spectral analysis of the THz pulse. While we mentioned that the upper limit of the THz-TDS technique is limited by detector bandwidth, the lower limit is given by the spectral resolution.

2.6 THz-TDS upon Reflection/Transmission

Our set-up allows us to perform measurements for several configurations: Transmission, Reflection, Emission, and Visible-Pump/THz Probe Spectroscopy (Figure 2.8). The real

advantage of a time resolved-spectroscopic method like THz-TDS compared with other frequency based methods (such as FTIR) is the ability to deduce material properties directly from the time-domain data. For example, the real index of a material can be deduced directly from the time-domain scan by examining the relative phase delay between incident and transmitted pulse (Figure 2.2) once the thickness is known. Another advantage of a time-resolved measurement technique is to examine carrier dynamics in photoexcited semiconducting samples. If the impinging light has sufficient energy to excite carriers from the valence to the conduction band, then the transmitted or reflected THz electric field will be absorbed proportionally to the carriers that have not yet recombined in the characteristic recombination time (τ_r). This technique is discussed extensively in section 2.6.2 when applied to LTG-GaAs and other materials whose response time is faster than the duration of the THz transient.

In Transmission and Reflection spectroscopy, scans are normalized (transmitted or reflected field normalized to incident field) to extract frequency dependent parameters of a medium with thickness d (which are obtained from equation 2.8):

$$n = \frac{c}{\omega d}[\varphi(\omega, d) - \varphi(\omega)] \tag{2.9}$$

And,

$$k = \frac{c}{\omega d}\ln\left(\frac{A(\omega, d)}{A(\omega)}\right) \tag{2.10}$$

One can also easily obtain the absorption coefficient of any sample if the thickness is known:

$$\alpha = \frac{2k\omega}{c} \tag{2.11}$$

Or,

$$\alpha = \frac{1}{d}\ln\left(\frac{I}{I_o}\right) \tag{2.12}$$

Where I is the intensity after passing and I_o is the initial intensity on the sample. Once any of the above parameters have been obtained experimentally, others such as conductivity, mobility, etc. can be extracted from an appropriate conduction model.

Metals, semi-metals and insulators each have different electronic characteristics. In the THz region most metals are opaque while insulating materials are purely transmitting. For example, in the far-IR, reflectance from a metal can be explained by the Drude model or free-carrier dispersion model [36]:

$$\varepsilon(\omega) = \varepsilon_\infty - \frac{{\omega_p}^2}{\omega(\omega + i/\tau)} \tag{2.13}$$

where, ε_∞ is the dielectric constant of the material at high frequencies, $1/\tau$ is the collision frequency, $\omega_p=(4\pi Ne^2/m)^{1/2}$, N, e, m are the plasma frequency, number density, charge and mass of the free carriers, respectively. While in the visible wavelengths its spectrum can be well fit with Lorentz model or local oscillator/bound charges model [36]:

$$\varepsilon(\omega) = \varepsilon_\infty - \sum_{m=1}^{M} \frac{{\Omega_m}^2}{(\omega^2 - \omega_m^2) + i\Gamma_m\omega} \tag{2.14}$$

Where, Ω_m, ω_m, Γ_m, and M are the oscillator strength, resonant frequency, resonant width, and number of resonances, respectively. From the bandstructure of various materials we can characterize metals which have overlapping bands to follow Drude, and insulators that have wide gaps between bands to follow Lorentz like conductivity models.

Semi-metals or semiconductors, can display characteristics which can be described by either Drude, Lorentz or a combination of both depending on the band structure and the region of the electromagnetic spectrum the sample is characterized in [36]:

$$\varepsilon(\omega) = \varepsilon_{\infty} - \frac{\omega_p^{\ 2}}{\omega(\omega + i/\tau)} - \sum_{m=1}^{M} \frac{\Omega_m^{\ 2}}{(\omega^2 - \omega_m^2) + i\Gamma_m \omega} \qquad (2.15)$$

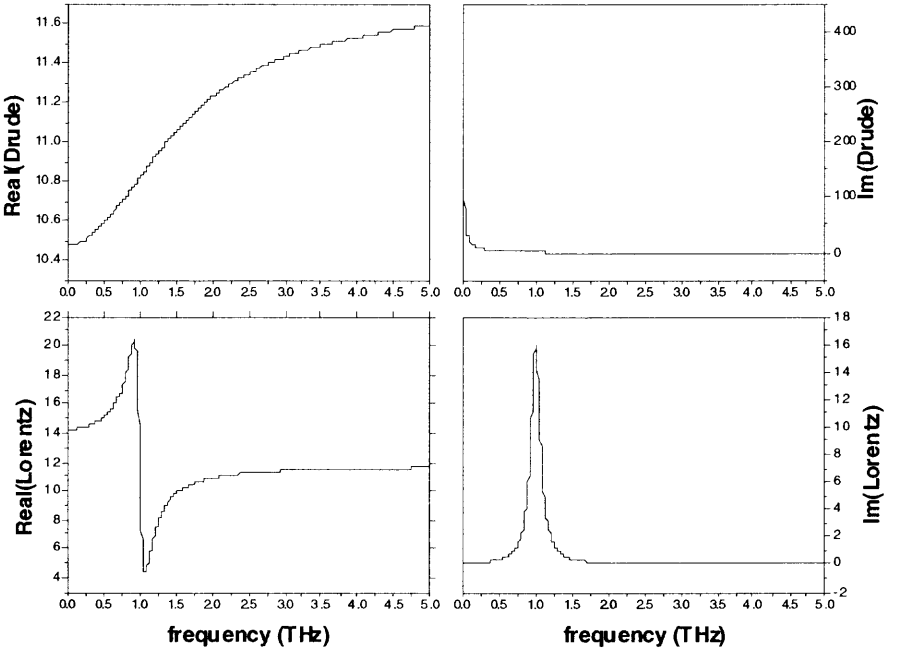

a)

Figure 2.7a. Real and imaginary parts of the dielectric function for p-type silicon with Drude model (top two curves) and Lorentz model (bottom two curves). The Drude parameters were N_p=1.46x10^{16}cm^{-3}, τ = 1x10^{-12}s corresponding to μ_p=140cm^2/V/s for $m_p^* = 0.38m_o$. Plasma frequency = 1.759THz. Lorentz parameters for m=1 are, Ω_m=10THz, Γ_m=1THz, ω_m=1THz. Lorentz absorption is introduced to show how it would affect overall response (see Figure 2.7b)

Example of what the real and imaginary components of the dielectric function would look like for the above three cases in the THz frequency range for p-type silicon is given in Figure 2.7a,b.

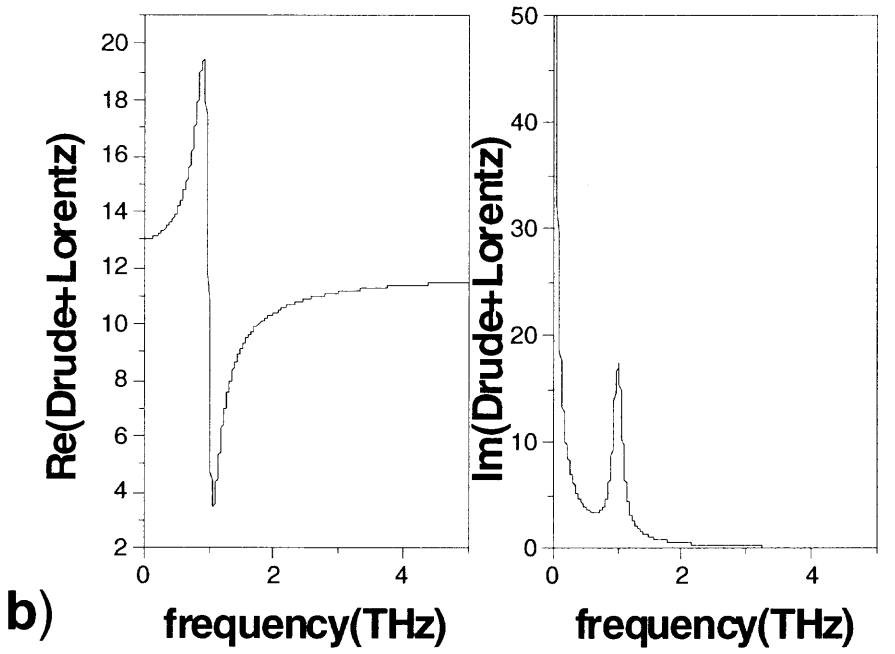

Figure 2.7b. Combined Drude + Lorentz response for the real and imaginary part of the dielectric function.

In addition to above conduction mechanisms due to interband and intraband absorption, vibrational excitations (phonons) that manifest as very narrow localized absorption features can also modify the response of a material as seen in transmission/reflection spectra. These phonons are also modeled by harmonic oscillators.

In the particular case of bulk semiconductors with low impurities or defects, due to the low energy (THz) spectral range of the THz-TDS system, the reflection and transmission measurements will follow a pure Drude model, so that only intraband transition energies of carriers in the valence or conduction bands are explored. However, in certain cases (SWCNTs-see Chapter 3), there is evidence for localized states that can be modeled with a Lorentz model. In both, interactions with phonons can be ruled out,

since the spectral range from 0.1 to 1THz is below the typical energies of acoustic and optical phonons which usually have very narrow linewidths. In addition, at room temperature (~26meV) phonon assisted transitions with energy below this set-point are not only highly unlikely but have broadened as well so as to not contribute much in the transmission/reflection spectra.

Upon examining the models discussed so far, two approaches can be taken towards analyzing the electronic parameters of any type of sample in the THz region. By extracting the real and imaginary index from the phase shift and absorption coefficient respectively, one can determine the plasma frequency and conductivity/mobility of the sample under examination (this approach assumes that the sample is thick enough so phase information can be obtained). The other approach is to extract a carrier density (corresponding plasma frequency) and scattering rate from the Drude model representation of the index of refraction, $n(\omega) = \sqrt{\varepsilon(\omega)}$, after the index of refraction is extracted from the transmission and or reflection coefficients. If the structure of the sample is known, then the reflection/transmission coefficient can be modeled with a Kramers-Kronig based analysis of the different media in the path of the THz transient. Furthermore, if the sample has both Drude and Lorentz-like properties, then the Lorentz parameters that govern the transmission/reflection spectra can be extracted similarly. The latter is the method of analysis we undertook in the applications discussed here since the thickness of the layers in samples we analyzed were too small compared to the THz wavelength so that the real and imaginary index could not be extracted directly from the measurements.

In our current Transmission configuration, the THz beam is focused to a 3mm spot size onto the sample surface with the aid of a parabolic mirror. The sample can be rotated in the p- and s-planes allowing for polarization dependent measurements.

When the sample is non-transmittive and impedes us from accurately measuring its electrical characteristics, we can proceed with reflection based measurements depending on the sample size with respect to the diameter of the THz beam.

In the reflection configuration, the sample is placed near one of the flat gold mirrors, with a THz beam spot size of roughly 40mm. Reference scans in this case are from the surface of the gold mirror, i.e. a perfect reflector in the far-IR. In both cases, the presence of water absorption lines needs to be acknowledged since they will affect the spectrum (Figure 2.6).

2.6.1 THz Emission Spectroscopy

The Emission spectroscopy method for characterizing a sample is performed with samples for which the pumping pulse can generate a THz transient. The shape of the THz waveform emitted from the sample after the irradiation by ultrashort optical pulse holds information about transient current density or polarization. If the response of the sample and the detector can be estimated then the theoretical expected THz waveform can be constructed and compared with measured values to estimate electrical parameters [37]. This technique was used for example to investigate quantum structures [38],

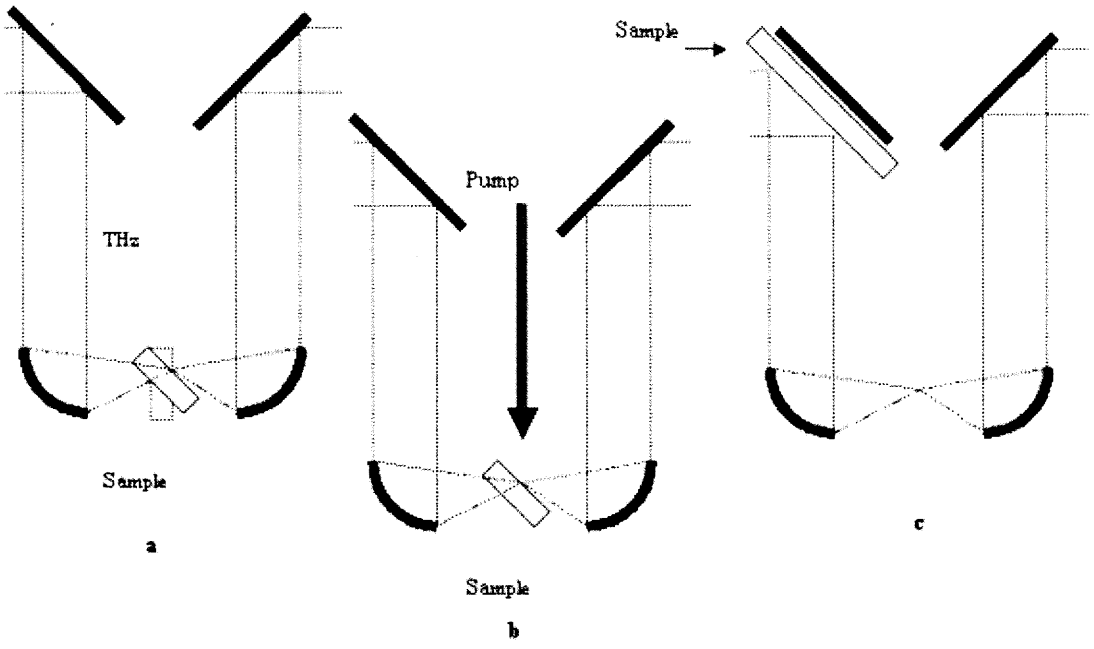

Figure 2.8. Three configurations that we can configure the set-up in Figure 2.2 to perform a) THz-TDS Transmission at normal to the interface or at an angle, b) Visible-Pump/THz Probe measurements done at 45 degree sample orientation assuring that the arrival of the pump pulse (~1cm spot size) coincide with the arrival of the THz pulse (~3mm spot size) on the backside of the sample.

semiconductor surfaces [39], cold plasma [40] and influence of magnetic field on carrier dynamics [41].

2.6.2 Visible Pump/THz Probe Spectroscopy

Finally, pump-probe spectroscopy is very suitable for investigations of ultrafast dynamics. Visible pump/ THz probe spectroscopy is similar to techniques employed in visible to near-IR regimes. Both amplitude and phase changes in the probe (THz) induced by effects from the sample due to the pump can be measured. Here, the probing pulse directly probes the response of the induced carriers or phonons. In an optical pump-THz probe experiment the changes in the response of the sample induced by the arrival of

ultrafast optical pulse are studied by probing the sample with a delayed THz pulse (Figure 2.8b). The excitation and THz beams are synchronized since they derive from the same ultrafast laser pulse. The principal interaction in most instances is the absorption of the THz pulse by free carriers. Our pump measurements can either be performed at 400nm (by frequency doubling the 800nm light though a lithium triborate (LBO) crystal), or 800nm, with pump-pulse peak energies on the order of a few nanojoules.

We conducted visible pump (λ~400nm)-THz probe experiments on [100] oriented LTG-GaAs grown on a GaAs substrate. The carrier dynamics after the arrival of the visible photoexcitation is very similar to the THz transient generation dynamics discussed earlier. Because the visible excitation is at 400nm, its penetration depth is limited to within 1 micron in the LTG-GaAs layer [42]. Either THz-Emission spectroscopy or time resolved THz-TDS technique can be done to probe the carrier lifetime. In the first case, since the visible pulse will generate a THz transient it is possible to deduce the recombination lifetime of the carriers by analyzing the generated waveform [37]-see section 2.6.1. In the latter case, the pumping pulse can be adjusted so as to arrive just before the THz pulse enabling the carrier-lifetime to be probed. When utilizing this method, specifically any THz-TDS based technique; the situation is a little more complicated since the carrier dynamics can be on scales that are faster than the duration of the probing pulse (few ps). When the THz probing pulse arrives, we expect to see the amplitude of the generated THz transient from the sample to decrease. This occurs, since free carriers which not yet have recombined absorb the THz probe. However, in the instance that the duration of the THz pulse (few ps) is comparable to the recombination lifetime (~1ps-[21,23,42]) we need to perform the experiment so as to not skew the

results. This places limitations on which delay lines we scan as shown in Figure 2.2. If the generated carriers respond in a time duration greater than the THz pulse then the lifetime can be probed with 1-line configuration scan (pump or probe) [43]. For times less than the duration of the THz pulse, the THz transient will not only be absorbed by photogenerated carriers but also will experience any changes in the index of refraction due to pumping so that any absorption will have frequency dependence. Because of this effect, visible pump/THz probe (1-line scanning implying moving delay lines 1 (pump) or 3 (receiver), see Figure 2.2, while keeping 2 (transmitter) fixed) can not be used to deduce lifetimes of materials whose response is short or comparable to the THz pulse duration. This was the case for one particular experiment conducted on LTG-GaAs. Figure 2.9b shows the change in THz transmission ΔE (since the sample itself generates a transient, so we must take the difference scan between pump on and pump off) taken by keeping delay line 2 fixed and scanning delay line 1. These results, as shown, can not be analyzed to extract recombination lifetime.

To analyze the recombination lifetime of such materials (whose response is faster than the duration of the THz pulse or recombination lifetime comparable or less than the duration of the THz pulse) one needs to employ Time Resolved THz Spectroscopy (TRTS) measurement technique. In TRTS, any changes in the THz pulse are analyzed with respect to the probe delay and the pump delay [42]. It is inherently non-linear because of these two temporal variables: the arrival of the pump pulse relative to the arrival of the THz pulse, and the propagation time of the THz pulse. The arrival of the visible pulse introduces a transient polarization in the sample, which will affect the propagation of the THz pulse. This is why TRTS is sometimes referred to as a 2-line

scan. By moving the transmitter (2) for fixed pump (1)-probe (2) time delays one can map out the change in THz transmission. Equally, both delay lines 1 and 3 can be scanned together while keeping delay line 2 fixed. Either scenario results in every portion of the measured THz transient experiencing the same delay from the visible pulse. Then the photogenerated carrier lifetime can be extracted as long as you deconvolute the effects with an exponential function representing the recombination of carriers and a Gaussian function representing the excitation pulse width.

In addition to the dynamical dependence of the pump-probe delay the other limitation is at the detector. Our detector response (~300fs) limits the time-resolved resolution of THz absorption, so that effectively places a lower limit on the types of materials we can study. The response of the detector has to be taken into consideration and deconvoluted from the overall model to extract carrier lifetimes for "fast decay" samples [42].

Since the sample itself generates a THz transient when illuminated with a visible pump pulse, a difference (ΔE) scan of the THz transmission through LTG-GaAs is shown in Figure 2.9a. By only considering the response to follow an exponential decay we extract the carrier lifetime to be $\tau = 2.43$ps. This is much larger than what we expect (< 1ps). The long decay suggests that there are other effects from the sample that need to be considered when extracting recombination lifetimes on such short scales.

Differential spectroscopy, which is a variant of Visible Pump/THz probe spectroscopy, is where the THz probe analyzes not the short lived carriers, but the carrier generation envelope at a fixed point. In these experiments the probe pulse is scanned

while the pump is fixed. This way, one can obtain the effect of the peak-carrier generation on the THz transmission. While this configuration of visible pumping

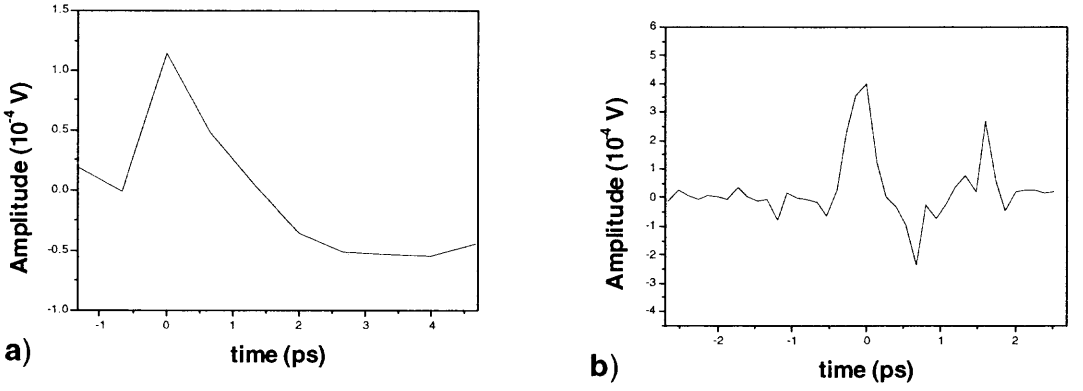

Figure 2.9. Visible pump/THz Probe measurement showing carrier lifetime decay of LTG-GaAs. Pump was centered on 400nm, with P_{av} ~30mW/cm^2. The scan in a) was done by moving delay line 2 and keeping delay line 1 fixed for different positions (2-line scan) and b) was done by moving delay line 1and keeping delay line 2 fixed (1-line scan., refer to Figure 2.2).

(essentially CW) will not allow us to investigate the time-resolved carrier dynamics, it does allow us to demonstrate a time-averaged optically induced change in the transport properties of the layer.

All the above methods have been successfully applied in measuring characteristics of a variety of samples. The THz-TDS technique has even been extended to studying biological tissues [44] as well as imaging methods [45]. THz waves have been shown to excite water molecules [46] and proteins [47]. Recently, visible pump-THz probe spectroscopy has been successfully applied to understand carrier dynamics in nanostructured materials [48]. These examples show the wide range of applications this technique can support. In the next two chapters, we applied the above methods towards understanding the carrier dynamics of novel structures like nanocomposite materials to industry standard Si based wafers.

CHAPTER 3

Nanocomposites

3.1 Overview

In this chapter we explore the optoelectronic characteristics of nanocomposites in the sub-1THz frequency range. Special attention is given to SWCNTs and 3-4nm sized Ion Implanted Silicon nanoclusters (from here on referred to as ion implanted Si nanocrystals). SWCNT structure and electronic characteristics are explored in the context of our measurements. Finally, we modeled a combination of Drude and Lorentz type conductivity to explain the observed effects.

3.2 Background

Nanoscale materials are undoubtedly one of the most exciting research areas in physics. Their development has lead to great advances in the area of nanotechnology. Coined in 1974 by Norio Taniguchi of Tokyo Science University and later defined by one time student of Richard P. Feynman, K. Eric Drexler [49], nanotechnology refers to device manufacturing on scales less than 100nm. On this spatial scale bulk material properties are not as important as surface or quantization effects. Due to their size, nanomaterial development has brought about extensive research efforts in the area of optical physics to deduce their electronic characteristics. It is the hope that through all-optical methods, methods that require no physical contacts, we can gauge materials electronic properties for use in nanotechnology applications. And in the process, effectively create a screening method to determine quality of the nanomaterial being manufactured.

Various optics experiments have been done to explore the behavior of such materials. For example, Quantum Dots sometimes referred to as semiconductor nanoparticles (NPs), have been noted for their luminescence after optical excitation [50]. Polycrystalline materials [51] that have nanomaterial scale grains as well as amorphous materials (a-Si, [52]) have been shown to exhibit enhanced electrical properties (larger mobility, faster recombination times, etc.) than their parent counterparts (for example, Bulk-Si). Attributes such as their structure (crystalline), size and proximity to each other when in clusters or stand-alone, all impact the electrical characteristics of the environment in which they are placed. This makes them attractive for use towards development of composite materials. This ability to tailor or condition the electrical properties of bulk materials (host) with addition of various nanomaterials has had profound impacts on nanotechnology. There is a multitude of different nanomaterials that we can add. Before we can implement them we have to first understand the electrical properties of the nanomaterial, then the host material, and finally the composite.

3.3 Characterization Methods

Whether the nanomaterial is in a dielectric host or, directly deposited on a substrate, optical techniques, such as Raman spectroscopy, optical absorption/reflection spectroscopy, Fourier Transform Infrared Spectroscopy (FTIR), and Fluorescence spectroscopy, have been used to deduce carrier dynamics of nanocomposites in the visible, near and mid-IR wavelength region [53]. Although these techniques provide a wealth of information there have been only a few studies in the far-infrared region of the spectrum and in particular, the THz regime [54,55,56,57] where intra-band transitions are

expected. THz time domain spectroscopy (THz-TDS) and visible pump-THz probe spectroscopy has been widely used to study ultrafast dynamics of many semiconductors [25,58]. One major advantage of THz spectroscopy is the ability to deduce electronic properties of materials without the necessity to overlay physical contacts making it a 'non-contact' technique. Therefore, by probing photo-induced carriers with THz spectroscopy one hopes to directly deduce the electronic mobility in these nanostructures.

Our motivation behind studying nanomaterials that are semiconducting stem from the fact that the conduction in bulk (electrical properties independent of small scale structure) semiconductors is well known and can be summarized in two statements: First, is that the plasma frequency is usually far above in frequency with respect to the THz region, so we expect absorption by carriers in valence band states to follow free-carrier dispersion model (Drude) (intraband transitions) due to the fact that the energy of the THz is not large enough to expect any other type of absorption (localized or acoustic or optical phonon-This is not true for SWCNTs or MWCNTs, and will be discussed later). Thus any changes in the THz transmission can be used to extract material parameters like mobility and conductivity.

The second is that if the carriers can be photoexcited with sufficient energy into the conduction band they are treated as "free" (intraband transitions) and can again be probed with the THz radiation (For SWCNTs we actually observe the presence of localized states after photoexcitation), so that material parameters like conductivity and mobility can be extracted if no appreciable change in THz transmission was observed with linear (no excitation) measurements.

Analysis for linear measurements follows the general outline as given in section 2.6, and equations 2.13-2.15. For the differential (visible pump/THz probe) case, the analysis is modified since effects of photogenerated carriers need to be incorporated into the Drude model. In the presence of photocarriers we expect the refractive index of the semiconductor to change [42]. Note that if we wanted to do time resolved visible pump/THz probe measurements (TRTS), this change in refractive index would translate into modifying the propagation of the THz pulse which needs to be considered in order to extract the correct recombination lifetime. The change in refractive index will be dictated by a change in the dielectric constant, $\varepsilon(\omega) = \varepsilon(\omega) + \Delta\varepsilon$. This incremental change is dependent on the plasma frequency ($\omega_p=(4\pi Ne^2/m)^{1/2}$) and scattering rate ($\tau$) assuming that the material response follows the Drude model. We expect the carrier density to increase after photoexcitation by an amount proportional to the photoexcited carriers, $N=N_o+\Delta N$. It is difficult to predict how the scattering rate will change. It is dependent on thermal contribution as well as the number of free carriers, and their effective mass. However, at low level of injection of carriers into the conduction levels, where thermal effects can be ignored, the scattering rate can be assumed to be similar to the linear scattering rate under thermal equilibrium [36].

Extracting the scattering rate and plasma frequency from differential measurements is far more complicated than the discussion given in Section 2.6 for linear ones. If the medium under examination is uniform and has a known thickness then the change in refractive index can be extracted by analyzing the phase and amplitude change of the THz waveform from the excited medium. However if the thickness of the medium is much smaller than the THz wavelength, impeding us from extracting phase

information using THz-TDS techniques, then we can not deduce the real change in refractive index and consequently we can not extract the Drude parameters. Again as was done with linear measurements, these parameters can be extracted only after modeling the transmission and/or reflection coefficients using a Kramers-Kronig based analysis. The drawback of this method is that we are trying to model all our measurements using only two parameters : ω_p and τ. The uncertainty in these quantities can be very large since they are coupled to each other under the Drude model [36]:

$$\frac{1}{\tau} = \frac{\nu_p^2}{2\sigma_o} \tag{3.1}$$

where, σ_o is the dc conductivity. A better way to extract one parameter would be to place a constraint on the other. For example if we can approximate the carrier injection level since we know the excitation power density on the sample surface then we can extract the change in carrier density independent of the above assertions. This is the method of analysis we took towards analyzing properties of various nanocomposites. We approximate the dielectric constant of the excited nanocomposite layer from modeling the measured differential transmission data.

Since these layers are non-uniform and are described as an artificial dielectric, we need to model the dielectric constant of the composite material that takes into account the nanomaterial density (fill factor) through out the layer as well as the dielectric constant of the host medium. Care must be taken when extracting fill factors using the method of analysis we undertook to extract Drude parameters. The fill factor will also itself be coupled to the carrier density so one has to either know this parameter beforehand or needs to decouple it from the analysis. A discussion on the model we used to

approximate the composite dielectric constant as well as the effects of the fill factor is given in Section 3.7.1.

Using THz-TDS methods, we studied many different nanocomposites. Emphasis was given for SWCNTs on quartz and Ion-implanted (3-4nm cluster size) Si nanocrystals in fused silica. The common factor between these materials is that they are both semiconducting and that the layer thickness is on the order of hundreds of nanometers, much less than the THz wavelength. We also analyzed other nanocomposites such as HipCO SWCNTs, MWCNTs (carbon nanopaper and as deposited on a quartz substrate), SWCNTs deposited in an opalline matrix on quartz, laser ablated Si on quartz, a-Si, hexagonal silicon on quartz and laser ablated Ge on quartz.

3.4 Carbon Nanotubes

Among all the latest nanoscale structures, interest in carbon nanotubes (CNTs) and the breadth of research activities across the world on their application potential have been extraordinary. It was one of the first materials to exhibit nanoscale structure after the discovery of the bucky ball (fullerene) in the 1960s [59]. CNTs were first discovered by Sumio Iijima of the NEC Corporation in 1991 [60] in the soot of an arc discharge apparatus. Their structure resembles elongated fullerenes with diameters as small as 0.3 nm (enclosed with a C36 cage) [61] and lengths of up to several microns [62,63]. The interesting combination of electronic and mechanical properties of CNTs [64,63] has led to wide-ranging investigations of their potential for future electronics. These include sensors, electrodes, as well as materials such as high strength composites, and for applications that are used for the storage of hydrogen, lithium and other metals.

3.4.1 Nanotube Types

There are two basic types of nanotubes. SWCNTs have one shell of carbon atoms in a hexagonal arrangement. Multiwalled carbon nanotubes (MWCNTs) consist of multiple concentric carbon tubes. SWCNTs are more advantageous than MWCNTs because MWNCTs have a higher occurrence of structural defects, which diminishes their useful properties such as conductivity and structural strength. However, MWCNTs are easier and less expensive to produce because most current synthesis methods for SWCNTs result in major concentrations of impurities that require removal by acid treatment. Since 1991, three major techniques were developed to mass-produce such structures: Arc discharge method (Ebbesen and Najayan, NEC, Japan, 1992 [65]), Chemical Vapor Deposition (Endo, Shinsu University, Nagono, Japan [66,67]) and Laser Ablation (Vaporization) (Smalley, Rice University, TX, 1996 [68]), see Table 3.1.

3.4.2 Structural Properties

Structural properties define the electronic characteristics that separate metallic and semi-metallic SWNTs. Both can be manipulated to form ropes or bundles of tubes whose characteristics differ from standalone tubes due to interactions between nearest neighbors [69]. Carbon nanotubes, especially SW kind, are considered as prototypes of 1D conductors. The SWCNT electronic structure is specified by a pair of integers (n, m) which represent coordinates of the wrapping vector in the hexagonal lattice of a single graphite sheet. The chirality is defined by (see Figure 3.1):

Table 3.1. Common Methods of Manufacturing Nanotubes (NTs)

Arc Discharge	CVD	Laser Ablation
Connect two graphite rods millimeters apart to a power supply, at 100 amps carbon vaporizes into hot plasma.	Place substrate in oven and heat to 600 °C while slowly adding carbon-bearing gas like Methane. As the gas decomposes it frees up carbon atoms that combine to form NTs.	Blast graphite with intense laser pulses to form a carbon based plasma, which recombines to form NTs. Can result in predominant mixture of SWCNTs rather than MWCNTs.
Can produce SW and MW tubes with few structural defects, however, the tubes tend to be short with random diameters and orientations.	Long length, tubes tend to be MW kind. This is the most productive method for industry applications.	Primarily SWCNTs with diameters that vary after baking them at different temperatures. The most costly method of the three due to requirement of lasers that produce intense laser pulses.

$$C_{n,m} = a(n^2 + m^2 + nm)^{\frac{1}{2}} \tag{3.2}$$

and the radius of the tube is given by,

$$R = \frac{a}{2\pi}(n^2 + m^2 + nm)^{\frac{1}{2}} \tag{3.3}$$

Where, a is given by the C-C bond length and is equal to 0.1424nm. Several groups have used "tight-binding" calculations [70] to predict that armchair SWCNT ($n=m$) are gapless (metallic) whereas zigzag (n, 0) or chiral SWCNT ($n \neq m$, and $m \neq 0$) have gaps that vary depending on the chiral vector. Thus, depending on the choice of the chiral vector, which defines the orientation of the unit cell to the tube axis, the nanotube either is a metal, a narrow gap semiconductor or an insulator.

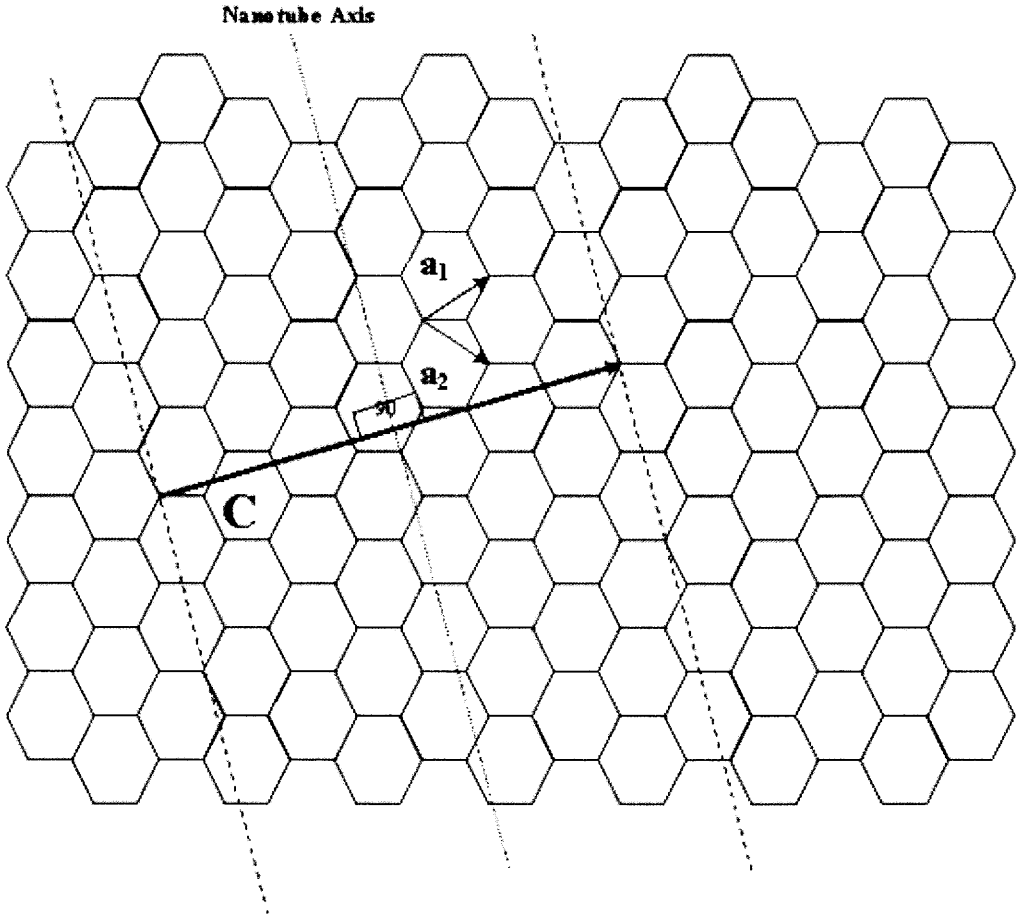

Figure 3.1. Nanotube rolled out showing hexagonal arrangement of carbon atoms. The chirality or twist is given by $C = a_1n + a_2m$, where n, m are the chirality indeces. For x = 0,1,2,3, etc, n-m = 3x represents tubes that are metallic and n-m ≠ 3x represents semimetallic tubes.

The semiconducting SWCNT has a primary gap (scales as $1/R$, where R is the tube radius) but for the case n not equal to m; with n-m divisible by 3, this gap nearly vanishes. Thus tubes whose n-m = 3×(integer) exhibit metallic properties, and for those which this is not true are semimetallic.

In addition, there remains a very small gap, on the order of 10meV = 2.4THz, that scales as $1/R^2$, induced by the tube curvature [71,72]. This secondary gap vanishes only in the $n = m$ armchair-metallic tubes.

In the case where these metallic SWCNTs are organized into bundles or ropes, it has been suggested that the intertube couplings cause a broken symmetry of the tube, inducing a pseudogap at the Fermi level [73]. Either or both of these effects could be responsible for far-infrared gap-like features; however we note that these features extend far beyond our detection limit of 1THz. The other notable difference between metallic and semimetallic tubes is inferred from optical absorption spectra. Due to different allowed optical transitions (discussed below), the energy of the lowest interband transition in metallic tubes falls between the second and third transition in the semiconducting tube of the same diameter (See Figure 3.2).

3.4.3 van Hove Singularity

A better understanding of these gaps can be achieved by analysis done on density of states (DOS) of SWCNTs [74]. A simple example of the band diagram for 1nm tubes (as was the diameter of our SWCNTs) is given in Figure 3.2. There are sharp features in the density of states that are due to van-Hove singularities. The van-Hove singularity can be examined under the DOS model. The density of states is given by:

$$dN = \frac{V}{h^3} d^3 p \tag{3.4}$$

Where, V is the volume of the sphere in momentum (p) space and h is the Plank constant. We can write the above expression in angular coordinates as,

$$dN = \frac{V}{h^3} p^2 dp d\Omega \tag{3.5}$$

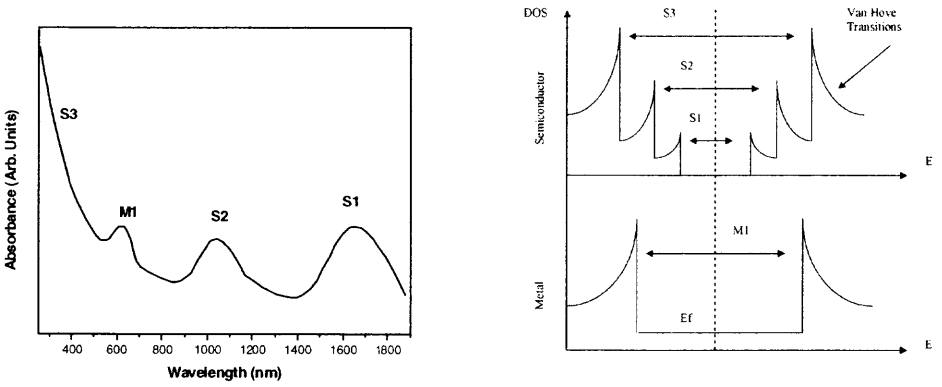

Figure 3.2. Optical properties of single walled carbon nanotubes. Semimetallic resonance are outlined S and Metallic ones are outlines as M. a) The S1, S2, S3 and M1 absorption bands correspond to electronic transitions in semiconducting and metallic SWNTs, respectively. The large absorption towards blue wavelengths is the reason behind using Visible Pump/THz probe methods to determine electrical properties. This figure was adapted from Lebedkin et al., "FTIR-luminescence mapping of dispersed single-walled carbon nanotubes," *New J. Phys.*, 5, 140, 2003. b) Density of States (DOS) showing so-called Van Hove transitions for single walled nanotubes, which lead to S and M states. Transitions between these states result from absorption of certain energies. In particular, the transition for S1 increases as the diameter of the tube decreases.

Since, $|\nabla_p \cdot E|dp = dE$ and $p^2 = 2mE$, then,

$$dN(E) = \frac{2mV}{h^3} E \frac{1}{|\nabla \cdot E|} dE d\Omega \qquad (3.6)$$

From this expression we can see that for $|\nabla_p \cdot E| = 0$ we have the van Hove Singularity.

Calculations as well as Raman spectroscopy measurements for SWCNTs show that the 1st, 2nd and 3rd tansitions (named S_1, S_2, S_3, S for semiconducting, see Figure 3.2) for ~1nm diameter tubes occur for excitation wavelengths centered around 1600-1700nm, ~900nm, and 300-400nm respectively [75]. Note that the metallic tubes also have density of states peaks with allowed optical transitions, and that the energy of this lowest interband transition in the metallic tubes falls between the second and third transition of

the semiconducting tube of the same diameter (this transition is labeled as M in Figure 3.2). The energy between each interband transition for semimetallic tubes is given by:

$$E_{ii}^{S} = 2\pi i\gamma_o \frac{a}{C_{n,m}} \tag{3.7}$$

and for metallic ones by:

$$E_{ii}^{M} = 6\pi i\gamma_o \frac{a}{C_{n,m}} \tag{3.8}$$

Where, γ_o is roughly equal to 2.7eV for 1nm tubes [76]. In addition, for tubes in ropes or bundles, interactions between the tubes have so far been characterized as Van der Walls interactions which tend to broaden the sharpness of the DOS peaks. Also, it is this interaction which is believed to give rise to the so-called pseudo gap at the Fermi level for metallic tubes:

$$E_{ii}^{S} \cong 2\pi i\gamma_o \frac{a}{C_{n,m}} + E_{vdw} \tag{3.9}$$

where E_{vdw}, which is the Van der Walls interaction energy, is on the order of 0.2eV [77]. The sharp peaks around certain wavelengths and especially towards the visible/UV range is quite interesting from the point of Visible Pump/THz probe spectroscopy. Ones hope is that if the SWCNTs can be excited by a source in this wavelength range (preferably near S_1 due to larger absorbance) then the photogenerated carriers can be well examined by a THz probing source.

3.4.4 Structural Defect Effects

Owing to their tubular geometry, SWCNT's are highly flexible and have a very large Young's modulus [78]. They sustain remarkable elastic deformations, and it has been

shown that the structure and electronic properties undergo dramatic changes by these deformations [79]. In single SWCNT (unbundled tubes) measurements, twists of the nanotube or interactions with the surface can strongly perturb the electronic structure leading to a transition from an insulator to metal. The band gaps of zigzag tubes reduce with applied strain, and eventually vanish leading to metallization. Armchair tubes remain metallic even with deformations. In particular to SWCNTs, gap-squishing effects have been observed with deformed tubes [80]. Structurally, temperature could have a huge affect on the tensile behavior (ductile or brittle) of the NT; providing the thermal energy for the defects to move and bonds to reform, leading to gap effects.

Preparation (how it's baked) of the SWCNTs is also important and can effect the electrical behavior of the tubes. For example, acid treatment is used to remove impurities from the CVD process and sometimes these leave the SWCNT in a charge-transfer doped or hole doped state. Its effect has been seen in baked (1000°C) and unbaked sample of SWCNTs. The unbaked samples showed larger absorption in the far-IR than baked ones [81]. Even though structural defects as well as interactions with other tubes cause changes in their electronic properties, none of these factors have so far been proven to alter electrical characteristics in the narrow frequency range of 0.1 to 1THz. Since the tubes we concentrated our efforts on were of the single wall variety and were semimetallic, we expect that we will be dominated by free carrier absorption if any. If the free carrier density is not large enough we might not see any absorption, since the nanocomposite films were extremely thin compared to the probing wavelength. Assuming effective mass of an electron, Tanner et al., 2002, [81] has suggested carrier densities on the order of $10^{18}cm^{-3}$ in semimetallic SWCNT mats they have experimented

on, corresponding to a plasma frequency of ~9THz, while Jeon et al., 2004, [94] has placed the plasma frequency of his SWCNT mats at around 5THz. As both these values suggest, we expect to see some absorption in our frequency range.

Other than free carriers, localized states can also contribute to the absorption. Both groups report the presence of localized absorption at 2.4THz which they explain as either due to tube curvature effects or interactions between tubes causing a pseudogap to form at the Fermi level. Even though this state is above our frequency range we expect to see its effects owing to its large resonance width (~6THz [81]). Considering both free-carriers and this localized effect, below (Figure 3.3) is a representation of what we might expect to see for a 100nm thick film, quoting measurements made by both Jeon et al and Tanner et al [81,94].

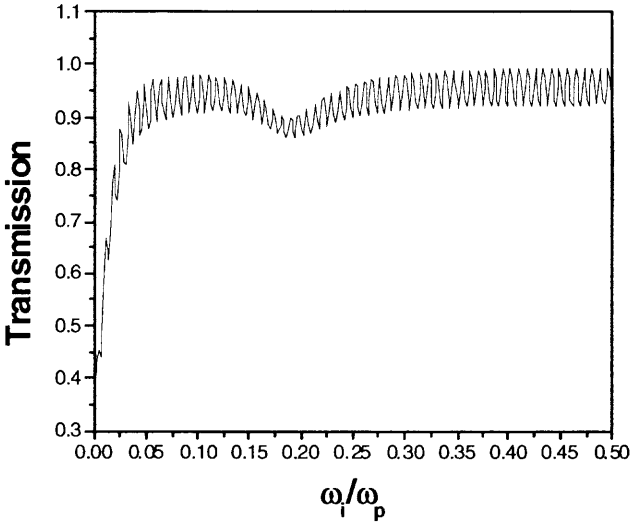

Figure 3.3. Transmission though SWCNT film on 1mm thick quartz substrate, assuming values given by Tanner et al (2002) similar to Jeon et al (2004). Plasma frequency at 8.97THz. Scattering rate~1THz, Lorentz absorption at 2.4THz, with parameters: Ω_m=60THz, Γ_m=5.5THz, ω_m=2.4THz. The fast oscillation is due to Fabry-Perot type interference effects from the substrate. Our frequency range is between ~0.02-0.08, normalized to ω_p.

Contributions of phonons as localized effects are also expected. These are due to radial breathing modes (RBM) in multi wall as well as single wall nanotubes. However, these modes usually lie above $100cm^{-1}$ and the few modes that do lie in our range of interest ($3\text{-}33cm^{-1}$) have been only shown to exist for multiwall or metallic variety of nanotubes.

All of the characteristics that we have mentioned so far have been done when the sample was under no photoexcitation. Due to the van Hove singularities in the carbon nanotubes we can probe their response to excitation which has sufficient energy to transfer carriers from states on the valence side of the gap to the conduction levels (see Figure 3.2). Few types of experiments have been conducted under photoexcitation on similar samples. Efforts have been made to characterize photoluminescense of various nanotube films [82] however no known measurements have been made in the THz frequency range after photoexcitation. We expect that after excitation into the conduction levels the carriers will follow Drude type behavior, however as is evident with our results discussed later on we observe a non-Drude type behavior after photoexcitation.

3.4.5 SWCNTs on Quartz Morphology

Films consisting of SWCNTs were synthesized using a chemical vapor deposition (CVD) technique at a relatively low temperature of 750°C. The nanotubes were formed on a quartz substrate in the presence of CO gas using Co particles as a catalyst. The catalyst did not play a role in our measurements. This growth method resulted in predominantly semiconductive nanotubes [83]. The average diameter of the tubes was assessed to be 0.9nm from HRES-TEM and SERS measurements. The tubes were distributed over a

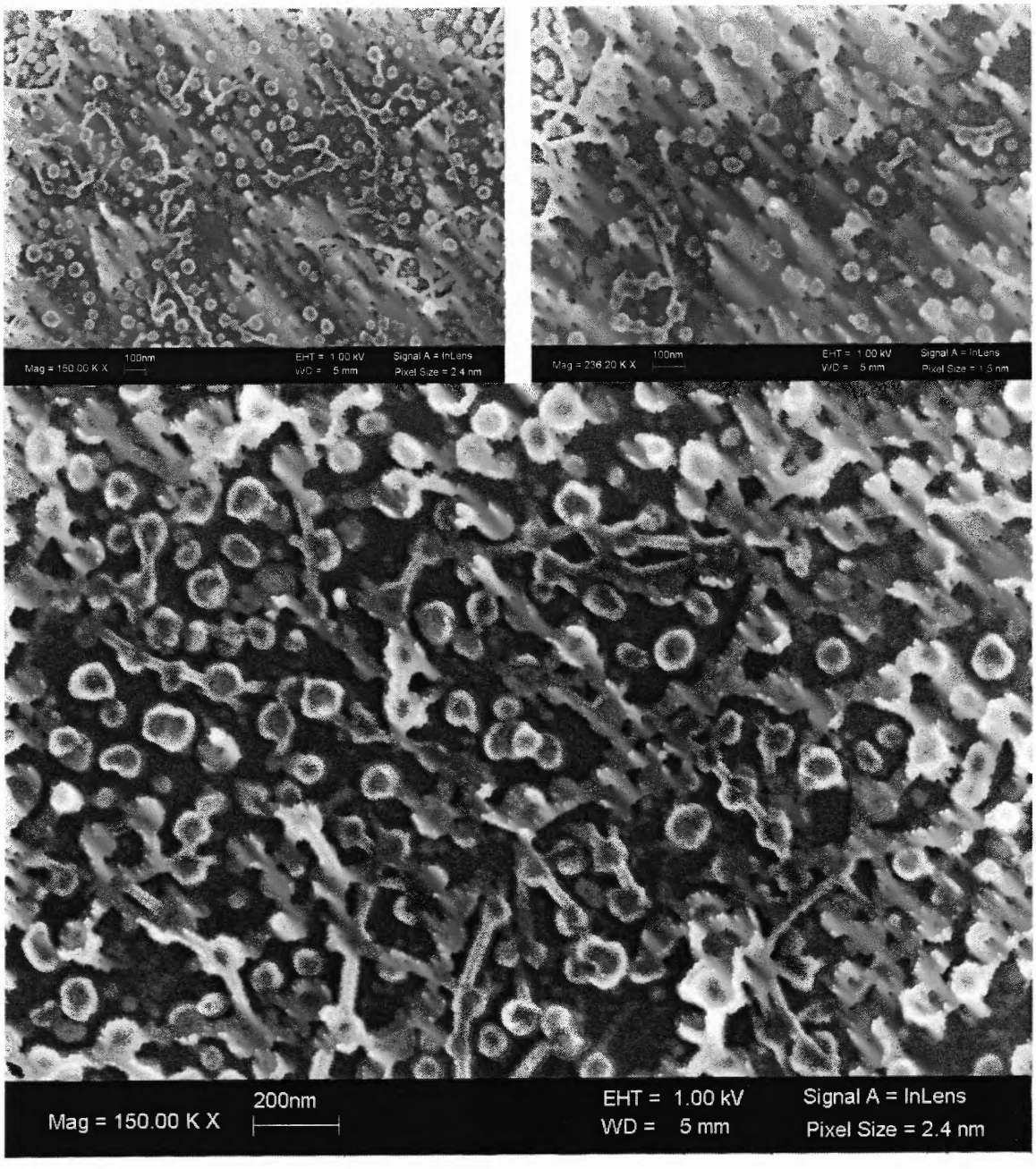

Figure 3.4. TEM images of the SWCNT film grown on quartz substrate we used in our THz-TDS experiments. All images are taken from different parts of the 2cm x 1cm sample. The tube like structures is tube bundles of 10 or more tubes. The globular matter in between is the catalyst (Co) used in the growth method.

$2cm^2$ area with a film thickness of less than 100nm (See Figure 3.4). White light experiments exhibited a large loss at wavelengths shorter than 500nm [63].

3.5 Ion-Implanted Silicon Nanocrystals and Other Samples

3.5.1 Optical Characteristics

These samples were implanted into fused silica, and have exhibited large non-linear ($\chi_3 \sim 10^{-6,-7}$ esu) values depending on the implanted cluster size (3-4nm or 5-6nm respectively) from Z-scan measurements done previously [12]. If the implantation dose, depth of implantation as well as implantation energy is known you can deduce the Si atom concentration, and from there try to deduce the number of free carriers that will contribute to the conductivity. Through photoluminescense measurements it has been found that as the cluster size decreases, the band gap of the silicon increases [84]. There is nothing to suggest that carrier density should be high enough that we are below the plasma frequency. Thus, we can assume the carrier density in these samples to be very low, on the order of intrinsic bulk silicon, $\sim 10^{10} cm^{-3}$. The transmission in our frequency range of interest (0.1-1THz) will be flat, dominated by dielectric constant at infinite frequency, which also has to take into account the dielectric of the composite layer accounting for the density of the implanted Si atoms and the fused silica (host). While linear measurements do not seem to be as useful in probing these samples, visible pump/THz probe measurements would be appropriate since the crystalline Si nanoclusters are found to be increasingly more absorptive towards the blue part of the visible spectrum [90].

Various types of small scale silicon structures exist of which only few have been studied in the THz region. Measurements have been conducted on both microcrystalline and nanocrystalline silicon with visible pump/THz probe spectroscopy. In microcrystalline silicon, a two-step carrier lifetime has been observed, where initially

majority of excited carriers recombine due to ultrafast trapping in less than 1ps, and afterwards the others recombine slowly to the ground state [57]. Similar measurements on nanocrystalline silicon show even faster recombination times of few hundred femtoseconds [85]. No visible pump/THz probe measurements of yet have been conducted on lifetime of ion-implanted Si nanoclusters. Through photoluminescence, femtosecond transient absorption measurements on samples similar to our own show a sub-10ps carrier lifetime [86]. Previously (Cai 1997), performed CW pump (Ar+-Ion at 514nm, 0.53W)-THz probe measurements (For experiment description see previous chapter), which showed large absorption in the THz transmission. The normalized transmission (THz transmission absorbed by photogenerated carriers / THz transmission under no excitation) was on the order of 10^{-4}. We too saw an effect of this magnitude from our experiments (shown later), and could only explain the observed response with non-Drude type behavior (not due to free carriers only) as is discussed below.

So far no known localized effects have been reported in the frequency range of our interest for ion-implanted Si nanocrystals, however, in micro crystalline silicon, frequency-resolved measurements of the far-infrared response of the photoexcited carrier distribution show a strongly non-Drude behavior reflecting the influence of the disorder on the conduction [85].

3.5.2 Ion Implanted Si Nanocrystal Morphology

Silicon nanocrystals were formed by Si (400keV) implantation into fused silica glass at a dose of $1x10^{17}cm^{-2}$. The film thickness was 300nm and was composed of 3-4nm Si nanocrystals on average as estimated by Transmission Electron Microscope (TEM) measurements. The overall thickness of the fused silica substrate was 200 microns.

Previous white light and photoluminescence measurements [87] exhibited an absorption band around λ=400nm suggesting that the carrier dynamics can be well examined with a visible pump-THz probe technique.

3.5.3 Other Nanocomposites

Other nanocomposites we conducted experiments on were manufactured using different techniques. Laser ablated Si on quartz and laser ablated Ge on quartz was obtained with laser assisted deposition techniques (involving a high-power excimer laser and a vacuum system). The carbon nanopaper was obtained commercially and the MWCNT was manufactured from adding a MWCNT powder to a mixture (1-2Dichlora Benzene) and baking it onto a quartz substrate forming a thin sheet of MWCNTs on the surface. Since the MWCNTs are known to exhibit metal-like characteristics, the skin depth of the THz waveform has to be larger than the thickness of the nanomaterial film in order to conduct

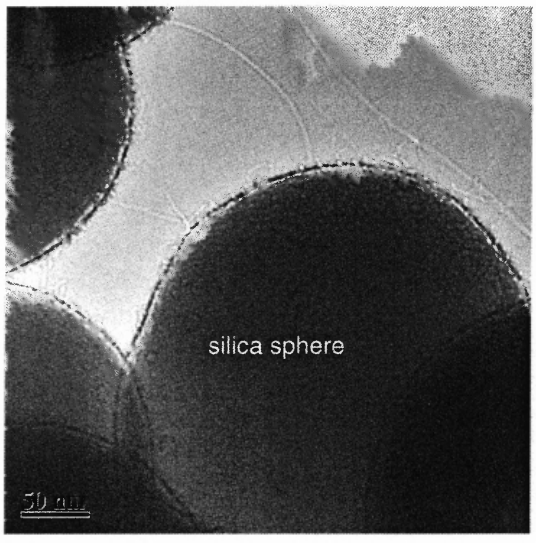

Figure 3.5. SWCNT inside a matrix made of a partially ordered array of 275nm silica spheres. The nanotubes are the small 'wirelike' structures, which extend from one silica sphere to the other.

transmission measurements. This was true in the case of the sample deposited on quartz (few hundred nanometers thick), but was not true in the case of the carbon nanopaper (microns thick).

We also performed extensive experiments on SWCNTs in an opalline matrix on top of a quartz substrate. Contrary to previous samples of SWCNTs deposited on quartz these samples contain a higher relative concentration of SWCNTs to MWCNTs (determined by High-Resolution Transmission Electron Microscopy (HRES-TEM) and Surface Enhanced Raman Scattering (SERS) measurements) [88]. The medium here can also be described as a Conditional Artificial Dielectric (CAD)-artificial dielectric that is sensitive to light-where the nanomaterial is dispersed in a host dielectric medium (Figure 3.5). The host dielectric medium is the silica spheres (opals) on a substrate of quartz. The opals offer the same advantage as the quartz in that it is fairly transparent to the THz. The silica spheres have an average diameter of 200nm as determined by SEM measurements. Visible Pump/Visible Probe measurements on this particular sample showed fast carrier relaxation times on the order of ~300fs [88]. From SEM images (Figure 3.5), visibly these samples have a far less concentration of tubes than the SWCNTs grown directly on a quartz substrate (see Figure 3.4). It is desirable to have the silica spheres highly ordered, however, since they serve as catalyst (Cobalt) supports and are grown during the formation of SWCNTs with the CO gas (found to be most efficient method of producing predominant concentrations of single wall tubes when the SWCNTs are grown together with opals) their structure experiences some disorder and the result is a partially ordered array. The SWCNTs in this particular structure are not predominantly standalone, but can exist in smaller bundles than the SWCNT sample as grown on quartz. The advantage of

this growth method is that the relative concentration of semimetallic SWCNTs to metallic SWCNTs is far greater than when they are as grown on quartz substrates without an opal matrix (determined by High-Resolution Transmission Electron Microscopy (HRES-TEM) and Surface Enhanced Raman Scattering (SERS) measurements).

3.6 Experiment and Results

The samples were placed into our THz-TDS system, which can be easily configured for visible pump-THz probe spectroscopy as was described previously (see Section 2.6). The pulsed THz radiation from the transmitter was collimated and focused down to a spot-size of 3mm onto the backside of the sample surface using a series of parabolic mirrors. The sample was placed at 45^{o} relative to both the pump and probe beams. The visible excitation at λ=400nm and pulse duration of ~80fs was generated through a second harmonic generator using a 1mm thick crystal of lithium triborate (LBO). The visible pulses were incident on the front side of the sample with a beam diameter of ~10mm. The THz probing pulses were transmitted through the sample and then collimated and focused down onto the receiver. In the visible pump/THz probe configuration a DC bias was used and the probing pulse was delayed with respect to the pump pulse.

As mentioned earlier, the lifetime of the carriers induced in the SWCNT samples are very short (less than 1ps). In standalone CNTs carrier lifetimes can be as long as 15ps [82]. Since the SWCNTS in Figure 3.4 is predominantly in bundles we expect a fast carrier relaxation time. Because this lifetime is less compared to the duration of the THz transient we can not use THz-TDS methods to resolve the recombination time (see Section 2.6.2). We employ a 2D scan method as discussed earlier not to resolve this

recombination time but to probe the response of the sample for a fixed pump-probe delay. The visible pump is mechanically chopped at 2.5kHz, and when the visible pulse is aligned to arrive and generate carriers at the sample we can scan and measure different portions of the THz pulse with respect to this carrier density. In essence we are performing CW pump/THz probe scans where we measure the response of the waveform piecewise in the time-domain to a fixed carrier density and then combine these pieces to deduce the frequency dependent response of the sample at this photogenerated carrier density. Using this differential technique, the measured THz signal was a direct measure of the change in THz transmission through the illuminated (at the peak of illumination) and unilluminated sample.

3.6.1 Unpumped Transmission through SWCNTs

The THz transmission spectra through un-illuminated SWCNTs exhibited an essentially flat spectrum (Figure 3.6) with no significant absorptive features. The sample was placed at 45° with respect to the incoming THz radiation and the transmission was fit with a curve assuming Drude-like conductivity where the dielectric constant of the nanocomposite was approximated with Maxwell-Garnett (MG) or Garnett theory. MG theory describes the effective dielectric layer of the nanocomposite as a function of the dielectric of the nanomaterial, the host medium and the volume density (fill factor) of the nanomaterial.

As mentioned earlier the fill factor (nanomaterial density in host medium) is coupled to the Drude parameters. We actually deduce this fill factor from our differential measurements where the differential absorption is described as predominantly due to

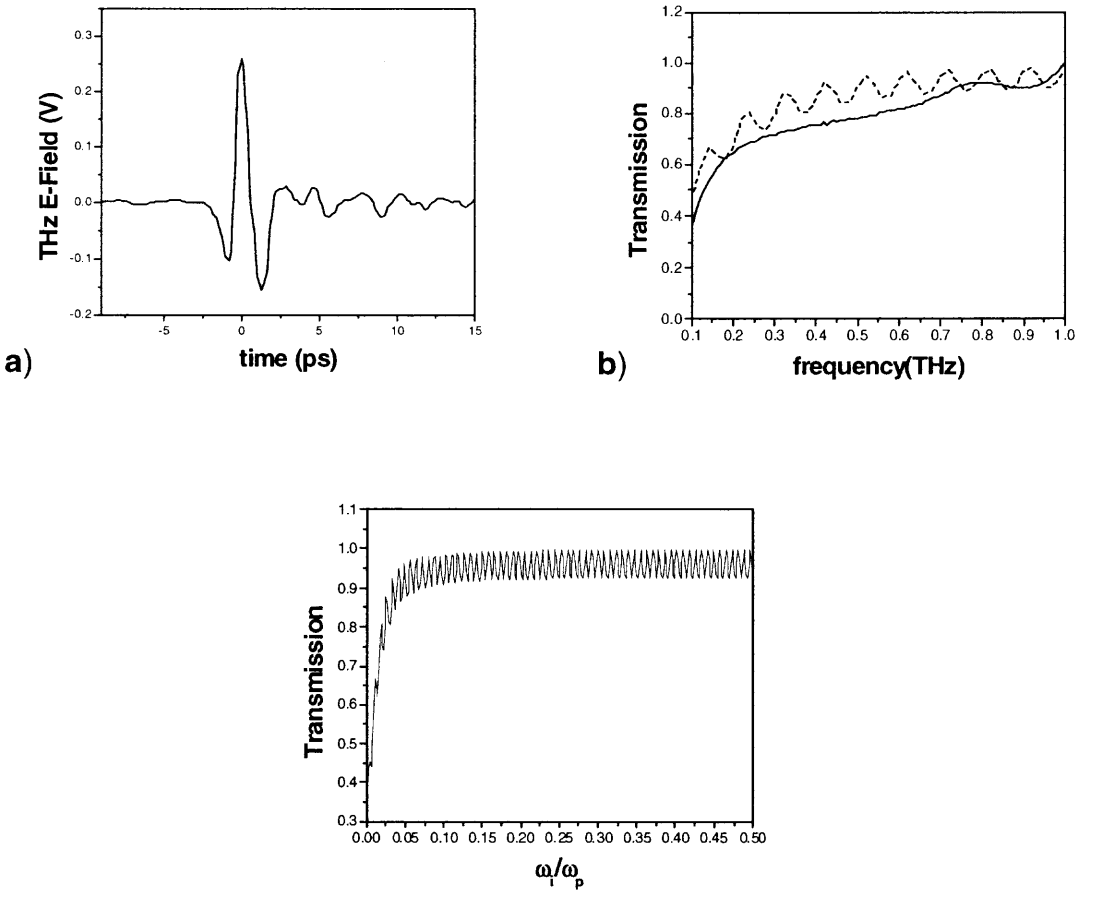

Figure 3.6. Time Domain a) THz pulse after passing through the ~100nm thick SWCNT film grown on the Quartz substrate and its corresponding b) Transmission (Normalized to scan though just the Quartz substrate). c) Response of the medium out to ~5THz, ω_p = 8.97THz, notice no Lorentz-like absorption assumed (see Figure 3.3) since our spectral range is far below its absorptive effects. The dashed curve in b) is the fit to the transmission assuming a simple Drude model for the conductivity with $N_e = 1x10^{18}cm^{-3}$ and $\tau=1x10^{-12}s$. The dielectric constant is calculated under Maxwell Garnett theory assuming that the dielectric medium is air and that nanotubes have a dielectric constant at infinite frequency of about 2 [94] (with a fill factor of roughly 5%, giving an effective index of refraction of 1.1 for thin film medium. Oscillations in b) and c) are from Fabry-Perot type interference effects.

Lorentz-like absorption (see section 3.9.2). This means that the fill factor is not only coupled to the Drude parameters but to the Lorentz parameters as well. This requires us to place an external constraint on the fill factor so we can extract appropriate conduction

parameters from the model. The 5% fill factor which was extracted form the visible pump/THz probe data was used to model the linear transmission data as shown in Figure 3.6. After analyzing the surface density of tubes in Figure 3.4, the 5% fill-factor is not unreasonable given that the nanotube density is sparse as seen in the SEM images. However, we can not say with certainty that a fill factor of 5% is an accurate depiction for these samples. MG theory and its effects on the conduction parameters are discussed in detail in sections 3.10.1 and 3.10.2.

3.6.2 Transmission through SWCNTs and Ion Implanted Si nanocrystals under Visible Excitation

Upon visible illumination and the photo-generation of charge carriers, changes in the spectral response of the SWCNT samples were observed. Figure 3.6a, c shows the response of the transient THz electric field through a SWCNT sample under visible pumping at $\lambda = 400$nm with a power level of 30mW. Visibly, the sample is transparent to the eye and under a light-microscope, surface variations reveal the presences of the nanotubes as well as voids where there seems to be none present. These voids and distributions of nanotube networks scale from hundreds of microns to few millimeters in size. The effect of this surface inhomogeneity was studied by conducting the experiment at various sample locations. Two such extreme cases are shown in Figure 3.7a, c, which represent two different positions on the same sample.

Multiple visible pump/ THz probe scans of the SWCNTs were obtained and then averaged to improve the signal-to-noise ratio. This averaging was required due to the relatively thin layer of the sample. The change in THz transmission is expected to be

small due to the relatively low pump power levels (less than <1/100), compared to previous visible pump-visible probe measurements on similar samples [88].

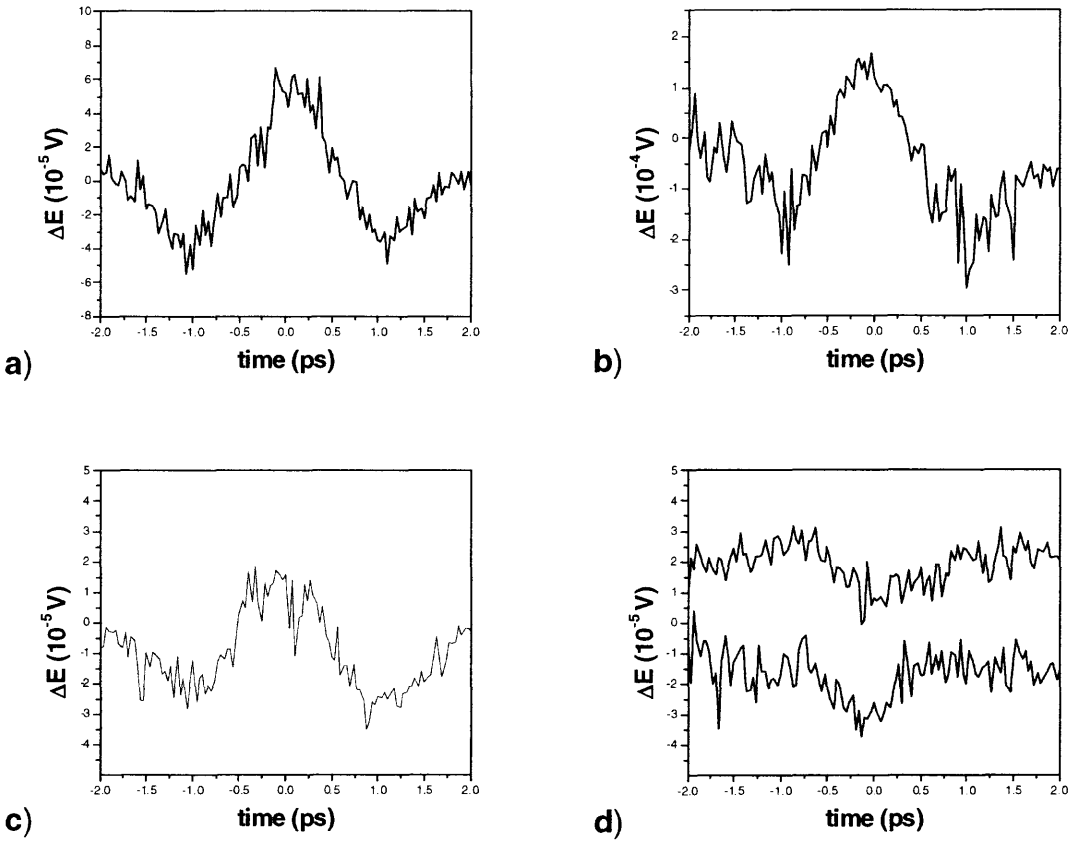

Figure 3.7.1. Visible Pump/THz probe scans through nanomaterials. These scans were done close to the peak of the generated carriers and do not give indication to any carrier dynamics. A) SWCNT on quartz (~100nm film grown on 1mm thick quartz). b) Contaminated Quartz substrate (c) SWCNT on quartz (a different region on the 2 cm x 1cm sample probed than that shown in a). d) Measurements on other grown SWCNT samples on quartz substrates (signal is not as well defined, due to noise and reduced THz sensitivity as discussed in text). Also, all these measurements were not sensitive to the phase, thus we could not extract this information from these scans. All figures are at 33.3fs resolution, and represent an average of 5 scans with 5s lock-in time constant at each step. P_{av} = 30mW/cm^2, resulting in 0.4nj per pulse.

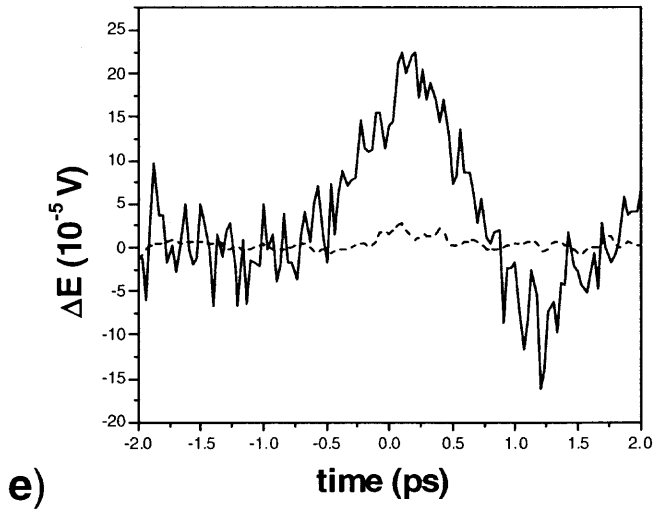

Figure 3.7.2. Refer to Figure 3.7.1 for detailed explanation, e) Ion implanted 3-4nm sized Si nanocrystals, with a 300nm implantation depth in a 200μm thick quartz substrate (solid line for pump power P_{av} = 30 mW/cm^2 and dashed curve for P_{av} = 20mW/cm^2).

These measurements are a first for such thin layers compared to the probing wavelength and relative pump pulse energy (~0.4nj, Avg. Power ~ 30 mW/cm^2). Since the relatively low pump energies require extensive averaging, researchers who work with thin film nanomaterials using visible pump/THz probe techniques rely on higher pump pulse energies (on the order of micro-joules to milli-joules). The other detriment of working with materials that require averaging many scans is that mode-locked lasers (like our home-built Ti:Sapphire laser) lose their stability over time. That is, primitive modes start to oscillate in the laser cavity, and the primitive feedback mechanisms to correct for such errors (oscillating mirrors, intracavity apertures) are not sufficient to keep the laser mode stable for such long periods of scan times. These effects limit the usefulness of these experiments at such low visible pump energies. We believe these effects to have

aided in our inability to observe such well defined time-domain waveforms as in Figure 3.7a, c (see Figure 3.7d for comparison).

Comparatively, one advantage in performing visible pump/THz probe measurements at low excitation energies maybe in the fact that the methods needed to obtain high-energy density pulses result in lower repetition rates (a consequence of pulse compression/stretching). This translates into fewer pulses averaged through measurement interval of the lock-in; however, the signal will be proportionally larger so that the measurements at high pump power would still be an improvement, ignoring any non-linear effects. Until higher pump-pulse energy measurements are made on similar samples we can not truly compare the two methods.

3.6.3 Contaminated Quartz Sample

Pump/probe experiments were performed on the substrate with and without the catalyst in order to eliminate the catalytist effects. It was found that the catalyst particles had no absorption features in the THz frequency range under differential transmission (i.e. time-domain data under a visible pump revealed no features-essentially flat. Refer to Appendix B for non-responsive differential spectra obtained from various nanocomposites).

Different samples of substrate were tested to see if it exhibited any effects. For all of the substrates tested, only one particular quartz substrate sample without the catalyst showed a response to the THz E-field (Figure 3.7b). This sample was 1mm thick. As can be observed from Figure 3.7b, the response of the quartz only substrate is comparable in magnitude to the response of SWCNTs on the same quartz substrate. Yet, the differential (pump light on/pump light off) transmission (Figure 3.8a, b) shows a clear distinction between the two samples. As discussed in the next section, we believe the differential

THz signal from this particular quartz substrate can be attributed to nano-Si particles in the quartz which are remnants of the manufacturing process [89].

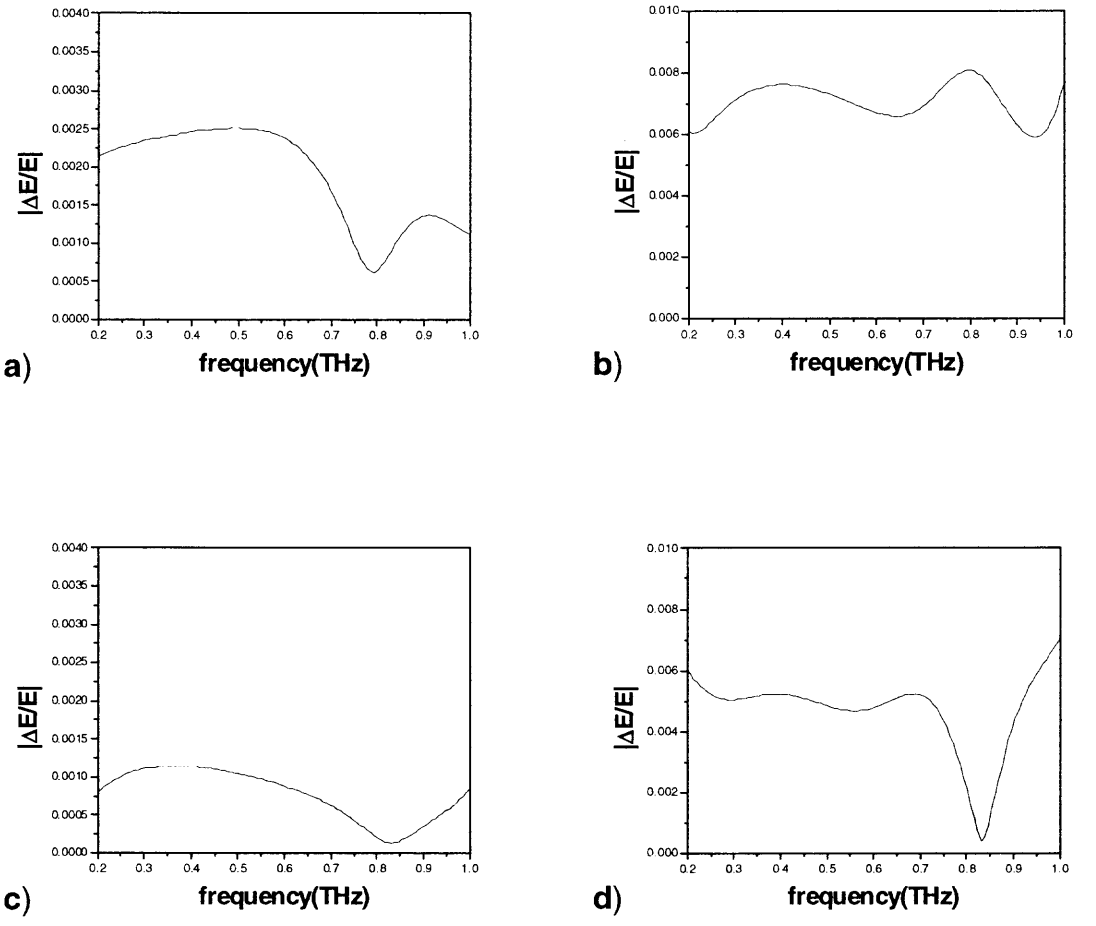

Figure 3.8. Differential transmission (FFT of time domain scan/ FFT of scan through unpumped material) for a) SWCNTs, high density, b) Contaminated Quartz, c) SWCNTs, low density and d) Ion-implanted Si nanocrystals. The dip near 0.8THz is an artifact; see section 3.10 for a discussion.

3.6.4 Ion Implanted Si Nanocrystals under Visible Excitation

Differential pump/probe experiments with pump power of 30mW at λ = 400nm on ion-implanted silicon imbedded in quartz exhibited similar behavior as the SWCNTs (Figure 3.7e). Similar to SWCNTs [88], these samples exhibited fast carrier relaxation time on

the order of a few picoseconds [90]. We note that the magnitude of the frequency domain differential transmission of the THz E-field is very similar to the corresponding curve for quartz only substrates, reaffirming our initial estimates that the particular quartz substrate used in that experiment had nano-Si particles. A possible result due to remnants of the manufacturing process, whereby the quartz is annealed to reduce effects from thermal expansion when used as substrates for host materials or optical windows for various laser based applications. The annealing can result in formation of Si clusters which we extrapolate to be the cause of this observed response; however we can not rule out surface contaminants entirely although great care was made to clean the all quartz or fused silica sides of samples with methanol.

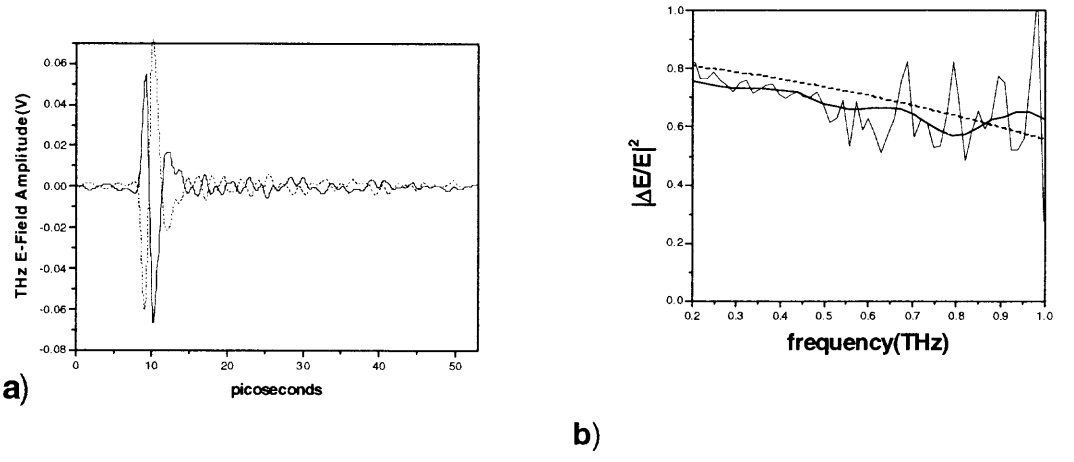

Figure 3.9. CW all lines visible Ar+-Ion Pump at 200 mW/cm^2-THZ Probe measurement on 700 μm thick Silicon wafer, a) Time-domain scan, solid line scan under pump, dashed line scan under no photoexcitation, note the appearance of the π phase reversal; b) Differential Transmission, solid line-measured data (the line with less noise shows the differential transmission for the truncated time-domain scan from 7 to 13ps), dashed line corresponds to the Drude fit with parameters $N_e = 1x10^{16}cm^{-3}$, and $\tau = 0.14x10^{-12}s$.

To probe the effects of nanosize dimensional constraints on the electrical properties exhibited by silicon, bulk Si (p-type silicon wafer with a thickness of 700μm) was used as a reference material (Figure 3.9a, b). In Figure 3.8b, the apparent π phase reversal is not due to changes in refractive index but primarily due to the fact that we are plotting ΔE = E(pump on)-E(pump off), and that since E (pump off) > E (pump on), we see the waveform "flip."

Since large non-linear effects were previously observed from Z-scan measurements on this particular 3-4nm ion implanted Si nanocrystal sample [12] we decided to lower the pump power level at λ=400nm to a level of 20mW/cm^2. Ion implanted Si films exhibited a weak but a visible absorption (Figure 3.7e, dashed line); however the pump power was not high enough to produce a similar time-domain trace. The much less signal strength for a fractional change of pump power could be indicative of non-linear processes. These measurements could not be further explored due to limited access to this sample, thus we could not rule out the possibility of an erroneous measurement.

When the experiment was repeated for SWCNTs, they showed little or no response at lower pump powers as well. However, like the ion implanted Si nanoclusters, the signal was not strong enough to analyze in the frequency domain. Whether this is indicative of non-linearity is unclear due to the relatively (with respect to ion-implanted Si nanocrystals) non-uniform distribution of nanotube networks on the sample surface.

3.7 Noise Issues and Spectral Padding Effects

3.7.1 Padding

The presence of noise in the time-domain signals of Figure 3.7a, c, e must be considered while computing the Fourier transform of the time-domain data to extract the frequency domain data (see Figure 3.8).

Prior to computing the Fourier transforms, one needs to ensure that no discontinuity was introduced in the time-domain data. Subtle changes in the padding of the data, prior to the Fourier transform algorithm, for example, can lead to large spectral features in the frequency domain (see Figure 3.10). Previously these features were thought to be "real", but later it was realized that a few microvolt difference between the noise-level of the data sets and the zero-level of the padding could lead to the erroneous features as shown Figure 3.10a. After the offset of the padding was varied relative to the offset of the raw data insuring that no erroneous spectral features were introduced, the noise level was shifted down to the zero-level and the data was subsequently padded to 2^n points (in our case, 4096). No padding and padding to 128 total data points were compared to padding to 4096 data points, insuring that there were no new erroneous spectral features. Since the window of data collection is limited in time, the zeros that are added to the beginning and end of the data set insures that the Fourier transform appears smoother and more pronounced.

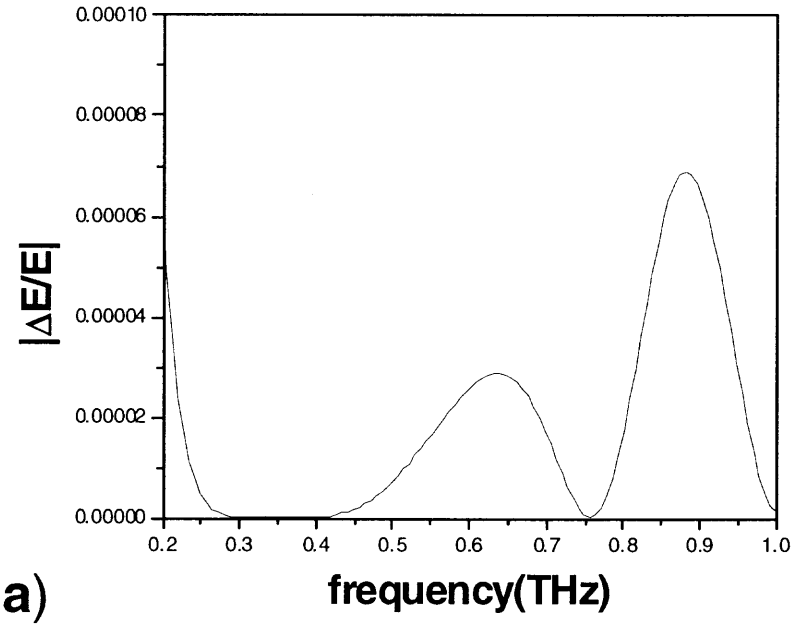

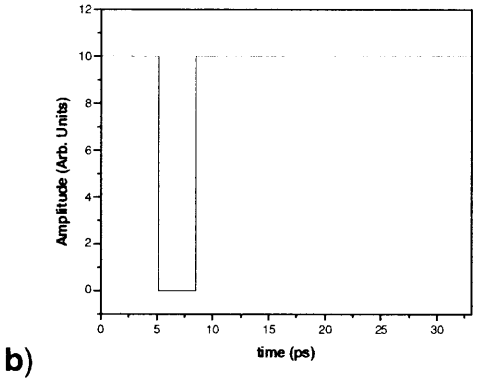

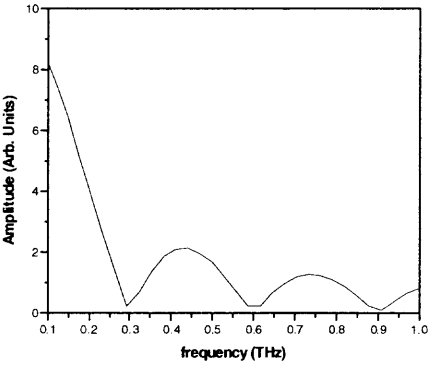

Figure 3.10. Errors associated with incorrect padding. a) Zero padded SWCNT differential transmission; b) Curve depicting slight offset between padding and data similar to SWCNT's in a); c) FFT of b), showing oscillations similar to the ones in a). Note that the differential transmission in a) is normalized to a linear scan, while c) is not.

3.7.2 Noise

The significant noise contribution to the time-domain signals required special attention to ensure that the corresponding spectral features were not attributable to noise in the time-domain signal. Fine scale time-domain features on the order of 100fs are noise since the THz detectors are not sensitive to electric field fluctuations on this time scale. These fluctuations, therefore, give an estimate of the noise contribution to the THz waveform.

In order to assess the effect of the time-domain noise on the frequency domain spectral features, Fourier transforms of different time-domain data sets, which were consistent with the noise level, were compared. These estimates as shown in Figure 3.11a, b, c were done by fitting a line through the variation of the noise level. Three estimates were made for each time-domain scan, that was representative of a fit though the top, the middle and the bottom of the largest peak occurring around 0ps. Based on the variation (done by analyzing the average variance of each fitted point to the raw data transforms) in the Fourier transforms for the SWCNT data (Figure 3.11a,b,c) over the range of 0.2-1 THz (Figure 3.10d,e), the error in the value of $|\Delta E / E|$ was assessed to be approximately 20%. A similar analysis suggested that the error in the magnitude of ion-implanted differential spectra (Figure 3.11f) was roughly 30%. Within these noise limits, the SWCNT sample exhibited a broad absorption in the 0.2-1 THz range, and the differential THz spectrum for the ion-implanted silicon sample exhibited a similar, but seemingly much broader absorption in the same range.

Another interesting outcome of the above assessment was that the presence of a narrow reduced absorption feature at or near 0.8THz could not be ignored, as can be seen in Figure 3.11d, e, f. This feature is not due to any type of interference effects and can

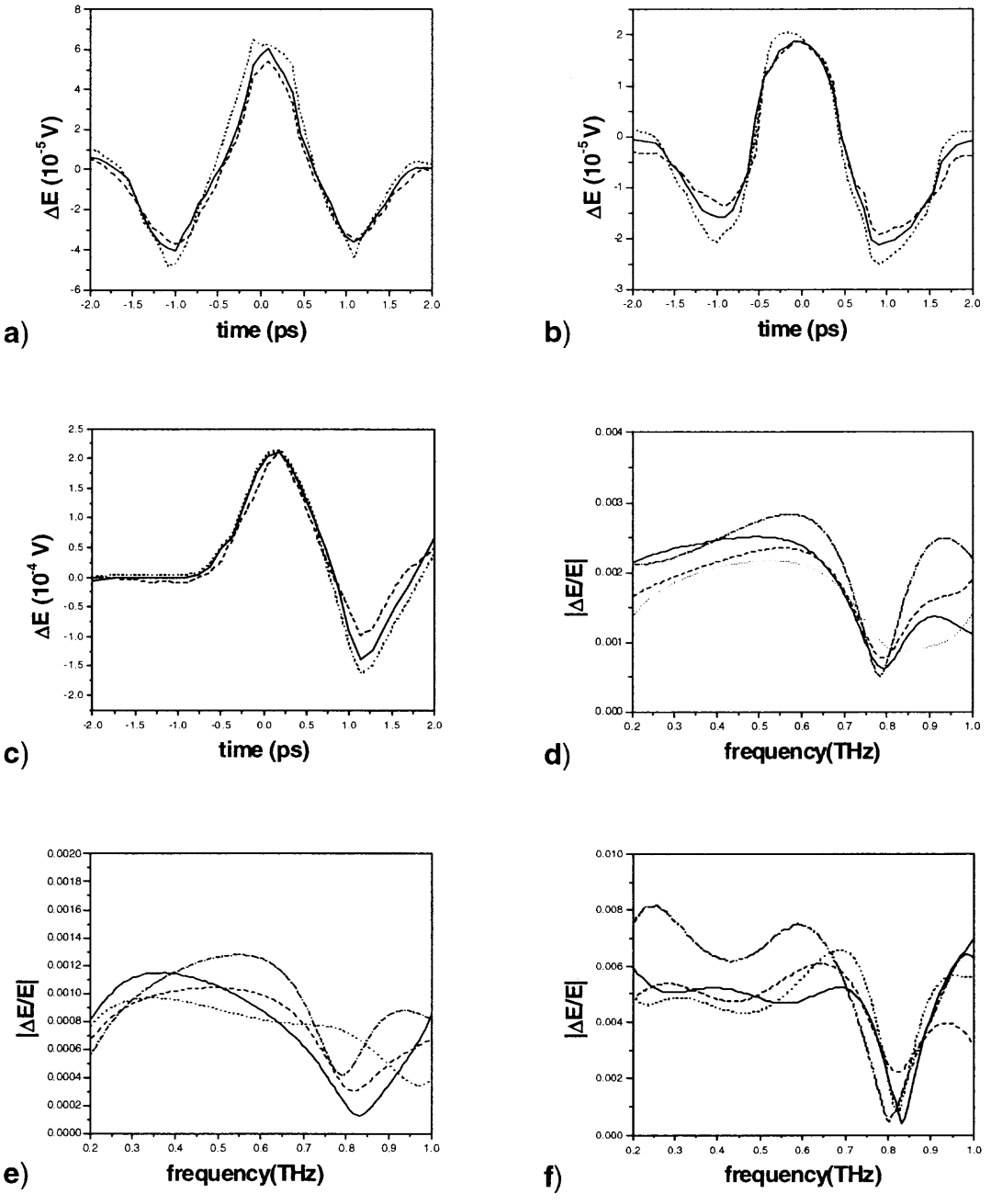

Figure 3.11. Various curves fitted through the noise level of Figure 3a, c, e, and their corresponding differential transmission. The dashed curve represent upper and lower extremes though the noise level while solid curve is a fit through the middle for a) high density SWCNTs; b) low density SWCNTs; c) Ion implanted Si nanocrystals; Differential transmission d) of curves in a; e) of curves in b; f) of curves in c. These fits allow us to estimate any uncertainty in the raw data analysis.

only be explained as an experimental artifact since it appears for both SWCNTs and Ion implanted Si nanoclusters. We believe that the low differential signal strength from the nanomaterials and the low antenna sensitivity at higher frequencies in the range from 0.1 to 1THz (see Figure 3.13) both contribute to the extent of this absorption feature.

3.8 Effective Dielectric and Drude Based Conduction Models

3.8.1 Effective Dielectric

Three composite structure models are the most common for calculating effective dielectric strengths of various mixtures of materials. Of these, the Maxwell-Garnett theory describes geometry where small particles are embedded in a host material. The Bruggeman geometry consists of two intermixed components (applied usually to intermixed components of different phases, such as one is crystalline and other is amorphous). And finally, an alternating layer composite geometry consisting of two dissimilar materials. In all the composite structures we assume that the distance between nearest neighbors of the constituents is much less than the wavelength of the probing radiation.

We applied Maxwell-Garnett (MG) theory which describes an effective dielectric constant for conductive (or doped semiconductive) particles embedded in a dielectric layer [91]. This model is applicable to our samples since Transmission Electron Microscopy (TEM) measurements showed that both the SWCNTs and Si nanoclusters were well separated and statistically distributed, implying that the dc conductivity was negligible. We treat the ion implanted Si nanocrystals as embedded particles in the fused silica substrate and the SWCNTs as embedded in a layer of air on top of quartz. We also

make the assumption that since the linear transmission measurements show no absorption by either nanocomposite, in the limit of our measurement uncertainty, we treat the dielectric function of the host and embedded material as solely due to high-frequency dielectric constant for each constituent. Then, the dielectric constant in this model is represented as:

$$\frac{\varepsilon-\varepsilon_i}{\varepsilon+2\cdot\varepsilon_i}=(1-X)\cdot\frac{\varepsilon_n-\varepsilon_i}{\varepsilon_n+2\cdot\varepsilon_i} \tag{3.10}$$

Where ε, ε_v, ε_i is dielectric constant for the effective nanocomposite layer, the nanomaterial itself, and the insulator, respectively. $1-X$ represents the fraction of nanomaterial (fill factor) in the effective layer. For the SWCNTs we assumed that the nanomaterial dielectric constant at infinity is around 2 [94] and that for the Ion-implanted Si nanocrystals, the dielectric constant, is the same as for bulk-silicon ($\varepsilon_\infty = 11.7$ [36]). The dielectric medium for the insulator in the case of SWCNTs was Air, and for the Ion-implanted Si nanocrystals was fused silica. When analyzing the effective dielectric using THz-TDS techniques, generally one would like to extract this right from the measured linear THz waveform. Then using, the Garnett model figure out the frequency dependent dielectric function of the nanotubes by using known values for the high frequency dielectric constant of the nanomaterial as well as the dielectric constant of the insulator, heeding to the dependence of the nanomaterial dielectric function to the fill factor parameter. Since we were not able to observe any appreciable change in the linear THz transmission with the samples at our disposal, instead of extracting the effective dielectric from the data, we approximated it in the high frequency limit using known values for the nanomaterial and host medium. Then fit the differential transmission in the frequency

domain using Kramers-Kronig based analysis on the differential transmission coefficient. By varying the Drude parameters, Lorentz parameters and fill factor, we could only come up with a given range for each value that would fit the data with the few constraints at our disposal, such as photoexcitation intensity.

3.8.2 Drude Model

In Chapter 2 we discussed the different types of models that can account for the conductivity of various semiconductors. The low frequency resolution of our measurements and the noise variation as shown in Figure 3.11 leads us to examine the nanocomposite under a variety of conduction theories. If the tubes are predominantly semi-metallic than the Drude model would be appropriate since the pump pulse would excite carriers into the conduction bands where they can be treated as free. In the free carrier Drude Model, the frequency dependent dielectric function of the nanocomposite film is modeled as [94]:

$$\varepsilon_{eff}(\omega) = \varepsilon_{eff}^{\infty} - \frac{\omega_p^{\,2}}{\omega(\omega + i/\tau)} \tag{3.11}$$

Where, $\varepsilon_{eff}^{\infty}$ is the effective dielectric constant of the material at high frequencies (Given by MG model), $1/\tau$ is the collision frequency, $\omega_p = (4\pi Ne^2/m)^{1/2}$, *N, e, m* are the plasma frequency, carrier density, charge and mass of the free carriers, respectively. Upon visible excitation, the free-carrier contribution is changed by the photo-excitation of free-carriers. Our attempts to fit our data to a Drude model [92] demonstrated that the photoexcited carriers do not exhibit Drude-like conductivity for two reasons. The Drude model can not explain the hump-like feature in the differential transmission of SWCNTs

(Refer to figure 3.14 to see shape of Drude-based differential transmission). But most importantly, the carrier density required to generate such a response as was observed with SWCNTs and Ion Implanted Si nanocrystals are not justified by our visible pump-pulse energies. Since the photogenerated carrier density is coupled to the fill factor, the maximum carrier density that you can have in the film is when the entire nanocomposite dielectric is due to only the SWCNTs (fill factor =100%). Given that the spot size of our pump beam, laser repetition rate, pulse duration, and thickness of the nanocomposite layer were 1cm, 82 MHz, 100fs, and 100nm respectively and assuming that 1 photon exactly generates 1 free-carrier, then at our excitation level of 0.4nj per pulse, we will generate $N \sim 8x10^{14}cm^{-3}$. However, to reproduce the magnitude of the differential response as seen in Figure 3.8, with just the pure Drude model, we would need to generate at least $10^{18}cm^{-3}$ at a fill factor of 100% corresponding to an excitation level of 10μj per pulse. Once you take into account that the sample transmits most of the excitation (i.e. transparent) and that the fill factor is less than 100%, then the carrier density reduces to about $10^{12}cm^{-3}$. As discussed later in section 3.11, modifying this carrier density in the range up to but less than $10^{18}cm^{-3}$ has no effect on the curve fitting. The constraints discussed here also hold for the Ion-implanted Si nanoclusters, since the observed differential spectrum is comparable in magnitude to the SWCNTs, and the only difference is that the dielectric constant at high frequency is larger by less than order of magnitude, and does not impact the curve fitting.

In contrast to these measurements for which we can not explain with a pure Drude response, visible pump/THz probe measurements of a CdSe nanoparticle system exhibited a Drude-like response [93]. In addition, visible pump/THz probe measurements

carried out on μc-Si:H and ac-Si:H shows a non-Drude type behavior reflecting the influence of disorder in the conductivity [85].

3.8.3 Drude + Lorentz Model

Since the carrier density required to fit the observed differential transmission for both SWCNTs and Ion implanted Si nanoclusters was far beyond the experimental parameters under a pure Drude model, we next assumed the large response to be due to localized states in the nanomaterial and incorporated a Lorentz-type contribution to the dielectric function. In this model, the dielectric function of the nanotubes can be expressed as:

$$\varepsilon_{eff}(\omega) = \varepsilon_{eff}^{\infty} - \frac{\omega_p^{\,2}}{\omega(\omega + i/\tau)} - \sum_{m=1}^{M} \frac{\Omega_m^{\,2}}{(\omega^2 - \omega_m^2) + i\Gamma_m \omega} \qquad (3.12)$$

where Ω_m, ω_m, Γ_m, and M are the oscillator strength, resonant frequency, resonant width, and number of resonances, respectively. This model assumes that the carriers not only move freely but also are quasi-elastically bound to atoms, which are then excited by the THz probe energy and are forced to vibrate. It was noted earlier that SWCNTs exhibit a far-IR gap at 10meV (~2.4 THz), and FTIR measurements on baked and unbaked SWCNT samples showed Lorentz-like feature at 2.4THz [81]. This feature was also incorporated in our example spectrum as shown in Figure 3.3. Drude + Lorentz like behavior have also been observed under linear THz transmission (no visible pumping) for very thick SWCNTs films (thickness on the order of microns) [94]. In this combined effect model, the fill factor will also affect the strength of the resonance. For example, changing the fill factor from 1% to 100% will increase the required oscillator strength to fit the magnitude of the differential transmission by a factor of at least 10, keeping the carrier density at a level below $10^{18}cm^{-3}$. The one, weak, external constraint we have on

the oscillator strength is that its magnitude be comparable to that of other resonances which have been observed at higher frequencies such as that at 2.4THz.

3.8.4 Drude-Smith Model

When a system (such as a group of clusters or atoms) have some degree of disorder (randomness) some of the states become localized, often referred to as Anderson localization. The energies of these localized states occur in the bandgap of the system and are predominant in 1D systems. The degree of this localization can be explored under a Drude-Smith approach. Here the equation that governs the conductivity is given by [48]:

$$\sigma(\omega) = \frac{{\omega_p}^2 \tau}{(1 - i\omega\tau)}\left(1 + \frac{c}{1 - i\omega\tau}\right) \tag{3.13}$$

Where, the value of c is associated with the degree of back scattering a carrier undergoes after a collision. It has a value of $-1 < c < 0$, where $c = 0$ gives the Drude Model and $c = -1$ gives Anderson localization. An example of such a measurement done with visible pump/THz probe spectroscopy was seen with InP nanoparticles [48]. The researchers could not explain their results by a simple Drude conductivity behavior. They concluded that a Drude-Smith model, which included a parameter for the degree of carrier backscattering, produced a satisfactory fit to the InP data. We conclude that the Drude-Smith model was insufficient in explaining the magnitude of the observed differential transmission for similar reasons as outlined for the Drude model.

3.9 Modeling the Observed Differential Transmission

In analyzing the SWCNT and ion-implanted silicon data, we conclude that we can only model the observed broad features in the differential transmission with the presence of

localized states [81,92,94] done by incorporating a Lorentz-type contribution to the dielectric constant of the material. Since the unpumped transmission through our samples is featureless (Figure 3.6b), we assume that the contribution to the differential transmission is due to photo-excited carriers only (Note: There may be a feature at around 2.4THz but we cannot tell due to our limited bandwidth). One can approximate $\varepsilon(\omega)$ as $\varepsilon(\omega) + \Delta\varepsilon$, where $\Delta\varepsilon$ is due to the photo-excited carriers. In this model, $\varepsilon(\omega)$ is the effective dielectric function of the nanocomposite and the change in dielectric function of the nanomaterial can be expressed as:

$$\Delta\varepsilon(\omega) = \frac{4\pi \cdot \Delta N \cdot e/m}{\omega(\omega + i/\tau)} - \sum_{m=1}^{M} \frac{\Omega_m{}^2}{(\omega^2 - \omega_m{}^2) + i\Gamma_m\omega} \qquad (3.14)$$

where $\Delta N, \Omega_m$, ω_m, Γ_m, and M are the photo-excited carrier density, oscillator strength, resonant frequency, resonant width, and number of resonance, respectively. Of these parameters, ΔN is estimated from the visible pump power density, assuming 1% of light being absorbed. Varying τ and ΔN over the range of 10^{-15}-10^{-10} s^{-1} and 10^{8}-$10^{17}cm^{-3}$, respectively, while keeping the fill factor fixed at 100% does not affect the curve fitting. The fits were mostly sensitive to the Lorentz parameters but not to the Drude model parameters. Even though τ does not effect the curve fitting over these range of values, in all the fits we used $\tau = 1x10^{-11}s$, corresponding to an electron mobility of $20{,}000cm^2/V/s$ as has been reported for SWCNTs that have lengths up to few microns [95]. Using equation 3.14 and applying it to the dielectric constant of the nanoparticles, the differential THz transmission through the sample can be modeled. Assuming a bi-layer medium (nanocomposite on a quartz substrate), one can write the transmission of the

electric field at normal incidence in the form [96]:

$$\frac{E}{E_o} = \frac{8n_s n_n}{(n_s + n_n)\cdot(1+n_n)} \cdot \frac{e^{i(n_s-1)k_o L}}{1 - e^{i2n_s Lk_o}\left[(n_n - n_s)\cdot(1-n_n)\right]/\left[(n_n + n_s)\cdot(n_n+1)\right]} \tag{3.15}$$

where n_s is the index of refraction of the substrate, n_n and L are the index of refraction and thickness of the nanocomposite layer and $k_o = c/\omega$ where c is the speed of light in a vacuum. For our experimental configuration, the THz differential signal is proportional to $\Delta E = E_p - E_u$ where E_p denotes the transmitted electric field through the material under optical illumination, E_u represents the electric field transmission without illumination, and E_o is the incident electric field. In the limit of a small photo induced change in the nanotube's index of refraction ($n_n = \sqrt{\varepsilon} = n_o + \Delta n$, where $\Delta n = \Delta\varepsilon / 2\cdot\varepsilon_\infty$), the differential THz signal can be expressed using equation 3.15 to first order in Δn:

$$\frac{|\Delta E|}{|E_o|} = \left| \left[1 + \frac{\Delta n}{n_n}\right] \cdot \frac{[1 + ik_o L\Delta n]\cdot\alpha_o}{[(n_n + n_s + \Delta n)\cdot(1 + n_n + \Delta n)] - e^{i2n_s Lk_o}[(n_n - n_s + \Delta n)\cdot(1 - n_n - \Delta n)]\cdot[1 + ik_o L\Delta n]} - 1 \right| \tag{3.16a}$$

with,

$$\alpha_o = [(n_n + n_s)\cdot(1+n_n)] - [(n_n - n_s)\cdot(1-n_n)]e^{i2n_o Lk_o} \tag{3.16b}$$

The analysis may be simplified if reflections from the front and back surface of the substrate are neglected. This is justified due to the limited time window of our measurements (we only scan 2ps after the peak of the THz pulse) we do not "see" reflections from the back of the quartz or fused silica substrate. Since, the nanocomposite layer is thin compared to the THz wavelength, reflections from the front and back surfaces of the nanocomposite film are included in the above calculation.

Using equations 3.14 and 3.16, multiple Lorentz parameters (Table 3.2) are extracted from the differential spectra that range from 0.2 to 1THz. The spectra could also be modeled with one Lorentz parameter (Table 3.3) in a reduced spectral range from 0.2 to 0.7THz (see section below as to why the spectral region is reduced). In Figure 3.12a, b (multiple Lorentz parameters) and Figure 3.15a, b (one Lorentz parameter) the Fourier transform of the raw data is compared to the Lorentz fits. Note: As mentioned before, depending on the fill factor (a value between 1% and 100%) the oscillator strength can change by a factor of at least 10 for each nanocomposite type (Table 3.2 and 3.3 only lists values extracted for a fill factor of 5%).

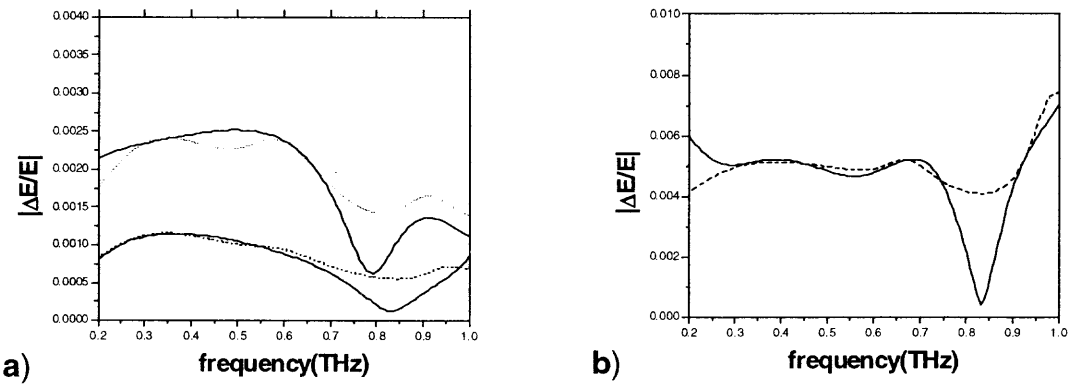

Figure 3.12. Multi-parameter Drude + Lorentz Fits for a) Upper solid curve: high density, lower solid curve: low density SWCNTs; b) Ion implanted Si nanocrystals; dashed lines represent fits. Lorentz parameters used in the model are shown in Table 3.2. Drude parameters for all fits were $\tau = 1x10^{-11}s$, $\Delta N = 1x10^{12}cm^{-3}$, with Garnett parameter of 1-X=0.05, for upper curve SWCNTs, 1-X=0.02 for lower curve SWCNTs, and 1-X=0.05 for Ion implanted Si.

Table 3.2: Extracted Lorentz Parameters of Differential THz Spectra from 0.1 to 1THz

Sample	*M*	$\omega_o(cm^{-1})$[a]	$\Omega_m(cm^{-1})$	$\Gamma_m(cm^{-1})$
SWCNT Fill Factor:5%	1	13	920	100
	2	20	330-460[b]	50
	3	31	330	33
3-4 nm Ion Implanted Si Fill Factor:5%	1	16	1190	200
	2	22	200	26
	3	33	430	26

3.10 Spectral Sensitivity

The differential transmission curves as shown in Figure 3.8 exhibit a dip around 0.8 THz, which is far more pronounced in the Ion Implanted Si nanocrystals than in SWCNTs. As mentioned before, we believe this dip to arise from the limited power we have in that spectral range as can be see from Figure 3.13. We note the fact those two vastly different nanocomposites - SWCNTs and Ion implanted Si nanocrystals, both exhibit a dip in the same frequency range suggesting that this feature is an artifact. To be able to accurately predict whether this feature were real would require us to repeat these scans with a THz system that has greater bandwidth such as one based on electro-optic detection with ZnTe

[a] 33 cm^{-1} = 1 THz

[b] This oscillator strength was different for the two different scans through SWCNTs

crystals being used to generate and detect the THz transient. The best and only solution available to us was found by only considering the spectral range up to 0.7THz.

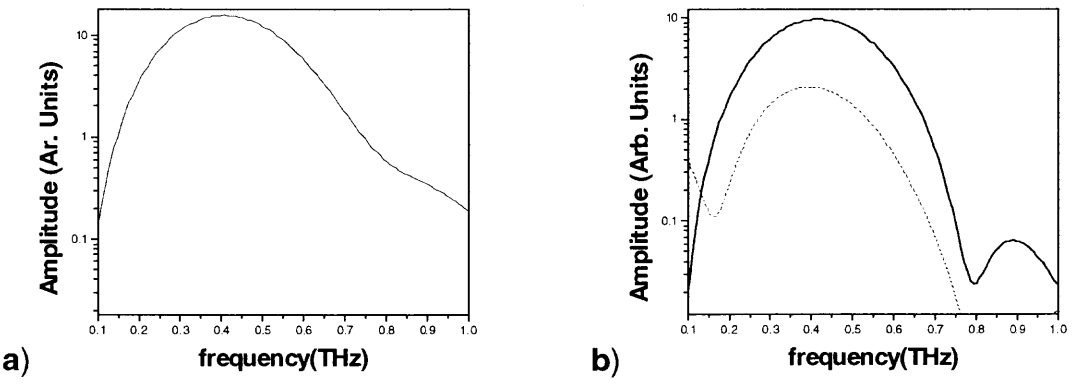

Figure 3.13. Spectral amplitude of THz transmission through a) Air, and b) SWCNTs on quartz, solid line is representative of the denser nanotubes and dashed line of the less dense area. Note the cutoff near 0.75 THz which suggests that the differential (pump on-pump off) scans should be cutoff near this frequency.

3.12 Discussion and Results

Differential transmission in the frequency domain proved useful when analyzing THz transmission under delayed pump beam. The optically generated carriers respond to the probing THz radiation and therefore, modify the THz transmission in the visible pump/ THz probe geometry. Both SWCNTs and ion-implanted samples, which were used in our experiments, exhibit nonlinear characteristics of short-lived photo-induced carriers [88,90].

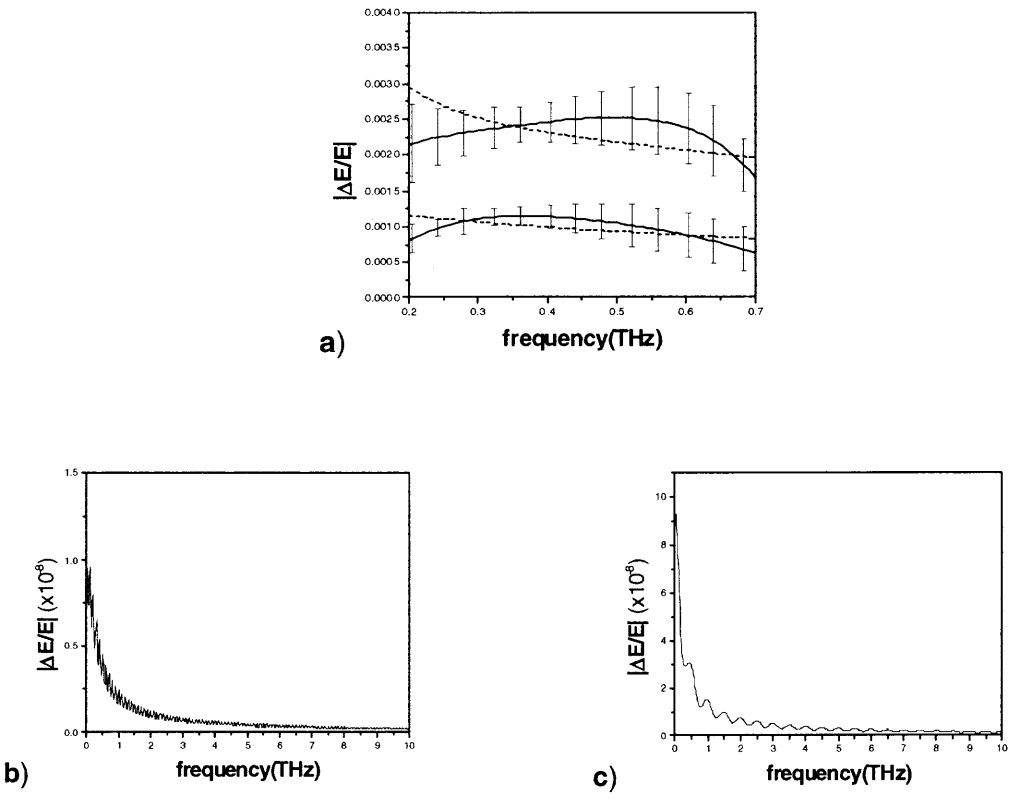

Figure 3.14. Fits using a Drude only model to raw data differential transmission curves for a) SWCNTS, bold lines are the raw data while the dashed lines are best fit curves; error bars show the fluctuation in the raw data due to noise as described in the analysis. Drude parameters for top fit were $\tau=1x10^{-11}s$, $\Delta N=1x10^{18}cm^{-3}$ while for bottom $\Delta N=1x10^{12}cm^{-3}$. The fits for b) SWCNTs and c) Ion Imp. Si nanocrystals plotted over longer frequency range.

Initially, in the case of the ion-implanted silicon, we compared the data to what we would expect from bulk semiconductors. The differential transmission spectra of the bulk silicon (Figure 3.9b) can be fit using only a free carrier Drude model. Similarly to its bulk counterparts, InP nanoparticles [48] also exhibited photo induced Drude-like behavior. The differential transmission data for our nanocomposite samples clearly indicate the necessity for a model beyond the Drude-only or, Drude-Smith model. Due to the limited power density at high frequencies the spectra was cut-off at 0.7THz, further narrowing

our spectral region of interest. The adjusted spectra are shown in Figures 3.14, and 3.15. The large uncertainty in Figure 3.15 and the reduction of the spectra width, coupled with our poor resolution resulted in less constraint on the fitted parameters. Even still, a simple free-carrier dispersion model could not explain the large signal observed with our samples when pumped with relatively low pump intensities (< 0.4nJ) for any fill factor describing the effective dielectric. Even when we assumed a value for τ in the analysis that corresponds to one reported result that semiconducting nanotubes can have mobility up to 20,000 $cm^2V^{-1}s^{-1}$ [95] corresponding to $\tau = 1x10^{-11}s$, the models still could not account for the observed differential response. This value was kept the same for the Ion-implanted Si nanocrystals, but we note again that changing the scattering time from 10^{-15}-10^{-10} s^{-1} had little or no effect on the curve fitting for both samples. The model is dependent on the Lorentz parameters and we would need to change the Drude parameters by at least 5 orders of magnitude to obtain a fit of the same magnitude as the data. The fill factor is important in determining the relative oscillator strengths and one can not determine the oscillator strength in these materials accurately without some external constraint on the fill factor. For example, while we were not entirely successful in estimating the nanotube density visible through SEM images as shown in Figure 3.4 (although we mention that a fill factor of 5% is certainly plausible) we can approximate the fill factor from the Ion implanted Si sample since we already know the depth and implantation dose of the Silicon atoms. Using Large Scale Statistical (LSS) theory [97], we estimate the Si atoms in 3-4nm Silicon nanoclusters throughout the 300nm thick implantation layer to occupy at most 10% of the available space, assuming each silicon atom to have a diameter of 2Å. Thus, our estimate of 5% is within expectation.

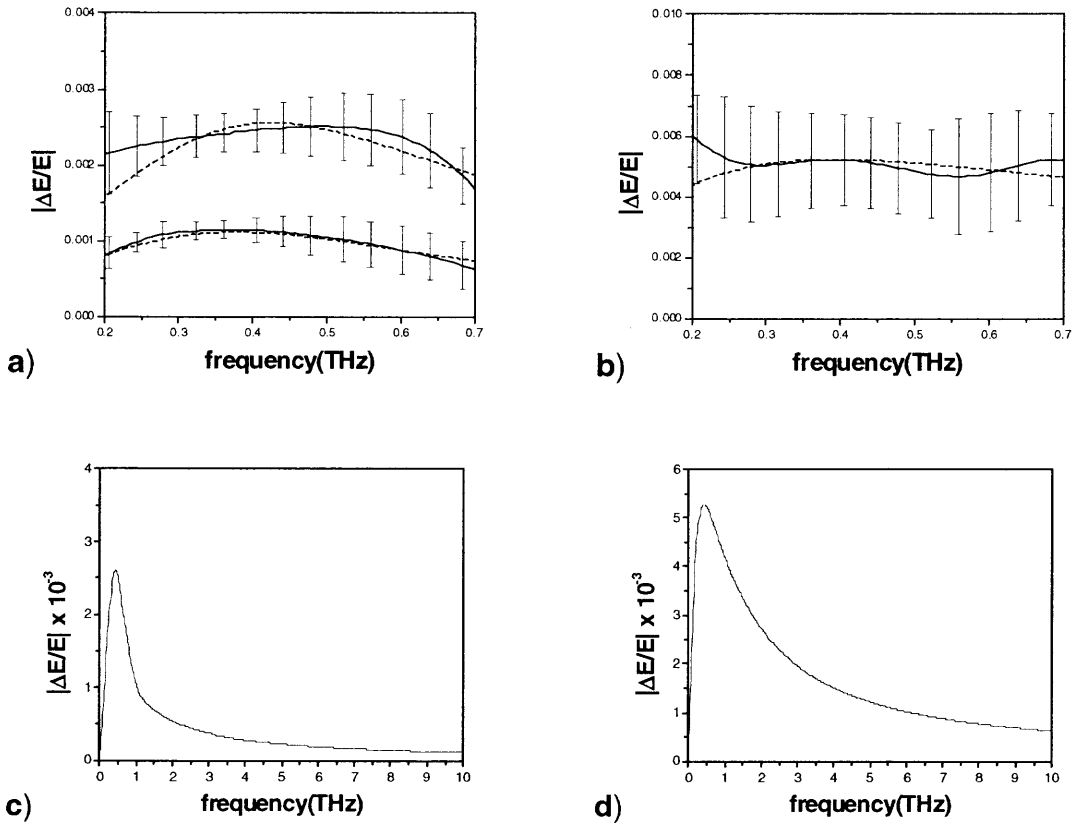

Figure 3.15. Fits using a Drude + Lorentz model to raw data differential transmission curves for a) SWCNTs, b) Ion implanted Si nanocrystals. Bold lines are the raw data while the dashed lines are best fit curves; error bars show the fluctuation in the raw data due to noise as described in the analysis. Drude parameters for all fits were $\tau = 1x10^{-11}s$, $\Delta N = 1x10^{12}cm^{-3}$, with Garnett parameter of 1-X=0.05, for upper curve SWCNTs, 1-X=0.02 for lower curve SWCNTs, and 1-X=0.05 for Ion implanted Si (Lorentz parameters are given in Table 3.3).Figures in c), d) show fit over longer frequency range.

Table 3.3: Extracted Lorentz Parameters of Differential THz Spectra from 0.2 to 0.7THz.

	M	$\omega_o(cm^{-1})$	$\Omega_m(cm^{-1})$	$\Gamma_m(cm^{-1})$
SWCNT	1	16	1180	130
3-4 nm Ion Implanted Si	1	18	1420	260

When other models were considered, the results showed that while the differential spectra shape of a Drude-Smith model would be similar to the spectral shape of the Lorentz fit of Figure 3.15a, the required pump power and photo induced carrier density to reproduce the experimentally observed $|\Delta E/E|$ strongly suggested that the Drude-Smith model was not the appropriate approach.

Additional motivation behind applying the Drude + Lorentz model lied in the fact that Lorentz-like states have been observed for SWCNT samples with relatively large oscillator strengths [71] from $30cm^{-1}$ to $12000cm^{-1}$. Also, since the scales in which the carriers are confined effect their available energies [98,99], the complex structural environment of the tubes in the bundle coupled with structural deformations of the bundle itself could lead to the observed resonance at the low end of the spectrum. There is no evidence in literature that there should be a resonance at such a low frequency. Resonances that appear to the lower end in frequency range ($<200cm^{-1}$) tend to be due to RBMs. For SWCNTs these modes have been calculated [100,101]:

$$\omega(cm^{-1}) = \frac{223.75}{d(nm)} \tag{3.17}$$

thus for SCWNTs of diameters less than 1nm we don't expect to see such resonances. However, in metallic nanotubes, there is a mode due to optical phonons at $17cm^{-1}$[100], but in general the width of these RBMs are usually very narrow ($<10cm^{-1}$[100]). At room temperature we don't expect to see these modes since they are far below the corresponding frequency ($200cm^{-1}$) and have broadened so much that their effects can be safely neglected. When the system is not in thermal equilibrium as is the case under photo excitation, even at the low excitation levels we pump at (< 0.4nj), these low

frequency resonances are overpowered and broadened to the point where they are not seen anymore.

Figure 3.15a shows the SWCNT data modeled with a single Lorentz state at 0.5THz. The relatively large oscillator strength ($1180cm^{-1}$) and width ($130cm^{-1}$) of the Lorentz state is consistent with Lorentz-like states that were observed in linear spectroscopic measurements. Moreover, density variations of nanotubes on the sample (Figure 3.15a) (varying the nanomaterial concentration from 2% to 5%) does not affect the general shape of the response as observed with the THz probe. Recently, linear THz spectroscopic measurements (no visible pump) that had been done on SWCNT mats with thickness on the order of microns showed evidence for localized absorption at 0.65THz very close to our estimate of 0.5THz [55]. However, in another case [94] this feature at 0.65THz was ruled to be a larger part of a broader absorption at 2.4THz, which has been independently observed with FTIR measurements on similar samples [71].The ion-implanted differential spectrum of Figure 3.15b was fit using one Lorentz state as shown in Table 3.3.

Because of the limited constraints we had on the range of values the Lorentz parameters could have, we could not rule out the possibility that the differential spectrum is the tail of spectrally broadened Lorentz state whose center frequency lies outside of our 0.2-0.7THz spectral band. In ion implanted Si nanoclusters there is no evidence in the literature to confirm the existence of this resonance; however, similar arguments pertaining to structural confinement of excited carriers could be made. In the case of SWCNTs, however, the resonance could be a strong phonon mode that is due to interactions between the tubes in bundles with surface effects or the sphere like catalysts

in the medium as can be seen in Figure 3.4 that were left over after acid purification. These questions can only be answered when experiments can be conducted on highly ordered SWCNT mats with appreciable thickness so that one can compare linear and differential measurements to see evidence for these localized effects.

3.13 Time-Resolved Dynamics in SWCNTs

Efforts were made to try to resolve the carrier dynamics in the SWCNT sample. As mentioned before we can not resolve the lifetime of photogenerated carriers in these materials because we expect the carrier recombination time to be less than the duration of the THz pulse (See section 2.6.2). 2D scanning methods can be utilized but if the recombination lifetime is on the order of 300fs as had been measured with visible pump/visible probe measurements than we would additionally have to factor in limitations due to the receiver antenna response time (<300fs). Due to the lengthy averaging involved it proved difficult to obtain good signal to noise ratio, thus the experiments were unsuccessful.

3.14 Other nanocomposites

Measurements (linear transmission as well as Visible Pump/THz Probe Spectroscopy) we conducted on MWCNT samples, laser ablated Si on quartz and laser ablated Ge on quartz as well as the SWCNTs grown in an opalline matrix on quartz did not reveal any evidence for THz absorption. Thus we were unable to deduce to any extent the electronic characteristics of these samples.

In the case of the SWCNTs in the opalline matrix we mentioned that these tubes

are in smaller bundles and are far well separated than the SWCNTs as grown on quartz substrates. As was explained before, interactions between individual tubes in bundles and/or structural deformations modify the DOS. In particular we mentioned that the sharp peaks in the DOS broaden due to Van der Walls interactions. If the broadening is on the order of the THz energy then the individual carriers can be confined to oscillate in this region. This could lead to the Lorentz like absorption we observed in these samples. This would also explain why we don't see any effects from the opalline samples since the tubes are presumably non-interacting or interactions were far fewer due to smaller bundles. However, we can not rule out that maybe the density of tubes in the opalline matrix is far less than in the samples we tested which would justify us not seeing a response from these samples.

In addition to the above samples we performed experiments on hexagonal silicon on quartz and CNTs in polymer on quartz as well as CNTs on quartz. The hexagonal silicon structure was verified by electron diffraction patterns. The CNTs are thought to be of the semiconducting kind due to SERS/HRES-TEM measurements on similar samples. The only difference being that the CNTs in polymer are well separated compared to the CNTs on quartz (assumed to be in bundles). The results are documented in Appendix B.

CHAPTER 4

$Si_{1-x}Ge_x$ and High-K dielectrics

4.1 Overview

In this chapter we review usefulness of THz spectroscopy on probing electrical properties of semiconductors. We apply reflection based THz-TDS to extract the mobility of $Si_{1-x}Ge_x$ composite wafers as well as HfO_2 (high-κ dielectric) and SiO_2 deposited on p-type silicon wafers. We also study HfO_2, SiO_2 structures under THz-TDS and visible pump/THz probe using a CW Ar+-Ion laser. From our visible pump/THz probe measurements we model the structures with two different multilayer models. Emphasizing one model, our measurements show that the interfacial defect density for HfO_2/Si is greater than SiO_2/Si and we are able to predict this density knowing SiO_2/Si interfacial defect density.

4.2 Introduction

The frequency dependent optical parameters for doped semiconductors are important and need to be assessed for many device design applications. Frequency dependent characteristics such as mobility, conductivity, index of refraction and others such as minority carrier lifetime determine the effectiveness of using one particular semiconducting material than another in applications which range from communications to high-speed computing.

The THz-TDS technique provides a non-contact method of determining these parameters. The pioneering studies of GaAs, silicon (Si) and germanium (Ge) were performed by Grischkowsky et al. [102,27,103]. THz based methods were also successfully used for the investigation of the carrier dynamics in semiconductors. For this purpose, visible pump/THz probe or THz emission spectroscopy is used. In addition, the number of studies concerning the influence of magnetic fields has also gained ground using THz spectroscopy [104]. In this area, traditional electrical measurements done on wafers utilizing phenomena such as the Hall Effect can be duplicated with THz spectroscopy. Actually, the THz Hall Effect has proven to be an accurate measurement technique [105]. It utilizes the fact that the polarization of a THz beam focused on the sample under a magnetic field will rotate while passing through the semiconductor.

4.3 THz-based Methods

Tools in the THz regime can be very useful to understanding the electrical properties of semiconductors since parameters like the scattering rate and plasma frequency are on the order of the THz probing frequency. According to the simple Drude model of conduction, the key parameters that determine the free carrier dynamics in a material are the plasma frequency and the carrier scattering time. Since the values of the plasma frequency (ω_p) and 1/scattering time ($1/\tau$) are in the domain of THz frequencies, the measurements should be performed in this frequency range. Some examples of successful measurements include characterization of doped silicon (see Figure 4.1), gallium nitride and other semiconductors [106] using THz spectroscopy in transmission. However, depending on the doping level and the thickness of the sample, the transmitted pulse may be so severely

attenuated that THz-TDS cannot be used. For this case THz-TDS in reflection would have to be performed (see Figure 4.2). Initial work in this area was done on doped semiconductors [107] and extended to measuring layer thicknesses by analyzing the reflection off undoped InSb from 0.1 to 1.1 THz, as a function of temperature from 80 to 260K. Here, the researchers were able to successfully obtain values of the mobility and carrier concentration over this temperature range [108].

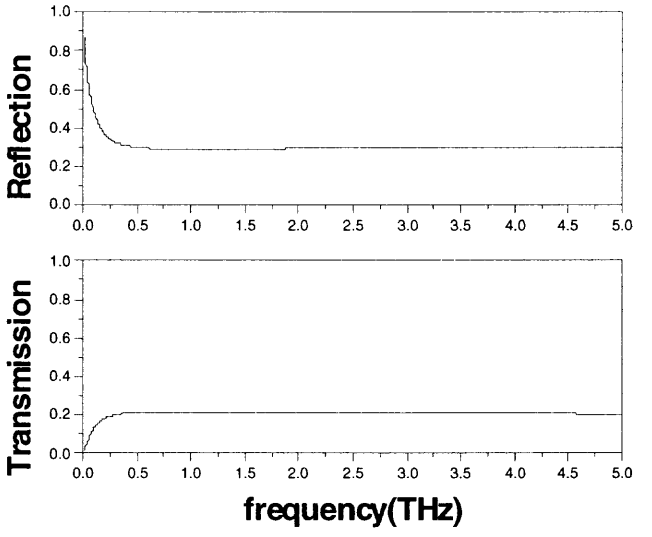

Figure 4.1. Drude based model of Transmission and Reflection through p-type silicon wafer. The Drude parameters were N_p=1.46x10^{16}cm^{-3}, τ = 1x10^{-13}s corresponding to μ_p=425cm^2/V/s for $m_p^* = 0.38m_o$. Plasma frequency at 1.759THz.

THz based methods have also been successfully implemented for the investigation of ultrafast processes in semiconductors. For this purpose, the optical pump/THz probe or THz emission spectroscopy is used [25,109]. All the aforementioned success achieved with THz-TDS makes it a viable technique towards analyzing the properties of newly developed semiconductor heterostructures.

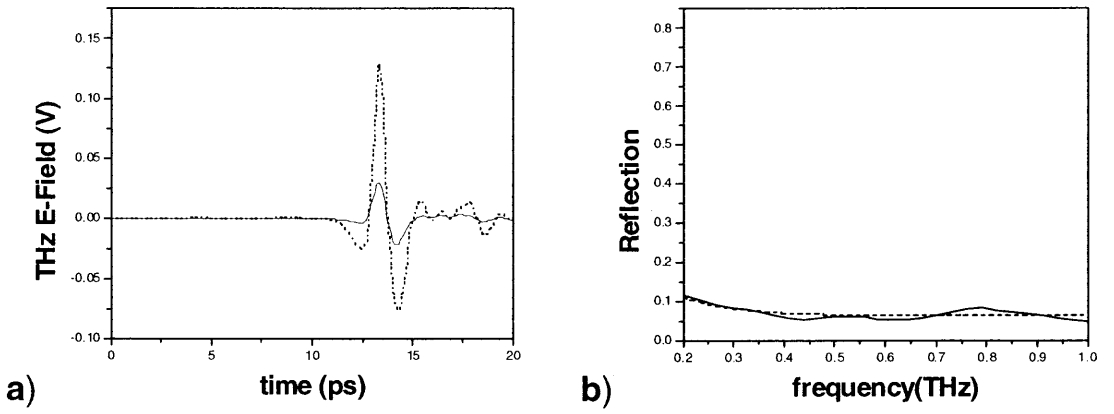

Figure 4.2. THz-TDS reflection off silicon wafer. a) Solid line is the scan from silicon, dashed line is the scan from a gold mirror that serves as the negative sample (see chapter 2, Figure 2.6). b) Reflection (FFT of sample /FFT of negative). Reflection was fit with Drude model, fit parameters were, $N_e = 4.8 \times 10^{14} cm^{-3}$ and $\tau = 1.5 \times 10^{-13}$ s for n (Si) =3.4 and assuming $m_{eff}^* = 0.26 m_e$.

4.4 $Si_{1-x}Ge_x$

Technology based on silicon has dominated the device industry due to features like low power dissipation, high-integration levels, high cost-effectiveness, and overall reliability in micro and nano-electronics. However, low mobility of electrons and holes in silicon limits its use to low-frequency regime. Applications like mobile communications, which require faster response and better conductivity, require III-V materials like GaAs (and others) to meet its demands [110]. In general, the increased sophistication of electronic devices is increasing the demand for advanced semiconductor technologies. Hybrid and exotic structures of materials are being explored to be the suitable platform from which these devices can be built.

Strained layers like epitaxially grown silicon and silicon-germanium alloys dramatically improve mobility, and therefore the performance of the device. Silicon germanium is a compound element whose electronic characteristics are defined by the

relative concentration of one to the other ($Si_{1-x}Ge_x$), x being the concentration. SiGe is remarkably faster than regular silicon semiconductors and its properties can be utilized in several ways. One reason for the improvement in performance is mainly due to the differing atomic diameters of each element. Larger germanium atoms fuse with smaller silicon atoms to form a "strained layer." The inter-atomic tensions within the layer drastically increase charge carrier mobility and hence improve the conductivity of the silicon germanium compound.

A different method of obtaining a strained layer with SiGe can be found by fabricating Strained-Si substrates using multiple epitaxial thin film growth steps towards forming a stack of films on the silicon substrate. The first film grown on the substrate is a Silicon Germanium ($Si_{1-x}Ge_x$) heterostructure layer, used as a strain introduction layer. Next, at least a 10nm thick silicon layer is epitaxially grown on the $Si_{1-x}Ge_x$ layer. Since, the lattice spacing of the $Si_{1-x}Ge_x$ layer is different than that of the Si layer grown on it, the atoms of the grown Si layer to adjust to match the lattice spacing of the $Si_{1-x}Ge_x$ layer. The Si atoms try to conform to the layer on the bottom causing a biaxial tensile strain in the silicon lattice, and thus stretching the lattice in the lateral direction. The introduction of the strain into the epitaxial Si increases the effective mobility of the carriers in the strained-Si layer. Strain can also be introduced by reversing the layers so that the $Si_{1-x}Ge_x$ layer is formed on top of the epitaxially grown strained silicon.

This mobility enhancement is observed usually in Metal-Oxide-Semiconductor Field-Effect Transistor (MOSFET) devices due to conduction band energy splitting caused by an applied electric field [111]. As these energy levels are repopulated, the carriers are now at a lower energy, reducing the effective mass and increasing the

effective mobility. The amount of band splitting and the energy band gap throughout can be calculated based on the percent of Ge contained in the relaxed $Si_{1-x}Ge_x$ layer [112].

For example, room temperature mobility in silicon MOSFETs (Metal-Oxide-Semiconductor Field-Effect Transistor) tend to be around $300cm^2V^{-1}s^{-1}$ for electrons, and less than $100cm^2V^{-1}s^{-1}$ for holes. In the case of SiGe, where in one study the electron transport properties were measured at 300K and 77K, record mobility of 2,830 and 18,000 $cm^2V^{-1}s^{-1}$ respectively, had been obtained [113]. Although, on average, measurements for the mobility of SiGe wafers measured with either poly-silicon gate contacts or gold gate contacts utilizing Hall techniques show electron mobility on the order of 1000 $cm^2V^{-1}s^{-1}$ that gradually decreases for applied electric field strength (MV/cm) [114]. This is still a much larger value than obtained for doped silicon wafers. The channel thickness in these measurements is not accurately known, but is predicted to be less than 10nm thick.

4.5 SiO_2/HfO_2

Over the years, the trend towards smaller sizes in MOSFETs and other transistors has brought about substantial improvements in overall device performance. However in the next few years, as mentioned in the annual forecast: International Technology Roadmap for Semiconductors (ITRS, 2003 Edition), the use of a conventional Si based MOSFET architecture will be insufficient. The two main reasons is that the necessary drive current can not be achieved at the current 90nm node, and the other is that the gate dielectric scaled to that node will be an insufficient insulator leading to gate leakage. While the use of a strained-Si or strained-Si on a SiGe alloy as the channel will increase the mobility

resulting in a higher drive current [115], solutions for the gate dielectric are far more complicated.

4.5.1 SiO_2

SiO_2 has been the industry workhorse for many years. It exhibits extremely low defects when grown on Si substrate and therefore has little effect on the performance of the device. According to ITRS, the SiO_2 oxide thickness should be less than 2nm now to keep up with Moore's law. The fundamental limit for device scaling is related to the thickness of the oxide for which direct tunneling occurs. The consequences of this phenomenon are already observed with current MOSFET technology with SiO_2 as the gate dielectric scaled down to 1.3nm, where a high gate leakage current and reduced drive current limit the operation of the device and increase power consumption. To continue the trend towards smaller devices, materials other than SiO_2 have to be considered. We can prevent the gate leakage by using a dielectric material with a higher permittivity (high-κ dielectric) than SiO_2, since the material will have a smaller electric field under the same bias voltage. The relative permittivity of the high-κ oxide and the equivalent oxide thickness (EOT) are related by:

$$EOT = \frac{\varepsilon_{oxide}}{\varepsilon_{high-\kappa}} d_{physical} \tag{4.1}$$

Where ε_{oxide} is the dielectric constant of SiO_2, d and $\varepsilon_{high-\kappa}$ are the physical thickness and dielectric constant of the high-κ dielectric respectively.

4.5.2 HfO_2

Despite many efforts, a high-κ dielectric material that provides as perfect an interface with silicon as with SiO_2 has not been found. The factors that contribute to a poor interface between the oxide and the Si substrate are thermodynamic stability with silicon at elevated temperatures, the dielectric constant, and the conduction band offset. A large number of gate dielectric materials have been examined during the past few years, including metal oxides such as Ta_2O_5, TiO_2, HfO_2, ZrO_2, Y_2O_3, Al_2O_3, and La_2O_3. Of these, due to its adequate band-gap and conduction-band offset [116], Hf-based high-κ dielectrics have become a very promising candidate to replace SiO_2 in MOSFETs. Its dielectric constant around 25, thermodynamic stability with Si up to 950 °C and a conduction band offset of 1.5eV allow it to offer a sufficient barrier against electron tunneling with EOT as small as 10 angstroms. Developing all-optical methods to deduce how much this oxide will affect the mobility and other parameters is again of great interest to many in the industry.

4.6 Manufacturing Methods

The technologies (most common growth method is CVD) to produce these exotic materials are already incorporated in standard silicon processing methods making them favorable to the semiconductor industry. Already large manufacturers are building SiGe epitaxial growth systems with large productivity using low-pressure CVD vertical furnace techniques. The vertical structure of these wafers can be characterized as a Si substrate with a $Si_{1-x}Ge_x$ layer on top, above that is a layer where the Ge concentration

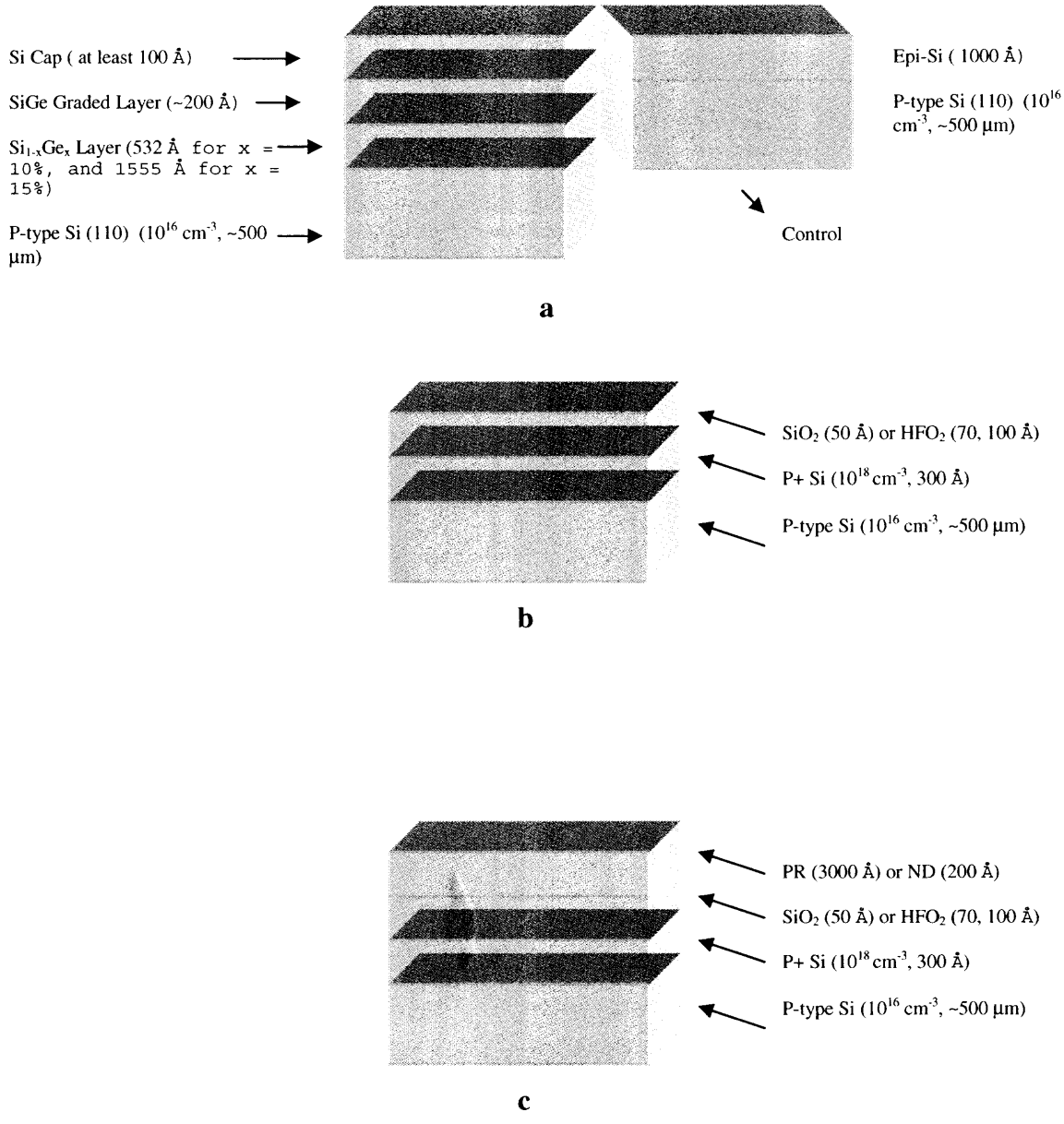

Figure 4.3. Wafer layered structure for a) Si1-xGex; b) dielectric and high-k dielectric deposited on p-type silicon; c) photoresist or nitride deposition protected dielectric and high-k dielectric deposited on p-type silicon.

is graded down to zero and finally the strained Si cap layer above it (see Figure 4.3.1a).

Techniques other than CVD used for production of the high-κ oxides include physical

vapor deposition and ion-assisted deposition.

4.7 Sample Specifications

To be able to characterize the electronic properties of these materials without poly-silicon or other material gate contacts is highly desired by the industry. To measure their wafers' electrical properties, International Sematech, Austin, TX, has provided us with a batch of 200mm diameter $Si_{1-x}Ge_x$ wafers of 10-15% (x) varying Ge dopant (See Figure 4.3a). These samples were formed on p-type (B doping~$10^{16}cm^{-3}$) substrates to which a control sample of just the p-type substrate with an epitaxially grown Si layer on top was also supplied. In addition, they have also supplied us with two batches of HfO_2 and SiO_2 dielectric on p-type 200mm diameter silicon wafers (see Figures 4.3b, c). The first batch was a set of 200mm diameter wafers with differing thickness of 50, 75, 100 angstrom thick layers of SiO_2 or HfO_2 deposited on a p+ layer (B doping~$10^{18}cm^{-3}$) which is on top of a p-type silicon substrate; a control sample with no oxide was also provided. The second batch was a set of 200mm diameter wafers with either a photoresist (PR) or nitride deposition-Si_3N_4 (ND) coating on 70 or 100 angstrom thick HfO_2 and 50 angstrom thick SiO_2 dielectric layers. Again all samples were deposited on a heavily doped p+ layer on top of a p-type Si substrate, but in this case two control samples were provided where each was coated with either photoresist or nitride deposition without any oxide underneath. The purpose of the photoresist or nitride deposition was to serve as a protecting layer to eliminate any interfacial SiO_2 layer that can form by oxygen-diffusion underneath the high-κ material after processing.

4.8 Types of Experiments

Reflection THz-TDS, Transmission THZ-TDS and Visible Pump/THz Probe experiments were performed to determine the optoelectric characteristics of the $Si_{1-x}Ge_x$, HfO_2, and SiO_2 bearing wafers given to us by Sematech International. The $Si_{1-x}Ge_x$ wafers and first batch of dielectric coated wafers were not transmitting through the THz pulse, possibly due to polishing treatments done on the backside of the wafers. These sets of wafers could only be examined under the Reflection THz-TDS set-up. In this case, the wafer is placed in our standard THz-TDS set-up at 45° to the THz beam, which reflects off the surface unfocused, at a spot size of ~43 mm (see Chapter 2, Figure 2.7c). The second batch of dielectric coated wafers, with photoresist (PR) or nitride deposition (ND), to our satisfaction, was able to transmit though the THz radiation. Here, the wafer is placed ~~vertical and~~ perpendicular to the THz beam which is focused with the aid of an off-axis parabolic mirror to a spot size of ~3 mm (see Chapter 2, Figure 2.7a). Also, this allowed us to perform Visible Pump/THz Probe measurements in transmission with a continuous wave (CW) Argon-Ion laser operating at $\lambda = 514$nm with an average power of 450 mW/cm^2. In this case, the visible pump is not time resolved, so that we are not probing the carrier dynamics but the response of the photoexcited carriers to the THz E-Field. It is important to note that this experiment could not be performed on reflection due to inadequate excitation power density. The pump beam covered an area of about ~4 cm^2, larger than the THz spot size, but much smaller than the THz spot size for reflection measurements. This impeded us from measuring an observable difference in the THz E-Field upon reflection from the photoexcited sample due to the lower pump intensity over the larger area. In addition, we repeated the reflection experiment under photoexcitation

with a white light incoherent source with an all line (UV to near-IR) output at ~300 $\mu W/cm^2$ for which again no evidence for THz absorption by photoexcited carriers were seen.

4.9 Results

4.9.1 Reflection/Transmission

All reflection, transmission and CW pump/THz probe measurements were analyzed individually as well as averaged over a number of many data sets to see whether any observed difference between each wafer were real or was an artifact. In reflection or transmission measurements time-domain scans showed little or no difference between each wafer. Upon transforming the data to the frequency domain trends were revealed for the $Si_{1-x}Ge_x$ sets of samples (Figure 4.4) and none for the oxides as can be seen in reflection (non-coated wafers, Figure 4.5; PR and ND coated ones Figure 4.6a) or transmission (PR or ND coated wafers, Figure 4.6b,c,d).

Here, the reflection and transmission curves are obtained by normalizing the data taken with the sample to data taken without the sample (negative). In the case of reflection, the negative sample was a gold mirror whose front surface was placed as to match the front surface of the sample. Since the front surface of the wafer did not exactly match the front surface of the gold mirror, there was a decrease in the observed intensity of about 20%, which we estimated from the reflection/transmission measurements we performed on a p-type silicon wafer (Figure 4.1, 4.2). Trends appeared for the $Si_{1-x}Ge_x$ scans (see Figure 4.9a). In particular, reflection off the control sample is always less than reflection off the 10 or 15% doped $Si_{1-x}Ge_x$ samples. Furthermore, the 10% doped sample

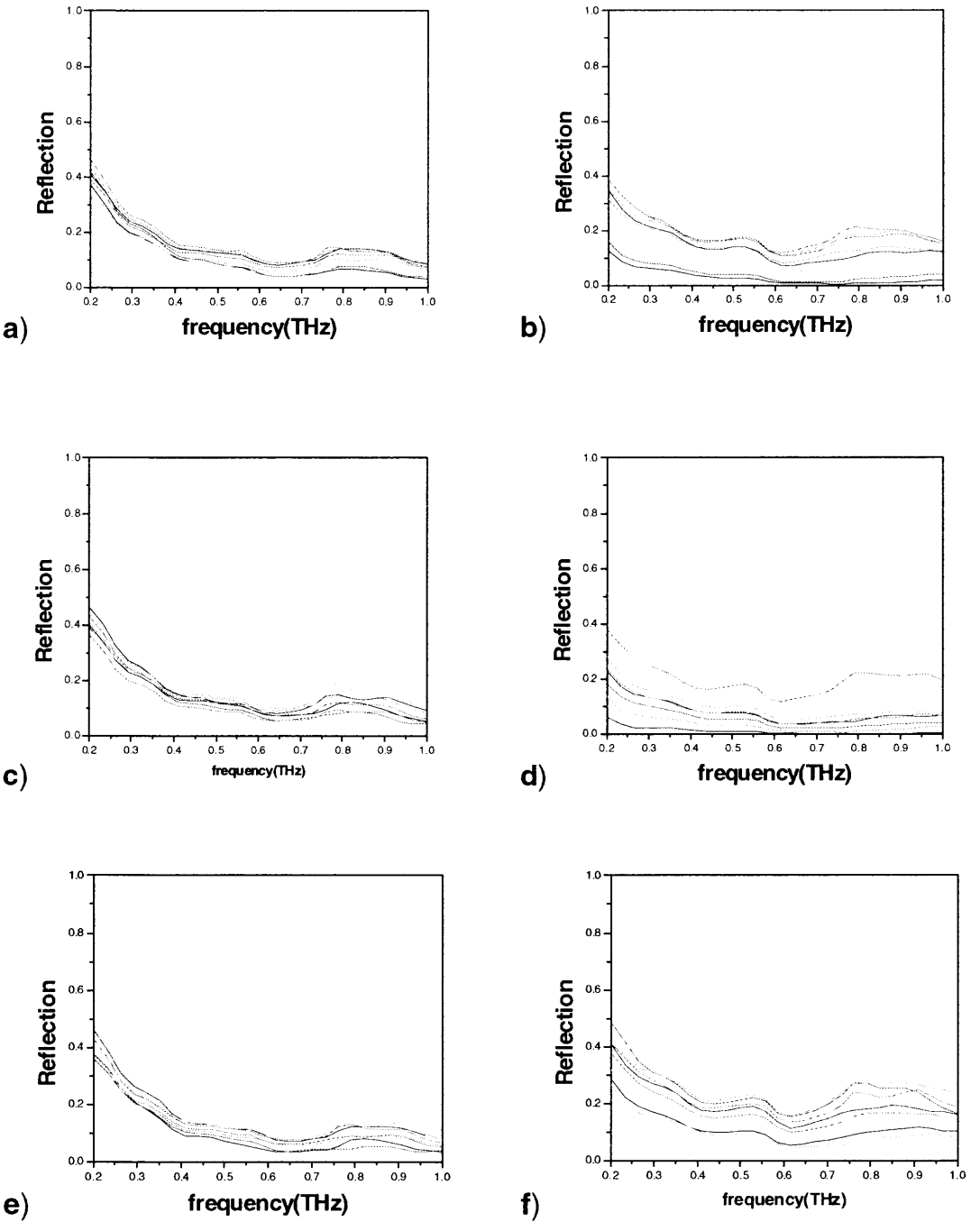

Figure 4.4. Reflection off of $Si_{1-x}Ge_x$. Figures in a, c, e represent scans from no Ge dopant to 10 and 15% Ge dopant which have been normalized to reflection off the gold mirror for which the front surface of the wafers and gold mirror were brought as close as possible (as close as thickness of wafer ~ 0.5-1mm) and the incidence angle of THz beam was rigidly kept at 45° for both wafer and mirror. Figures in b, d, and f are corresponding scans which does not follow the aforementioned criteria. Bumps at 0.58 THz and 0.78 THz are due to ambient water absorption.

is less transmittive than the 15% doped sample. This slight difference is a testament to the sensitivity of the THz-TDS technique, even though our S:N is roughly 200:1. The bumps in the scans are due to water absorption at 0.58 and 0.78 THz. All our scans include reflections off each interface except for the reflection off the backside of the wafer,

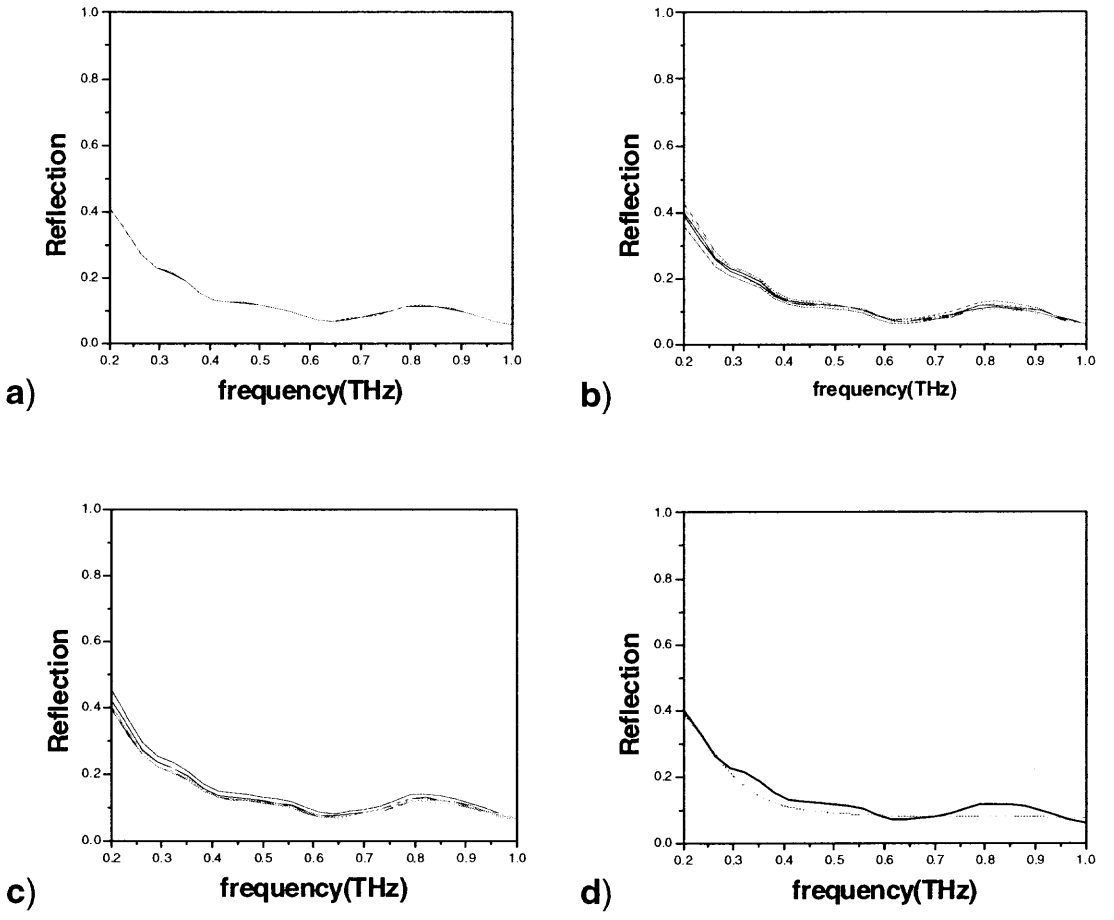

Figure 4.5. THz-TDS Reflection off 1st batch of dielectric deposited wafers. a) Control: p-type Si substrate, b) 50, 75, 100 A thick SiO_2 on p-type Si substrate, c) 50, 75, 100 A thick HfO_2 on p-type Si substrate, d) Average of all scans (solid curve) and fit (dashed curve) with parameters $N_p = 1x10^{16}cm^{-3}$ and $\tau = 0.3x10^{-12}s$. Assuming the thin-dielectric limit as outlined in the text, as well as assuming $m_{eff}^* = .38m_e$.

this limited us to a maximum of 0.025 THz resolution for reflection and ~0.04 THz resolution for transmission measurements. The transmission through the protected oxides,

although nearly indistinguishable, revealed larger uncertainty at higher frequencies (Figure 4.6b, c, d). We believe this is due to the small spot size of the THz beam (~3 mm) which is sensing a smaller area than reflection scans thus we are probably more susceptible to surface and subsurface distortions in the sample.

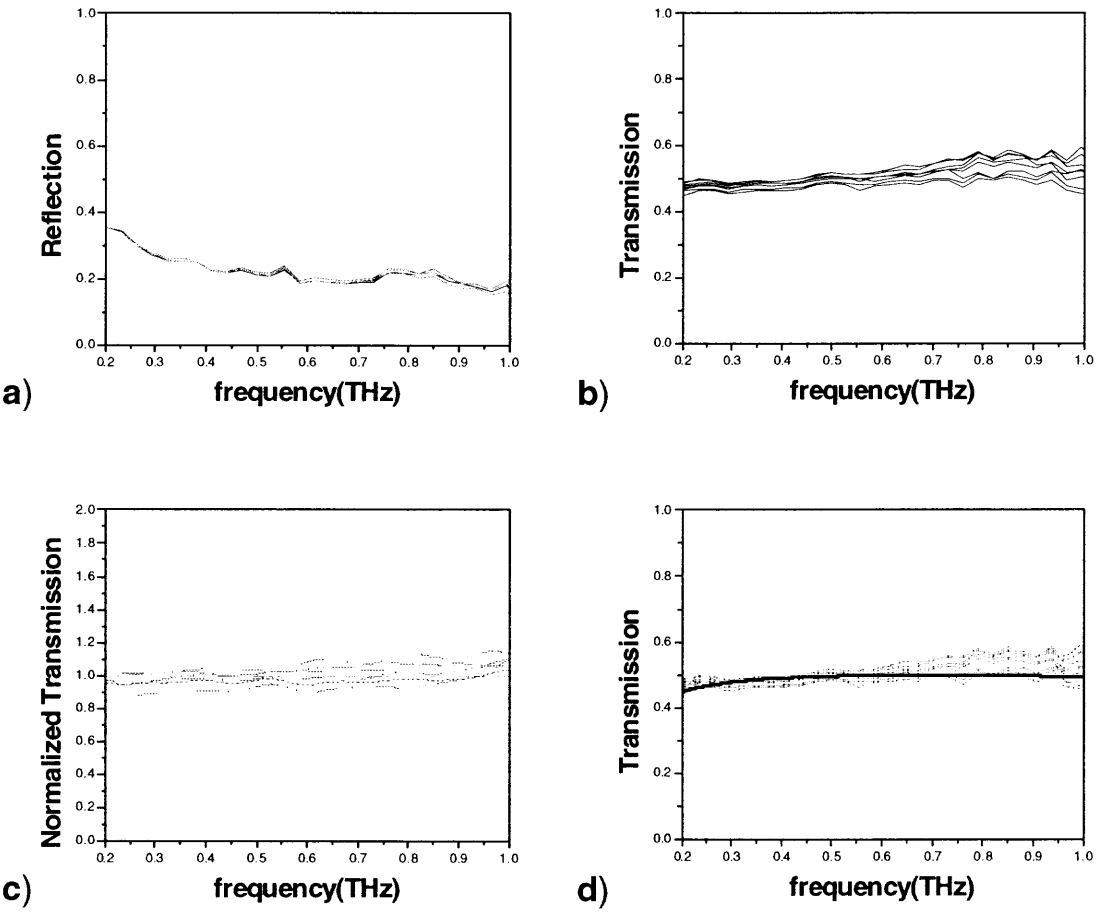

Figure 4.6. Reflection and Transmission of 2nd batch of dielectric deposited wafers with protective photoresist or nitride deposition coating on top. The layers underneath the oxide are p+ Si on p-type Si substrate. a) Reflection off Control (Photoresist and Nitride Deposition), 50 A SiO_2 (PR and ND), 70 and 100 HfO_2 (PR and ND); b) Transmission through Control (Photoresist and Nitride Deposition), 50 A SiO_2 (PR and ND), 70 and 100 HfO_2 (PR and ND); c) Transmission normalized to Control showing relative deviation of all plots from 1; d) Transmission fit with Drude model (solid curve) with parameters $N_p = 1x10^{18}cm^{-3}$ and $\tau = 0.02x10^{-12}$ s for p+ layer and $N_p = 1x10^{16}cm^{-3}$ and $\tau = 0.14x10^{-12}$ s for p-type substrate, and $m_{eff}^* = .38m_e$ for all wafer samples.

4.9.2 CW Visible Pump/THz Probe

Although the HfO_2 and SiO_2 were much alike in respect to reflection and transmission measurements, they were very much different under a visible pump. The THz transmission was considerably attenuated when the samples were photoexcited with CW

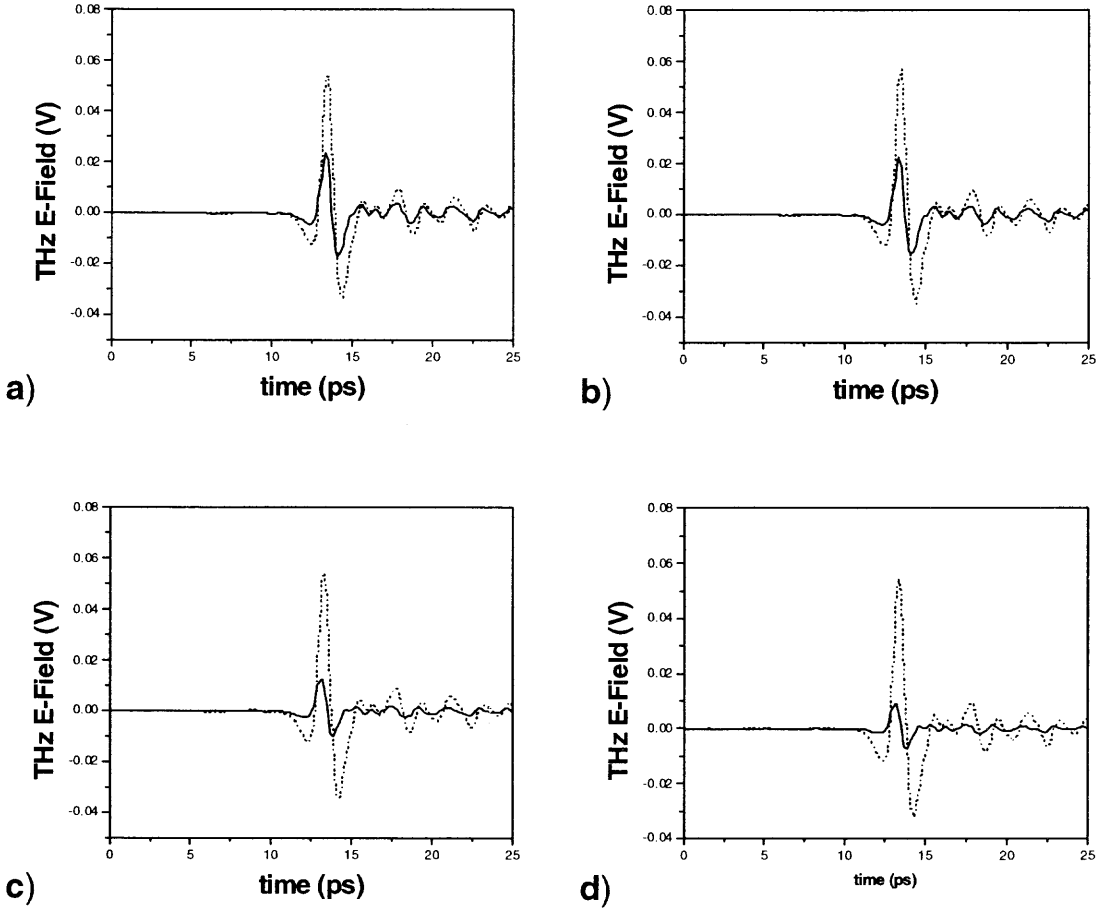

Figure 4.7.1. Time-domain pump on (solid curve) and pump off (dashed curve) scans through PR and ND coated SiO_2, HfO_2 and Control wafers. a) SiO_2, PR; b) SiO_2, ND; c) HfO_2, PR; d) HfO_2, ND. These figures show that the most dominant effect is a change in amplitude of the THz waveform and that phase change is negligible (however relative delay more pronounced for HfO_2 rather than SiO_2 and Control). The pump was an all lines visible CW Ar+-Ion laser at 450mW/cm^2 on the sample surface.

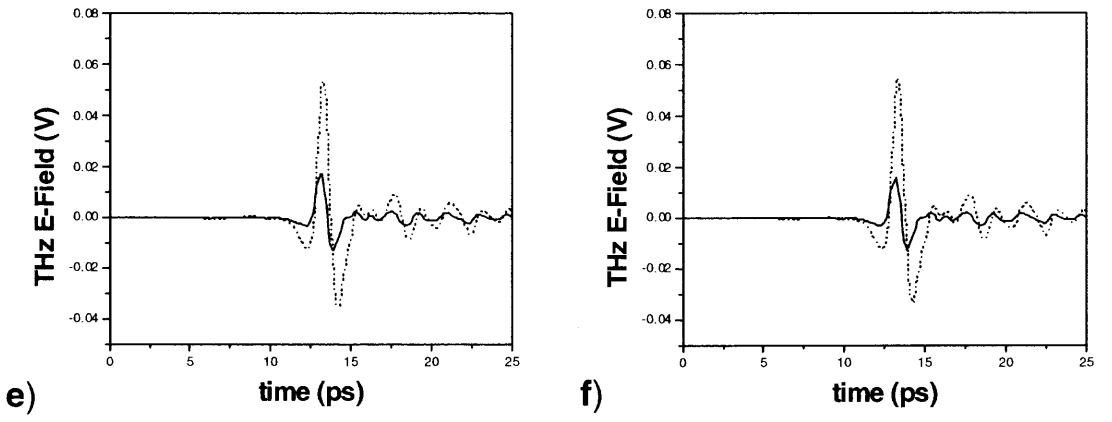

Figure 4.7.2. Time-domain pump on (solid curve) and pump off (dashed curve) scans through Control wafers. e) Control, PR; f) Control, ND. Refer to Figure 4.7.1.

Ar+-Ion beam. The differences were evident in the time-domain (see Figure 4.7) as well as the frequency domain data sets (Figure 4.8). The data shown in Figure 4.8 show the change in transmission (pump on-pump off) normalized to transmission under no pumping.

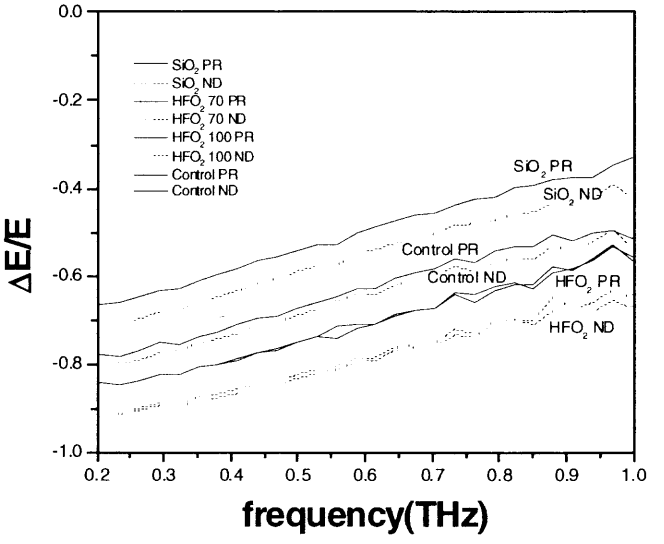

Figure 4.8. ΔE/E for 2nd set of dielectric coated wafers under a visible pump power of 450mW/cm^2 from a CW Ar+-Ion laser. Clear differences emerge between HfO_2, SiO_2 and Control samples using all optical non-contact methods.

4.10 Analysis of Reflection/Transmission (No Visible Excitation)

4.10.1 Drude Model

The free carrier dispersion model (Drude model) has been used successfully to characterize the frequency dependent parameters of semiconductors of various types [27,103,107]. In the free carrier Drude Model, the frequency dependent dielectric constant of the material is modeled as:

$$\tilde{n}^2 = (n+ik)^2 = \varepsilon(\omega) = \varepsilon_\infty - \frac{\omega_p^{\,2}}{\omega\left(\omega + i\frac{1}{\tau}\right)} \tag{4.2}$$

where, n is the real and k is the imaginary part of the complex index of refraction, ε_∞ is the dielectric constant of the material at high frequencies, $1/\tau$ is the collision frequency, $\omega_p=(4\pi Ne^2/m_{eff})^{1/2}$, N, e, m_{eff} are the plasma frequency, number density, charge and effective mass of the free carriers (electrons or holes), respectively.

4.10.2 Multilayer Reflection/Transmission Analysis

Through a Kramers-Kronig based analysis to obtain the reflection and transmission coefficients for the layered semiconductor structure, we can fit the reflection, transmission and visible-pump/THz probe data sets in order to estimate the frequency dependent dielectric constant, $\varepsilon(\omega)$ for each layer. The reflection off an interface between two dispersive media with complex index of refraction n_{n+1} and n_n is given by:

$$R_{n,n+1} = \left|\frac{n_{n+1} - n_n}{n_{n+1} + n_n}\right|^2 \tag{4.3}$$

For the measurements done under no excitation, we used the structure as shown in Figure 4.3. As can be seen there, there are multiple layers that need to be considered. The

reflection through $Si_{1-x}Ge_x$ and SiO_2 and HfO_2 can be modeled with the following expression, for n', n ∈ 0,1,2,...etc. and n' > n:

$$R_{n,\ldots,n'} = \frac{R_{n,n+1} + R_{n+1,n+2}e^{i2\beta_{n+1}}}{1 + R_{n,n+1}R_{n+1,n+2}e^{i2\beta_{n+1}}} \tag{4.4}$$

where, $\beta_{n+1} = \frac{2\pi}{\lambda_o} n_{n+1} d_{n+1} \cos\vartheta_{n+1}$, where θ is the angle of incidence (in our case 45°) and the expression can be extended to more layers by recursively defining $R_{n+1,n+2}$ to $R_{n'-1,n'}$. The above expression can also be obtained from matrix method of analyzing the reflection and transmission coefficient between each interface. For transmission at normal incidence through n' layers, n_o being the first medium (in our case n_o = 1, air):

$$T = \left| \frac{2n_0}{M_{11}n_0 + M_{12}n_0 n' + M_{21}n_0 + M_{22}n_0 n'} \right|^2 \tag{4.5a}$$

where,

$$M_{ij} = \begin{pmatrix} M_{11} & M_{12} \\ M_{21} & M_{22} \end{pmatrix}, and, M_{ij} = M_{n+1}M_{n+2}\ldots M_{n'} \tag{4.5b}$$

and,

$$M_n = \begin{pmatrix} \cos\delta_n & \frac{i}{n_n}\sin\delta_n \\ in_n \sin\delta_n & \cos\delta_n \end{pmatrix} \tag{4.5c}$$

where, $\delta_n = n_n k_o d_n$. Reflections from the backside of the substrate were not considered. We assumed literature values for the frequency independent dielectric constants for Si, the photoresist and silicon nitride (see Table 4.1). Since the HfO_2 is a high-κ material one would expect that the reflection or transmission would be considerable different than the SiO_2, however, the index of refraction in the FIR is on the order of 2.1, close to SiO_2.

Table 4.1: Optical Properties of Various Materials.

	Si	$Si_{1-x}Ge_x$	SiO_2	HfO_2	*Photoresist (PR)*	Si_3N_4 *(ND)*
Index of refraction (n)	3.42[a]	$3.42 + 0.37x + 0.22x^2$ [e]	1.5[a]	2.1[g]	1.4[i]	2.1[a]
Absorption coefficient (α, cm^{-1})	P-doped ~1-2x10^4 [b] for UV-Vis. 2.06x10^{-16} cm^{-2}xN for 0.1 THz[c]	-	Negligible	$2\pi x10^5$ [h]	Depends on photoresist ~11	Negligible-extinction coefficient(~ 2x10^{-4})
Effective Mass (m_{eff}^*/m_e)	0.26 for electrons[d], 0.38 for holes[d]	0.44 for holes[f]	-	-	-	-

[a] "The General Properties of Si, Ge, SiGe, SiO_2 and Si_3N_4." Site details properties of compound semiconductors and dielectric films. Retrieved October 1, 2004, from http://www.viriginiasemi.com/pdf/generalproperties20Si62002.DOC.

[b] Jellison Jr., G.R., Modina, F.A., White, C.W., Wood, R.F., and Young, R.T., "Optical Properties of heavily doped silicon between 1.5 and 4.1eV," Phys Rev. Lett. 46(21), 1414 (1981)

[c] Perera, A.G.U., Shen, W.Z., Mallard, W.C., Tanner, M.O., and Wang, K.L., "Far-infrared free hole absorption in epitaxial silicon films for homojunction detectors," Appl. Phys. Lett. 71(4), 515 (1997)

[d] Van Zeghbroeck, B., "Principles of Semiconductor Devices." Site details properties of semiconductor devices in a book format. Retrieved October 1, 2004 from http://ece-www.colorado.edu/~bart/book/

[e] National Compound Semiconductor Roadmap (NCSR)-SiGe, Site details properties of SiGe. Retrieved October 1, 2004, from http://www.onr.navy.mil/sci_tech/information/312_electronics/ncsr/materials/sige.asp

[f] Swain, P.K., Madapar, S., and Misra, D., "Plasma process-induced band-gap modifications of a strained SiGe heterostructure," Appl. Phys. Lett. 74(21), 3173 (1999)

[g] Lee, J.C., "High-k Gate dielectrics ZrO & HfO. Are they reliable?" Site gives presentation on high-k dielectric films. Retrieved October 1, 2004, from http://www.sematech.org/meetings/20001030/04_Gate_Stack_Transistor_Lee.pdf

[h] Zukic, M., Torr, D.G., Span, J.F., and Torr, M.R., "Vacuum Ultraviolet Thin Films. 1: Optical Constants of HaFBaF2, CaF2, LaF3, MgF2, Al2O3, HfO2 and SiO2 thin films," Appl. Opt. 29(28), 4284 (1990)

[i] Semiconductor International, Reed Electronics Group. Site details properties of deep-UV photoresist. Retrieved October 1, 2004 from http://www.reed-electronics.com/semiconductor/article/CA415043?pubdate=5%2F1%2F2004&spacedesc=webex

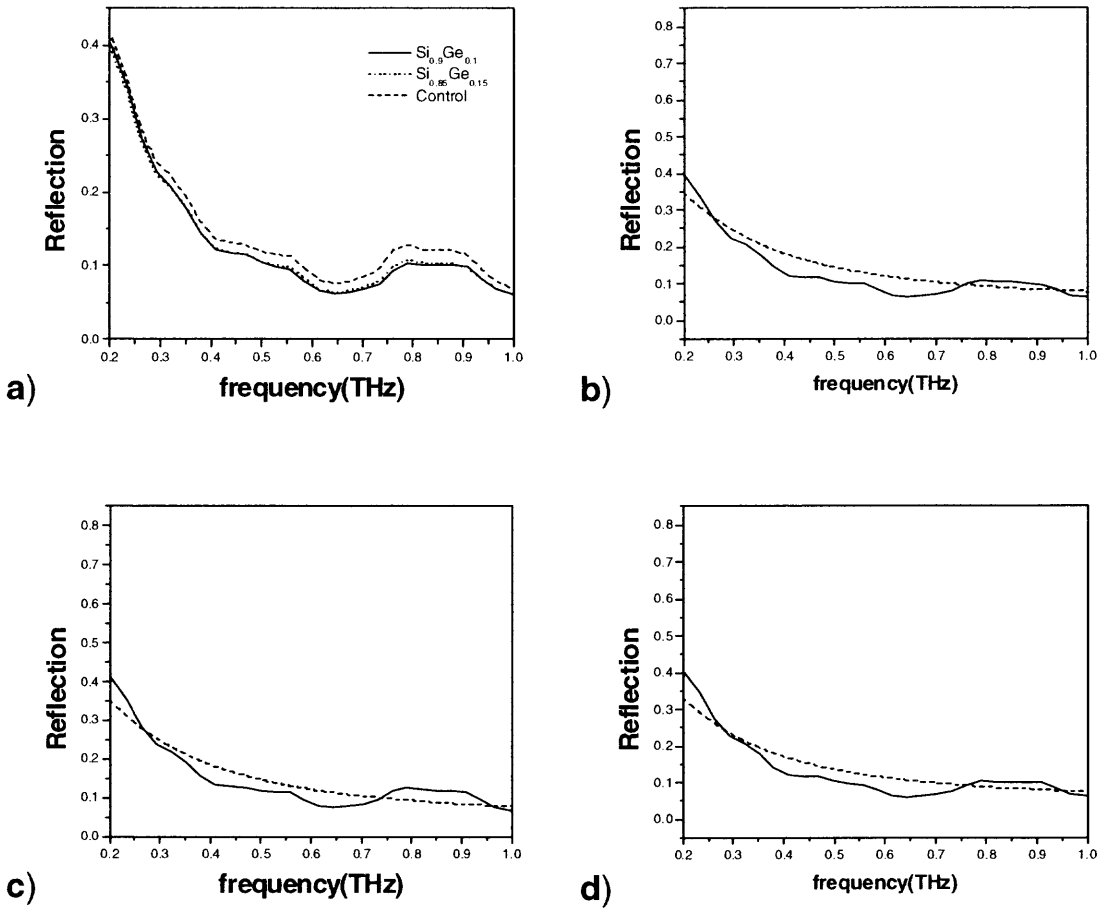

Figure 4.9. Averaged Reflection scans though $Si_{1-x}Ge_x$ and fits. a) Avg. scans for Control (lower dashed curve), $Si_{0.9}Ge_{0.1}$ (lower solid curve), $Si_{0.85}Ge_{0.15}$ (upper dashed curve). Fits (dashed curves) for b) $Si_{0.9}Ge_{0.1}$, c) $Si_{0.85}Ge_{0.15}$, and d) Control. Drude parameters for curves were $N_p = 4x10^{16}cm^{-3}$ for b,c,d and $\tau = 0.10x10^{-12}s$ for b, $\tau = 0.12x10^{-12}s$ for c, and $\tau = 0.10x10^{-12}s$ for d, assuming $m_{eff}^* = .44m_e$.

4.10.3 Effective Dielectric Function of $Si_{1-x}Ge_x$

To approximate the frequency-independent index of refraction for the SiGe composite a number of approaches can be taken. Since we know the concentration of Ge (x = 0.1 or 0.15 of total) we can estimate the resulting index of refraction from band structure calculations [117]. As previously done with the nanocomposites we can not approximate it with a Garnett approach [**Error! Bookmark not defined.**] assuming that

Si is the dielectric and Ge is the embedded metallic material since this assumes that the host and the resulting composite is non-conducting. Using the approach based on band structure, the index of refraction for the $Si_{1-x}Ge_x$ alloy can be estimated as [118]:

$$n(Si_{1-x}Ge_x) = 3.42 + 0.37x^2 + 0.22x^2 \tag{4.6}$$

for x < 0.85. For us, x can be either 0.1 or 0.15 depending on the Ge concentration of the alloy. However, this model assumes that the resulting index of refraction is frequency independent. We can model the composite $n(\omega)$ by assuming the Ge (individual atoms) is intermixed with the crystalline silicon in a Bruggeman type effective medium. The Bruggeman Effective Medium Approximation (BEMA) is given by:

$$0 = (1-x)\varepsilon_{Si}\left(\frac{\varepsilon_{Si}-\varepsilon_{eff}}{\varepsilon_{Si}+2\varepsilon_{eff}}\right) + (x)\varepsilon_{Ge}\left(\frac{\varepsilon_{Ge}-\varepsilon_{eff}}{\varepsilon_{Ge}+2\varepsilon_{eff}}\right) \tag{4.7}$$

where, ε_{Si} and ε_{Ge} are the frequency-dependent dielectric constants of Si and Ge, respectively. This approach has been successfully implemented in determining the complex index for photonic crystals of Si in SiO_2 deposited on Si [119]. Here the SiO_2 is the amorphous medium, and the Si is crystalline.

The fits were generated using commercial software (Mathcad™) show a good agreement between the data and the model (see Figure 4.9). By just changing the Ge concentration we can account for the slight difference between the control sample as well as the 10 and 15% doped SiGe curves and obtain different values for the scattering times. The mobility in a p-type or n-type semiconductor is given by:

$$\mu_p = \frac{q\tau_p}{m_{eff}}, \mu_e = \frac{q\tau_e}{m_{eff}} \tag{4.8}$$

Where, q is the electron charge, τ is the scattering time and m_{eff} is the effective mass of holes or electrons. Assuming that holes dominate due to the p-type substrate, we estimate the hole mobility of the control sample on the order of 400, for 10% doped sample to be on the order of 400, and the 15% doped sample to be on the order of 460 $cm^2/V/s$. These estimates agree well with other known values for p-type silicon [118] heterostructures with SiGe layers.

4.10.4 Thin Dielectric Approximation to Reflection for Oxides

For the two batches of HfO_2, SiO_2 wafers, distinguished by one set having a protecting of either photoresist or nitride deposition, one might expect that the magnitude of reflection should be considerably much less than as observed with $Si_{1-x}Ge_x$ wafers due to the index mismatch between air and the medium. In contrast, the reflection was not only on the same magnitude but exhibited similar spectral features. This is due to the fact that at long wavelengths the reflection coefficient for dielectric coatings on metallic or semi-metallic substrates can be approximated as that of just the substrate ignoring the dielectric. This approximation stems from the thickness of the dielectric being much smaller than the THz wavelengths. The reflection coefficient given in equation 4.4 becomes [120]:

$$R_{1,\ldots,3} = R_{13} + i\beta_2(coupled\_terms) \tag{4.9}$$

The second term on the right goes as the thickness, and drops out for very thin layers. Since the thickness of the nitride deposition (~200 angstroms), photoresist (3000 angstroms), SiO_2 (50-100 angstroms), HfO_2 (50-100 angstroms), are all less than the wavelength (<300 μm), the reflection coefficient simplifies to a relationship between air and the substrate medium (p-type silicon)-similar to equation 4.3. Fits using this approximation are shown for both sets of dielectric coated wafers in Figures 4.5 and 4.6.

4.10.5 Discussion on Models with no Visible Excitation

For all samples, the majority carriers of the p-type substrate are holes; thereby the plasma frequency can be approximated using the doping concentration (~10^{16} cm^{-3}). This also explains why control sample in each respective batch gave the exact same magnitude and same spectral features as the oxides. With this approximation the data sets were modeled and similar values were obtained for the scattering time and mobility as was with the $Si_{1-x}Ge_x$ samples (Compare information given in Figures 4.5, 4.6, and 4.9).

Transmission through the 2nd set of dielectric coated wafers was analyzed using the same approximation as was done with reflection measurements (see section 4.10.4 and Figure 4.6d). However, in these samples, the substrate was doped highly (p+ layer at 10^{18} cm^{-3}, 10^{16} cm^{-3} underneath) at the surface (300 angstrom thick) so the plasma frequency changed as well. The higher doping was done purposefully by the manufacturer so that we could observe effects near the interface between oxide and substrate. There were no trends between differing oxides as had been observed for $Si_{1-x}Ge_x$ wafers. We conclude that since we can model the data without considering the dielectric, we are unable to determine the effect of the dielectric on the mobility, using either linear (unpumped) Reflection or Transmission measurements. Thus, this method is not very useful since it can not differ between the SiO_2 and HfO_2 coated wafers. However, the situation is quite different when the sample is photoexcited (see section 4.11).

Even though scattering by physical variations and absorption by phonons were not considered, the above analysis is able to fit $Si_{1-x}Ge_x$ data sets well. We estimate, through varying parameters that the maximum deviation of the fit from the data is on

average less than 20%, and that there is a 15-20% uncertainty with our estimates for the mobility. The deviation of the fit was estimated by the standard deviation of the averaged value data set. The variations in the data sets are most probably due to noise and water absorption. Within these estimates our results for the hole-mobility agree with other reported values of up to 600 $cm^2V^{-1}s^{-1}$ for similar Ge dopant [114, 118]. Once these errors are accounted (Nitrogen purging, and better stability of mode-locked laser) for we believe the THz-TDS technique will be a well-suited method to accurately predict the mobility of $Si_{1-x}Ge_x$.

4.11 Analysis of CW Visible Pump/THz Probe Measurements

4.11.1 Effect of HfO_2 on Mobility

Understanding the effects of the high-κ dielectric on the underlying substrate is of great interest to the semiconductor industry. Hall measurements made by the manufacturer on similar HfO_2 and SiO_2 coated p-type Si substrates using polysilicon gate contacts show that the channel mobility underneath the high-κ material was less than that of SiO_2. Others have also reported that the HfO_2 diminishes the mobility in the channel due to the presence of more interfacial defects between it and the Si substrate than with SiO_2 and Si (see Figure 4.10) [121].

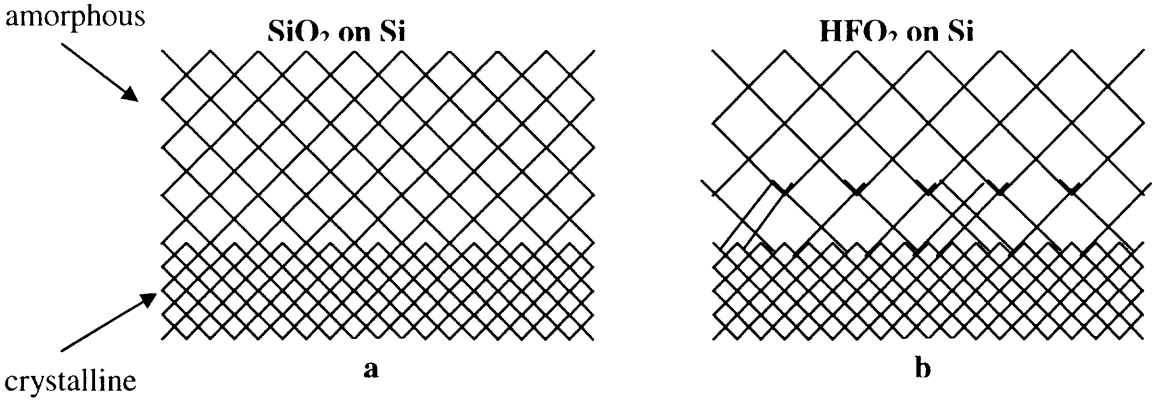

Figure 4.10. Representation of a) Near perfect lattice match of SiO_2 grown on silicon compared with b) interfacial defect as apparent with HfO_2 grown on silicon. The defects that arise in the interfacial layer, as well as trapped charges due to defects in the oxide, is what is believed to be the cause of the measured lower Hall mobility values as mentioned in the text.

4.11.2 Assessing the Photoexcited Layered Structure

The observable difference between SiO_2 and HfO_2 using visible pump/THz probe technique can be also analyzed with a Drude approach. Before we can analyze the pumped transmission we need to understand which layers the photoexcited carriers are confined to and what their relative density is. To estimate the latter we used literature values for the absorption coefficient of each layer-HfO_2, SiO_2, photoresist, Si_3N_4, p+ layer, p-type substrate (see Table 4.1), and deduced what percentage of the incident visible power fell on each layer. We also used literature values for the effective mass of the carriers (holes) in the p+ and p-type silicon layers (see Table 4.1). The layered structure under visible pump is shown in Figure 4.11.

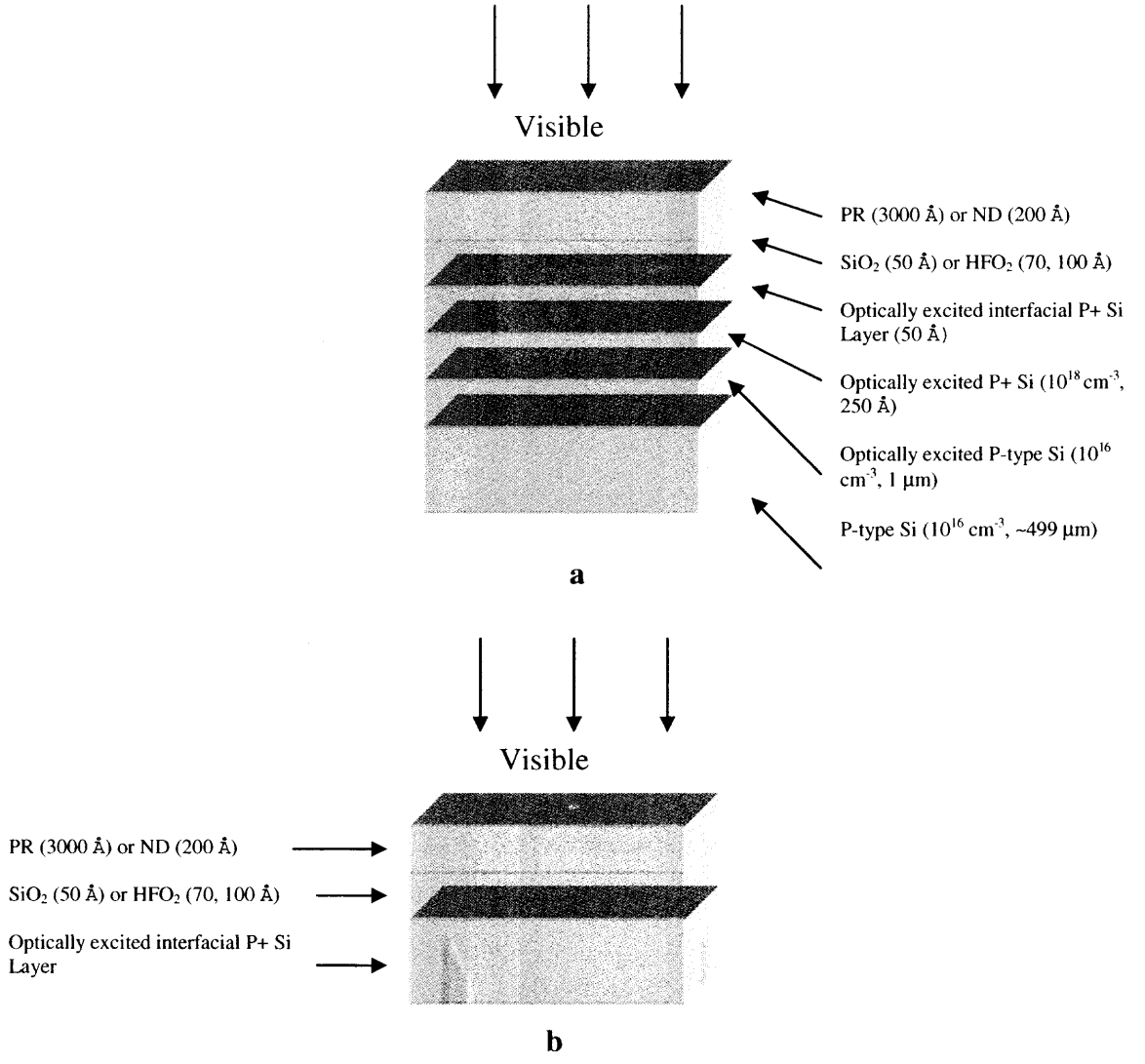

Figure 4.11. Two representations of the layered structure after visible excitation. a) A layer specific model which takes into account the varying absorption (cm^{-1}) through each layer of the visible beam and the effect on carrier concentration; b) simple layered structure which takes advantage of the fact that the pump beam is CW making our measurements insensitive to thin-layer specific effects and approximates the optically excited p+ and p-type layers as one layer.

4.11.3 Multilayered Structure Assuming an Interfacial Layer between Oxide and p+ Layer

Using the absorption coefficients as well as parameters obtained from the unpumped transmission analysis as described above (scattering time and carrier density) we can analyze the transmission under pumping with two different approaches.

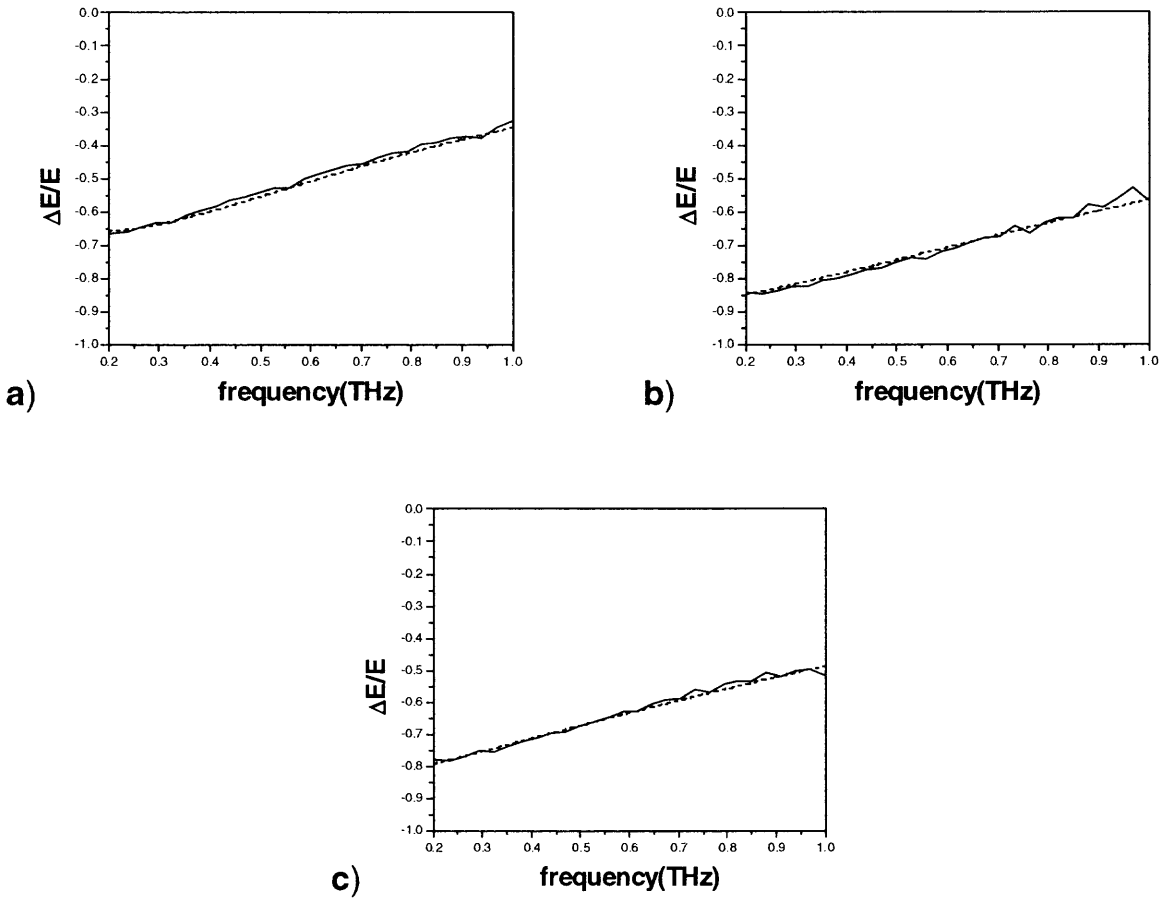

Figure 4.12. Fits to ΔE/E using the 1st multilayered model for a) 5.0nm thick SiO_2 coated with PR; b) 10.0nm thick HFO_2, coated with PR; c) Control, coated with PR. Parameters used in the fits are given in Table 4.2. The 7.0nm thick HfO_2 sample is almost identical in ΔE/E to 10.0nm thick HfO_2. Due to extremely large concentration of carriers needed to generate fits, this model seems insufficient. The larger effect (more negative) as observed with HfO_2 suggests that the mobility of HfO_2 coated wafer is higher than SiO_2 coated wafer under this model. This is contrary to previous Hall measurements

The first is similar to the way we analyzed the nanocomposites (see chapter 3). Assume that the photoexcited carriers change the effective dielectric constant by $\Delta\varepsilon$ and therefore change the index of refraction by Δn. However, to obtain $\varepsilon_{pump}(\omega)$ instead of calculating $\Delta\varepsilon$ due to pumping and adding it on $\varepsilon(\omega)$ (unpumped) we assume directly that

the carrier density and scattering rate change by an incremental amount ΔN and $\Delta\tau$ giving us $\varepsilon_{pump}(\omega)$:

$$\varepsilon_{pump}(\omega) = \varepsilon_{\infty} - \frac{\left[\frac{4\pi N' e^2}{m^*_{eff}}\right]}{\omega(\omega + i/\tau')} \tag{4.11}$$

Where, $N' = N + \Delta N$ and $\tau' = \tau + \Delta\tau$. ΔN and $\Delta\tau$ are the incremental changes due to photoexcitation. Using the modified index of refraction we can continue to calculate the transmission coefficient (see equation 4.5a-c) and obtain the scattering time in the photoexcited p+ layer (Figure 4.11a) which will give us an estimate for the mobility.

The results for this model are shown in Figure 4.12 for the PR coated samples only. We omit showing the 70angstrom thick HfO_2 sample since it is indifferent from the 100angstrom thick HfO_2. We also don't show fits for the ND samples, but we note that they are similar to the PR coated ones if we assume that the PR coating absorbs the incident visible excitation 5-25% more so than the ND coated sample (this is contrary to the literature values we quoted for α in Table 4.1). In addition we expect the control sample to give similar results to the SiO_2 sample since SiO_2 should not absorb any of the visible pump pulse. All the relevant values are shown in Table 4.2.

In analyzing these results, ideally, one would expect that the carrier density (N') in each sample is estimated with the only requirement that they reflect the relative intensity of light hitting the p+ layer after considering attenuation by each layer above with a non-zero absorption coefficient in the visible range. For example, this means that the carrier density in HfO_2 coated wafer should be less than the SiO_2 coated sample due to the fact the HfO_2 has a non-zero absorption coefficient in the visible range (see Table 4.1). However, the data could not be modeled with such an assumption. Contrary to this,

the carrier density in the HfO_2 sample had to be larger as can be seen in Table 4.2. One possible reason for this outcome is explained in detail later in sections 4.12-4.14. Here we give a brief summary: The carrier density in the sample does not only depend on the photoexcitation but also on the number of interfacial traps underneath the oxide. This allows for HfO_2 to have more effective number of carriers than SiO_2, even though SiO_2 is less absorptive, assuming that there are many more interfacial traps underneath HfO_2 then SiO_2. In addition, for the control sample, we believe there are more traps underneath the PR and ND coating then there is underneath SiO_2.

Considering the results for τ', the analysis shows that the mobility of the layer below HfO_2 is larger than that underneath SiO_2 by a factor of 2 or greater contrary to previous results [122] (see Table 4.2). The discrepancy only corrects itself, i.e. the mobility of the layer underneath HfO_2 is less than the mobility underneath SiO_2, if we assume that the carrier density in the interfacial layer underneath HfO_2 sample is at least a factor of 100 (instead of 10^{20} it should be $10^{22}cm^{-3}$) greater than the carrier density underneath the SiO_2 layer. This assumption allowed us to estimate the mobility of the HfO_2 to be at least half that of SiO_2. Such large carrier concentrations are improbable due to the low power of our photoexcitation source. While it is true that the generation of carriers is at a rate comparable to $10^{22}cm^{-3}s^{-1}$, recombination effects as well as diffusive effects will reduce the effective number of free carriers that the THz probe sees.

In summary, the fact that this model suggests that the mobility for HfO_2 is higher than SiO_2, plus, the fact that the carrier density is orders of magnitude off from realistic values is concerning. In all, this model is insufficient even though it makes an effort to approximate the physical properties of the structure as best as possible.

Table 4.2. Parameters Extracted from ΔE/E for the Interfacial Layer for 2nd Batch of Dielectric on Silicon Wafers.

	$N'(cm^{-3})$	$\tau'(s)$
SiO2 (PR)	$3.0x10^{20}$	$0.48x10^{-12}$
SiO2 (ND)	$3.3x10^{20}$	$0.48x10^{-12}$
HFO2 (PR)	$4.0x10^{20}$	$1.0x10^{-12}$
HFO2 (ND)	$5.5x10^{20}$	$1.0x10^{-12}$
Control (PR)	$3.8x10^{20}$	$0.55\ x10^{-12}$
Control (ND)	$4.0x10^{20}$	$0.55x10^{-12}$

4.11.4 Multilayered Structure Assuming the Underlying Layer beneath Oxide is Continuous.

Different from the above, the second model is to assume that the layer underneath the oxide is one continuous layer (as shown in Figure 4.11b), justified by two possible reasons:

- The photoexcitation is CW thus we may be sensing all the underlying layers since the absorption coefficients suggest that we penetrate all the way into the p-type substrate.
- The underlying layer is so heavily doped on the surface that the effect we observe is dominated to the layer for which the electron-hole pair (ehp) concentration is a maximum. This would be the p+ layer.

Of these two reasons the second is more plausible since the data suggests that the HfO_2, control and SiO_2 samples all show drastically different differential transmission ruling out that we are sensing a "deep" layer. If this were to be true than surface effects-

interfacial traps at the surface-due to HfO_2 would have to affect carriers deep into the substrate. There is no evidence in the literature for such an effect.

As shown in Figure 4.11b we estimate this underlying layer as a p+ layer and do not include reflections from the back surface, thus we make no assumptions on the layer thickness. We also further simplify our analysis by carefully examining the time-domain scans as shown in Figure 4.7. As can be seen the predominant effect is a reduction in the amplitude of the THz waveform when the sample is photodoped. Since we know, $\tilde{n} = n + ik$ and $\tilde{\varepsilon} = \varepsilon_r + i\varepsilon_i$ with $\varepsilon_i = 2nk$. And as shown in the time-domain scans there is relatively little or no phase delay, we can assume that the change in index of refraction due to pumping is due to the imaginary index only. Thus,

$$\tilde{n} + \Delta n = n + i(k + \Delta k) \tag{4.12}$$

where,

$$\Delta n = i\Delta k = i\frac{\Delta \varepsilon_i}{2n} \tag{4.13}$$

and,

$$\Delta \varepsilon_i = \frac{\left(4\pi \Delta N \frac{e}{m_{eff}}\right) \cdot \tau}{\omega[1 + (\omega\tau)^2]} \tag{4.14}$$

As can be seen in Figure 4.13 this model fits the data quite well. The parameters we obtained from the fits are quite striking (see Table 4.3). It is known that the creation of

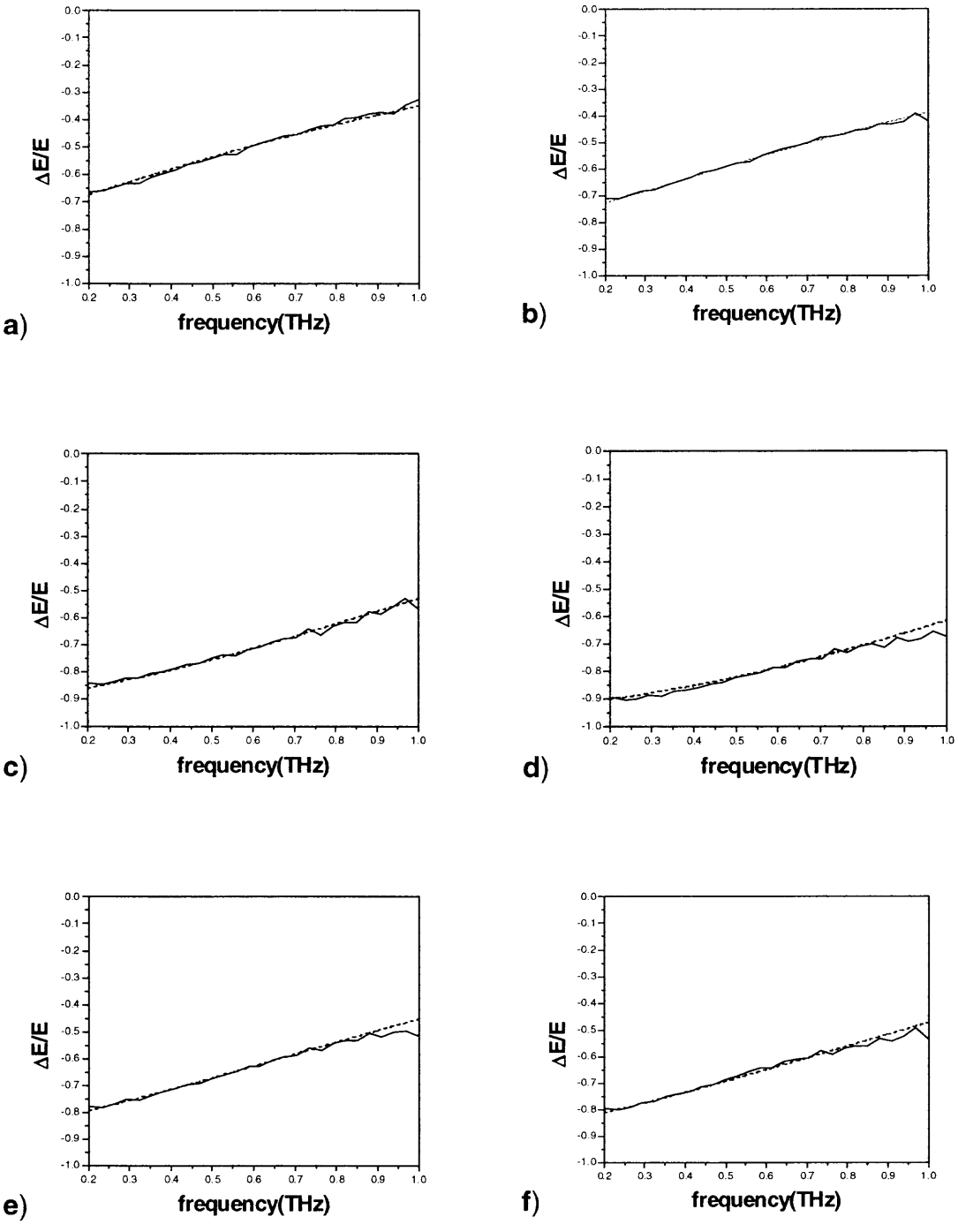

Figure 4.13. Fits to ΔE/E using the simple 2nd model where the entire layers underneath the oxide are approximated as one layer. a) 5.0nm thick SiO_2, PR; b) 5.0nm thick SiO_2, ND; c) 10.0nm thick HfO_2, PR; d) 10.0nm thick HfO_2, ND. Using the simple analysis as described in the text accurate fits were generated solely by changing the carrier concentration in the semiconductor layer underneath the oxide. These parameters are listed in Table 4.3.

ehp's increases the intrinsic mobility so the larger value for the scattering time than for previous unpumped measurement values is not unreasonable. In addition, we were able to fit all the samples by assuming the same scattering rate only changing the carrier densities.

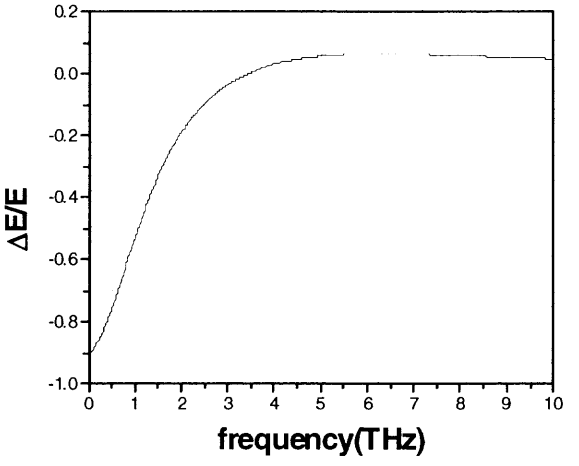

Figure 4.14. Fits using the second model extrapolated to higher frequencies for the 100 Å thick HfO_2 + photoresist coated wafer.

The additional carrier density due to pumping (ΔN) is less than the intrinsic density, which we assume as the doping concentration and is also less than that due to the relative photoexcitation striking the layer beneath the oxide. Thus, unlike the previous model, we do not need extraordinarily large carrier densities to fit the data (see Table 4.2). The ΔN for HfO_2 is larger than the ΔN of SiO_2 by a factor at least a factor of 6-10. We believe this increase is due to the many more interfacial traps associated with defects, which exist between the HfO_2 and the p+ layer more so than in the SiO_2/p+ Si interface, as has been suggested by others [121,122,123]. Since these interface-defect traps lie in a

state between the conduction and valence bands, carriers which are trapped in this state are re-excited into the conduction with the arrival of the next photon before they can recombine to the ground state [124] (see Figure 4.15).

The dynamical picture does not only dependent on the density of the trap states; it also depends on the fixed trapped charge in the oxide. Actually, the decrease in the mobility as observed with Hall measurements are primarily due to the fixed charge near the interface due to the oxide (Q_{ox}). After photoexcitation, defects in the oxide can be populated by carriers that may tunnel through to these available states being assisted by the visible excitation. This will affect the carriers in the interfacial states, and also the fixed charge (Q_{ox}). So any changes in the THz pulse will be dependent on the concentration of carriers (which will be dependent on the interfacial trap density and the effect of defects in the oxide) and the interfacial charge [125]. In the next section we try to estimate the density of trap states assuming non-radiative interfacial recombination to be the dominant effect explaining the difference between SiO_2 and HfO_2. Since we don't take Q_{ox} into account, our estimates are an upper limit to the trap densities.

In addition, the ΔN for Control is larger than that of SiO_2. This can be explained as follows: The Si_3N_4 deposition has been known to create interfacial traps [126], thus when placed directly on the p+ silicon it can lead to a poor interface. Our results suggest that the photoresist also provides a poorer interface than SiO_2/Si; however, there hasn't been any additional research in the scientific community on the effects of photoresist on Si mainly because it has no effect on device architecture or device performance.

Since we are pumping with a CW source we are continuously sending these trapped carriers back into the conduction band, thus, if there are more trapped carriers at

the interface we would see on average a larger carrier density. This is illustrated numerically in the next section where we can actually give an estimate on the number of interface traps (N_{IT}) due to the HfO_2 layer knowing the relative density due to the SiO_2 layer.

Table 4.3. Parameters Extracted from ΔE/E Fits of Figure 4.12.

	$\Delta N(cm^{-3})$	$\tau(s)$
SiO2 (PR)	$0.03x10^{18}$	$0.2x10^{-12}$
SiO2 (ND)	$0.08x10^{18}$	$0.2x10^{-12}$
HFO2 (PR)	$0.3x10^{18}$	$0.2x10^{-12}$
HFO2 (ND)	$0.48x10^{18}$	$0.2x10^{-12}$
Control (PR)	$0.17x10^{18}$	$0.2x10^{-12}$
Control (ND)	$0.20x10^{18}$	$0.2x10^{-12}$

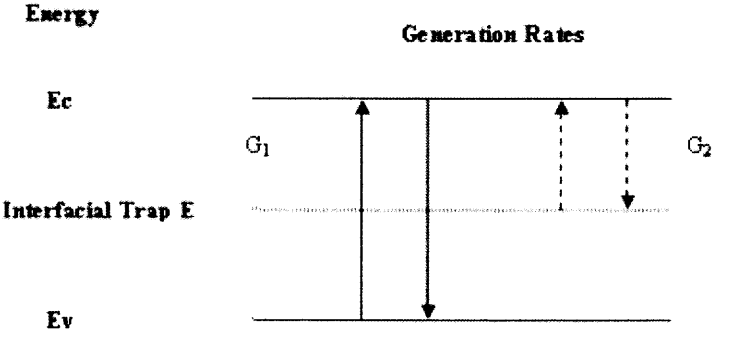

Figure 4.15. Energy band diagram representation of the carrier dynamics after photoexcitation. The carriers are sent into the conduction band from which they either recombine to the valence band (G_1) or an intermediary step due to interfacial traps between the oxide and the silicon surface. Where these traps become photo ionized and recombine continuously under a CW source (G_2).

4.12 Estimation of the Interfacial Defect Density

We can approximate the carrier generation rate of holes (p) or electrons (n) in a semiconductor due to a CW light-source as:

$$G_{p,pump} = G_{n,pump} = \frac{dP_{opt}(x)/dx}{E_{ph}A} = \frac{\alpha P_{opt}(x)}{E_{ph}A} \tag{4.15}$$

Where, $P_{opt}(x)/A$ is the visible power surface density (in our case 450 mW/cm^2), α is the power absorption coefficient, E_{ph} is the energy of the photon. In the simplest form, where we consider the generation from trap states and valence band, the carrier recombination/generation rate equation is given by:

$$\frac{dN_{n,p}}{dt} = \frac{-N_{eff}}{\tau_{eff}} + G_1 + G_2 \tag{4.16}$$

Where N_{eff} is the effective number of carriers which recombine back to the valence band plus the ones which recombine to the surface states and τ_{eff} is the effective recombination time of surface carriers as well as bulk carriers. Also, $G_1 = G_{pump}$ and $G_2 = \sigma_{h\upsilon}\Phi_{h\upsilon}N_{IT}$ [127], where N_{IT} is the surface interfacial trap density, σ_{hv} is the photon absorption cross section at the surface from interface traps and Φ_{hv} is the photon flux at the surface. G_2 represents the remittance of the carriers into the conduction band after absorbing a photon (photoionization of trap states). We ignore thermally excited carriers due to low pump power level. Note that, G_1 can be written in terms of the photon flux as $G_1 = G_{pump} = \alpha \cdot \Phi_{h\upsilon}$. The above relation is simplified since we don't consider any diffusive effects. As shown later, the above relation is further reduced to surface effects only. In the steady state:

$$0 = \frac{-N_{eff}}{\tau_{eff}} + G_1 + G_2 \tag{4.17}$$

where, τ_{eff} is the sum of the surface and bulk recombination rates:

$$\tau_{eff}^{-1} = \tau_s^{-1} + \tau_r^{-1} \rightarrow \tau_{eff} = \frac{\tau_s \tau_r}{\tau_s + \tau_r} \tag{4.18}$$

If we examine equation 4.17 closely, we can divide it into two processes: Photo ionization from trap states (G_2) and generation from valence band (G_1), so it would be better to write it as two rate equations:

$$0 = -R_1 - R_2 + G_1 = -R_1^{eff} + G_1 \tag{4.19a}$$

And,

$$0 = -R_1 - R_2 + G_2 = -R_2^{eff} + G_2 \tag{4.19b}$$

So that,

$$0 = -R_1^{eff} - R_2^{eff} + G_1 + G_2 \tag{4.19c}$$

Where, R_1 is the recombination back to the valence band and R_2 is the recombination rate back to the interfacial trap states. Then, from equation 4.17:

$$R_1^{eff} + R_2^{eff} = \frac{N_{eff}}{\tau_{eff}} \tag{4.19d}$$

We specifically examine equation 4.19d for two cases: HfO_2 and SiO_2 on p+ Si.. For ΔN (see equation 4.14), we assumed in our analysis that the layers underneath the oxide were continuous (so that we were effectively looking at surface effects). Also, the observed difference in $\Delta T/T$ between HfO_2 and SiO_2 is most probably due to surface effects, since they have the same layered structure underneath. Thus we assume that ΔN is mostly due to surface states or rather trap states and is related to R_2^{eff}. So that:

$$R_2^{eff} = \frac{\Delta N}{\tau_{eff}} \tag{4.20a}$$

And,

$$0 = \frac{-\Delta N}{\tau_{eff}} + G_2 \tag{4.20b}$$

since $\tau_s >> \tau_r$ [128] (recombination for trap states is much longer than bulk recombination), we can also assume $\tau_{eff} \sim \tau_r$ to be the same for both samples since they both have the same underlying layer, namely p+ silicon. Then, we can rewrite equation 4.20b as:

$$\sigma_{h\upsilon}(HfO_2)\Phi_{h\upsilon}N_{IT}(HfO_2) = \frac{\Delta N(HfO_2)}{\tau_r} \tag{4.21}$$

And,

$$\sigma_{h\upsilon}(SiO_2)\Phi_{h\upsilon}N_{IT}(SiO_2) = \frac{\Delta N(SiO_2)}{\tau_r} \tag{4.22}$$

since τ_r is the same for both SiO_2 and HfO_2 and N_{eff} is the same as the change in the number of carriers which we measured as ΔN (see equation 4.14), then:

$$\frac{\sigma_{h\upsilon}(HfO_2)\Phi_{h\upsilon}N_{IT}(HfO_2)}{\sigma_{h\upsilon}(SiO_2)\Phi_{h\upsilon}N_{IT}(SiO_2)} = \frac{\Delta N(HfO_2)}{\Delta N(SiO_2)} \tag{4.23}$$

Since, the ratio on the right of above equation is about 10 (see Table 4.3), we can obtain relationship between the interfacial trap density of SiO_2 and HfO_2.

$$N_{IT}(HfO_2) \approx 10\left(\frac{\sigma_{h\upsilon}(SiO_2)}{\sigma_{h\upsilon}(HfO_2)}\right)N_{IT}(SiO_2) \tag{4.24}$$

From previous electrical measurements, we can estimate the SiO_2/Si interfacial trap density to be on the order of $10^{10}cm^{-2}$ for low applied field strengths as was the case with our visible pump energy [122]. The term on the right hand side of equation 4.24 has a

dependence on σ_{hv}. For a photoexcited semiconductor, $\sigma_{h\upsilon} \approx \frac{\alpha}{\Delta N}$ where ΔN is the carrier concentration [129] due to photoexcitation. Thus by just assuming that the recombination time in the underlying layer between SiO_2 and HfO_2 is the same, and that the change in THz transmission (pump on-pump off) is due mostly to surface traps then we can estimate the interfacial trap density of HfO_2 to be at least 50-100 times greater than SiO_2 ($\sim 10^{12} cm^2$). Agreeing with electrical measurements (C-V measurements) on similar structured wafers where in these cases it was found that the interfacial trap density of HfO_2 was at most about a factor of 100 larger [122].

4.13 Discussion

THz-TDS in reflection, transmission and visible pump/THz probe configurations provide an effective mean towards understanding the optoelectric properties of semiconductor heterostructures. Ascertaining the mobility difference between a 10% and a 15% Ge dopant level in a $Si_{1-x}Ge_x$ alloy using an all optical method is very promising. We believe the sensitivity of THz-TDS upon reflection can be improved if we can focus the THz beam to spot size comparable to transmission measurements. This will also enable us to easily perform visible pump/THz probe upon reflection. Other groups report S:N on the order of 1000:1 using electro-optic THz generation/detection methods [35]. Coupled with experimental conditions that can account for water vapor, such as performing measurements in vacuum or under nitrogen purging, detection limits can be improved. We also incur error in our measurements from sample placement. The front surface of the wafer is not necessarily at the same position as the front surface of the gold mirror

(negative sample). The displacement of the beam will manifest itself as a loss in signal strength, which will affect the result.

Although the reflection/transmission measurements were almost identical for SiO_2, HfO_2 and the control samples the visible pump/THz probe measurements clearly show that the transmission through HfO_2 under pumping was far more reduced than the transmission through the SiO_2 or control. In addition the photoresist coated samples were always more transmittive than the Si_3N_4 coated samples. While the difference between SiO_2 and control can be attributed to the interfacial defects between photoresist or Si_3N_4 and the p+ layer, the difference observed between the photoresist (n=1.4) and Si_3N_4 (n=1.8) is not as clear. We think the photoresist is more absorptive to visible wavelengths than we had previously assumed (see Table 4.1). If we assume that α(photoresist) ~ 1000 x $\alpha(Si_3N_4)$, then we can account for its difference with Si_3N_4. Also from Figure 4.11 we can not see any difference between the 70ansgtrom HfO_2 or the 100angstrom HfO_2 wafers. This is expected since we are probing the carrier dynamics underneath these layers. In addition, their individual thickness difference does not affect the effect greatly the number of photoexcited carriers (70 angstrom layer less absorptive to visible photons than 100 angstrom layer). For the control samples, previous measurements suggest that the interfacial trap density for Si_3N_4/Si interface can be on the order of $10^{12}cm^{-3}$ prior to annealing [126]. Comparatively our measurements are in the same magnitude as this if we assume as before that the SiO_2/Si trap density is on the order of $10^{10}cm^{-3}$.

We expect that the optical mobility should be different than the electrical mobility [130], however the interfacial defects which are thought to cause the mobility measured by Hall Effect to be less for HfO_2 than SiO_2 should also apply for optical mobility as

well. Since, more interfacial traps would translate into shorter scattering time and a reduced optical mobility:

$$\tau \propto \frac{1}{N_T} \tag{4.25}$$

Where, N_T is number of traps. Since we can not infer the scattering time from our measurements (see Table 4.3), we can not infer the number of interface traps. To our benefit, in our analysis above, the scattering/recombination time drops out of the equation, this is why we are able to infer the number of interface traps purely from the added carriers in the conduction level (due to G_2).

From the above relation (equation 4.25), the scattering rate of the samples with HfO_2 should be 50-100 times less than that of the SiO_2 bearing wafers. This suggests that we need to consider both the real and imaginary part when calculating the change in index due to photoexcitation and not just the imaginary part as we had previously done. If we include the change in the scattering rate the effect on the fitting is minimal (see Figure 4.16), proving our initial assertion that we can ignore contributions from the real index.

A more thorough analysis would include effects of diffusivity of the carriers through each of the layers under the oxide. This would be formulated under the first model where we assume multiple layers underneath the oxide (See Table 4.2, Figure 4.10), and is not applicable to the second one as stated above since we are confining ourselves to surface effects. And to accurately analyze the effects of diffusivity one would need to probe the sample when the excitation is turned on and off, to see time-dependent effects.

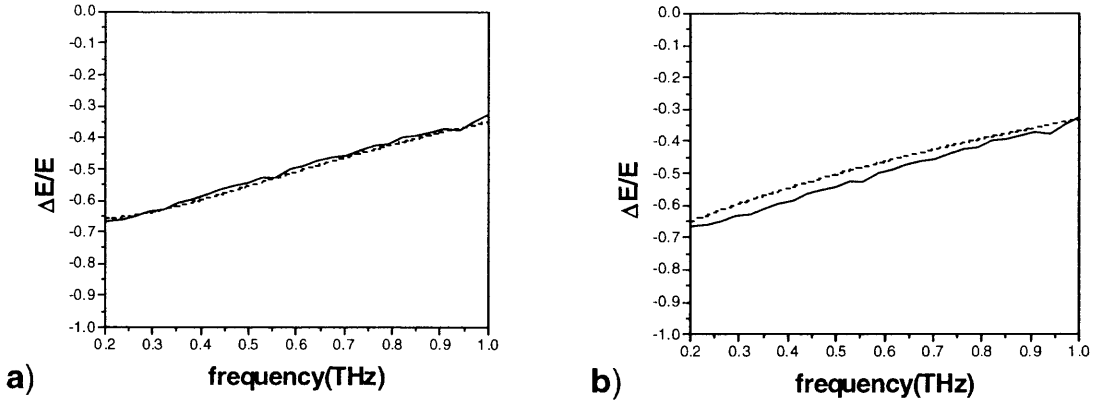

Figure 4.16. Differential transmission for SiO_2-PR coated sample. a) Assuming that change in index of refraction due to imaginary part only, where $\tau = 0.2x10^{-12}s$. b) Accounting for real as well as imaginary change in index with $\tau = .1x10^{-10}s$, corresponding to $N_T(HfO_2) \sim 50xN_T(SiO_2)$ (see equation 4.25).

4.14 Time Resolved Excitation

If we had to explain the observed effects in terms of the first multilayer model, we would be analyzing the carrier distribution after the system has reached some equilibrium carrier density in the sample. Then, the HfO_2 somehow effects this diffusive carrier distribution throughout the layers underneath the dielectric more so than SiO_2, explaining the larger carrier density needed in the underlying interfacial layer. Here we would also have to incorporate G_1 from equation 4.17 into the analysis to predict the trap density.

The other possible explanation could be that the defects introduced by HfO_2 not only effect the mobility but the absorptive properties of the p+ layer (300 angstroms thick), so that the carrier density in the underlying p-type substrate is much higher than that of SiO_2. For this to be true the absorption coefficient of the p-type substrate has to be ten times larger than that for the SiO2 sample over the penetration depth of the visible pump. To understand which of these effects is prevalent, we need to do time resolved

visible pump/THz probe measurements. In most semiconductors diffusion times are microseconds to milliseconds in duration, if we can probe the response of the layers after arrival of the ~100fs visible pulse then we can gauge the carrier density at the peak of the carrier generation. This generated carrier density will hopefully recombine much sooner than SiO_2 due to the number of defects under the HfO_2 allowing us to estimate the mobility. Whether this will allow us to measure the mobility accurately remains to be seen, but for the most part we are the first to see a measurable difference between HfO_2 and SiO_2 coated wafers and this research opens up the door to study other high-κ dielectric materials using THz-TDS techniques.

CHAPTER 5

CONCLUSION

5.1 Results

By applying a non-contact THz-TDS technique in transmission, reflection or visible pump/THz probe configurations we were able to effectively study the electronic characteristics of a variety of samples. In our work, as presented in this dissertation, we hope we have demonstrated its usefulness in analyzing nanocomposite materials as well as semiconductor heterostructure wafers. In the process we have discovered exciting new properties and results which previously, could not have been measured with other non-THz techniques.

5.1.1 Nanocomposites

We analyzed a host of nanocomposite materials. Most of the samples we tested were either grown or implanted on quartz or fused silica substrates which are transparent in the THz region.

Linear measurements (no photoexcitation) showed that for samples which had no metallicity, such as SWCNTs on quartz and ion implanted Si nanoclusters in fused silica, THz transmission from 0.2 to 1THz was fairly flat with no discerning features to suggest any absorption. Samples, whose predominant nature was metallic, such as carbon nanotube paper and MWCNTs deposited on quartz substrates, were completely opaque to the THz radiation. Reflection measurements could not be performed on these samples

since their size was much smaller than the THz beam diameter for our particular experimental scheme. The nanomaterial film thickness (few hundred nanometers) was much less than the THz wavelength for all the transmittive samples.

Non-linear measurements (done under photoexcitation) were performed to determine the nanomaterial characteristics after linear measurements were unsuccessful. For the first time, with the use of a visible pump-THz probe technique, the differential THz spectra of SWCNTs and ion implanted Si nanoclusters exhibited the existence of photo induced states. None of the other samples that we tested exhibited a similar response to the THz radiation under a visible excitation.

We modeled the observed differential transmission (visible pump on- visible pump off) using existing free-carrier and modified free-carrier conduction models. For SWCNTs and ion implanted Si nanocrystals a photo induced free-carrier Drude or Drude-Smith model was not consistent with the magnitude of the transmission coefficient. A better fit was obtained when incorporating Lorentz-like discreet states as outlined in the Drude + Lorentz model. The SWCNT data was consistent with a single Lorentz state in the measured frequency range at about 0.5THz, however we could not rule out the possibility that this state was the tail of a much broader state outside our frequency range. In addition since the density of nanotubes could not be verified to within the extracted fill-factor parameter of 5% in the Garnett model, the oscillator strength we extracted could have at most an order of magnitude difference. The flatness of the ion-implanted Si nanocluster differential spectra indicated either the presence of a broad Lorentz state in the 0.2-0.7THz range or, the presence of a much broader Lorentz peak outside of our spectral range.

Previous linear measurements on SWCNT mats whose thickness was on the order of microns showed evidence for localized states below 1THz [94]. However, no one has observed localized states in these structures for films whose thickness was on the order of hundreds of nanometers. We believe this is a testament to the sensitivity of the visible pump/THz probe technique.

5.1.2 Semiconductor Heterostructures

We performed measurements on 200mm diameter $Si_{1-x}Ge_x$ composite on p-type silicon wafers (B doping~$10^{16}cm^{-3}$) with a varying Ge content of 10% and 15%, as well as varying thickness of SiO_2 or high-κ dielectric (HfO_2) on 200mm p-type silicon wafers. Using THz-TDS upon reflection we were able to measure an observable difference between the 10% and 15% Ge content in $Si_{1-x}Ge_x$ samples. We measured the mobility of the 10% sample to be $400cm^2/V/s$ and the 15% sample to be $460cm^2/V/s$, agreeing within error to electrical measurements on similar samples [114]. None of these samples were transmittive, however, we note that the THz beam diameter was around ~43mm on the sample surface with an average power of a few microwatts. If we could focus the THz beam to a size comparable to that of transmission measurements (~3mm) we can improve the sensitivity of the technique by an order of magnitude.

We had two batches of dielectric coated wafers. While the first batch was not transmittive, the second batch was. Also, the second batch was coated with either a 3000 Å thick photoresist or 200 Å thick Si_3N_4 layer and the layer underneath the oxide was a 300 Å thick p+ (B doping~$10^{18}cm^{-3}$) on p-type substrate. The dielectric thickness varied between 50 and 100 Å on all samples. Reflection measurements were almost identical to samples with no dielectric on the surface. This was due to the much smaller thickness of

the dielectric layer compared to the THz radiation, so that upon reflection all samples exhibited the same response as the p-type silicon substrate. This was also true for transmission through the second batch of wafers.

Since the second batch was transmittive this allowed us to perform CW pump (Ar+-Ion laser)/THz probe measurements. Through these measurements we saw a difference between wafers that had a SiO_2 layer or an HfO_2 dielectric layer as well as wafers coated with photoresist or Si_3N_4. By analyzing two different transmission models through a stack layer configuration we concluded that the THz radiation under a visible pump is highly sensitive to the layer directly underneath the oxide so that interfacial effects as well as surface effects dominate the observed response. After extracting the appropriate free-carrier densities upon pumping through each wafer we analyzed the meaning of these carrier densities under a steady-state carrier recombination/generation rate equation model. Since we only considered the effects due to recombination process and not the oxide related fixed interfacial charge, we were only able to calculate an upper limit to the interfacial defect density in the HfO_2/p+ interfacial layer and found that it had 100 times more defects than the SiO_2/p+ layer, agreeing well with previous electrical measurements (C-V) [122]. In addition we calculate at most 50 times more defects between Si_3N_4/p+ and photoresist/p+ than in the SiO_2/p+ interfacial layers. Previous electrical measurements show similar results for Si_3N_4 [126].

5.2 Implications

SWCNTs are important for potential applications in development which include chemical sensors, probe tips, extremely lightweight and strong fabrics, and novel biological

detection methods. The presence of localized states under illumination could be exploited for detection methods. Most chemical and biological materials exhibit broad resonances between 0.1 and 1THz. A detector in this range based on SWCNT bundles that could be switched on and off by just shining visible light could be very useful in quantitatively determining the concentration of each species. As mentioned earlier, processes used to manufacture purely semiconducting CNTs yield a percentage of metallic tubes as well. The visible pump/THz probe method could determine and quantify the existence of semiconducting tubes in films whose thickness is on the order of hundreds nanometers.

It is of great interest to the semiconductor industry to develop a non-contact method to ascertain the properties of wafers they manufacture. $Si_{1-x}Ge_x$ based devices are finding many applications in electronics, especially high-speed devices which are essential for telecommunications. THz based methods can be successfully employed to determine wafer characteristics without the need for poly-silicon or metal electrode gate contacts for MOSFET development. As transistors decrease in size, the gate dielectric also scales down. We're at the limit that novel high-κ materials like HfO_2 need to be researched. Due to lattice mismatch none of the high-κ materials provide as good an interface as SiO_2. Defects between the gate oxide and the channel lead to a reduction in mobility. With visible pump/THz probe methods scientists can characterize the effect of interfacial defects without manufacturing the actual device, thus saving the manufacturer time and money.

5.3 Future Work

Visible pump/THz measurements need to be conducted on SWCNTs at higher visible pump powers so as to determine the effect on the observed photoinduced states below 1THz. By using either a ZnTe based THz generation/detection system or a photoconductive antenna based system with a bandwidth greater than 2THz, linear measurements can reveal the presence of photoinduced Lorentz-like states as was reported by others [71,94]. For samples that were not transmittive (metallic), reflection based visible pump/THz probe experiments can be performed to see whether photoinduced states exist for these samples as well. In addition the signal in time resolved experiments-to extract carrier lifetimes-can be improved by performing the experiments with a high power visible pump at 10μj-1mj/pulse. The hope is that we will see a difference in recombination lifetimes between SWCNTs in bundles and well separate ones.

Ideally, the results obtained for the semiconductor heterostructure wafers are promising enough that a commercial THz based wafer inspection system can be realized. This system will be nitrogen purged and the user will be able to perform for all three experimental configurations (reflection, transmission, CW pump/THz probe) with a degree of sensitivity described by the average THz flux on the sample. Currently, commercial THz systems are available, and with proper modifications could be converted and utilized by the semiconductor industry. In addition, time-resolved visible pump/THz probe experiments can reveal precisely the carrier dynamics underneath the oxide allowing us to analyze the recombination/generation rate equations exactly at the surface due to short time period of the excitation (~100fs) and probing pulses(~1ps). Then by

turning this excitation off (allowing only one visible pulse to strike the sample) we can measure diffusive effects across the layered structure completing an accurate picture of the dynamics in the heterostructure.

APPENDIX A: Antenna Fabrication

Once the LTG-GaAs wafer which has a 1μm thick GaAs layer grown using Molecular Beam Epitaxy (MBE) is acquired, it is cleaved along the lattice to obtain small chips that will subsequently be patterned. Afterwards, they are cleaned using a four-step process which involves: TCE, Acetone, Iso-Propanol and Methanol. When this is completed the annealing process can be started.

Rapid Thermal Annealing(RTA): Place wafer in a special air-tight chamber, inject gas into the chamber at very high-temperatures, annealing takes place at about T~600C. After annealing we achieve τ (carrier lifetime) ~1ps, and very high mobility.

Before lithography, a .5μm coating of photoresist is applied onto each chip, which is accomplished by spinning the chip at a rate of 5000 revs/min. Then the chip is heated with the photoresist and placed under a quartz mask that has the shadow features. This mask already has the pattern we want on it, namely a 60μm separation width transmission line and 5μm separation width dipole structure. UV light is shined onto evaporate any unwanted photoresist.

Afterwards, the sample is developed in a chemical solution to completely get rid of unwanted photoresist. Then it is placed in an evaporator where layers of metal are deposited. These metals are a recipe of all or some of the following: Au, Ni, and Ge. Finally, the sample is placed in an acidic solution to remove all of the metal which is not bound to the LTG-GaAs.

APPENDIX B: Results on Other Nanocomposites-CNTs on Quartz, CNTs in Polymer on Quartz and Hexagonal Silicon on Quartz.

Here, results are shown for 3 new types of nanocomposite samples in a sample set of 6. 2 of them were carbon nanotubes (CNTs) grown either on quartz or in polymer on quartz, while the others were a blank sample (Quartz-only), and a blank sample with polymer and 2 sets of Hexagonal Silicon grown on quartz substrates. These samples were analyzed using a THz-TDS system so as to characterize their electrical properties. The following gives an outline of these efforts and shows preliminary results.

B.1 Overview

The data obtained on these samples were acquired with a newly built THz-TDS set-up, brought online during the months of June and July of 2004. This set-up is exactly the same configuration as the previous one (see Chapter 2) used to acquire the data on SWCNTs on quartz and Ion-Implanted Silicon nanoclusters in fused silica. One difference is the laser we use to generate the THz transients. Specifically, the Ti:Sapphhire laser is a *Spectra Physics Tsunami* with an output characteristic as obtained with an *ANDO* Optical Spectrum Analyzer of ~100fs pulses centered around λ=804nm. An example spectra obtained with this system is shown in Figure B.1. The other major difference between this set-up and the previous one is that the beam from the output of the mode-locked laser travels a much farther distance (~2m) before reaching the transmitter receiver pair of the THz-generation/detection part of the set-up. The beam

diverges quite rapidly and by the time this beam is doubled through the LBO (Lithium triborate) it's diameter is ~1cm, and even larger before the objectives used to focus the beam onto the dipole antenna. This could be an important factor that could translate as added noise on the antenna - resulting in minute fluctuations in the THz E-Field. This beam diameter is harder to estimate by eye do to its near-UV wavelength so an accurate comparison can not be made without measuring the beam profile. These above points should be taken into consideration when examining the spectra below.

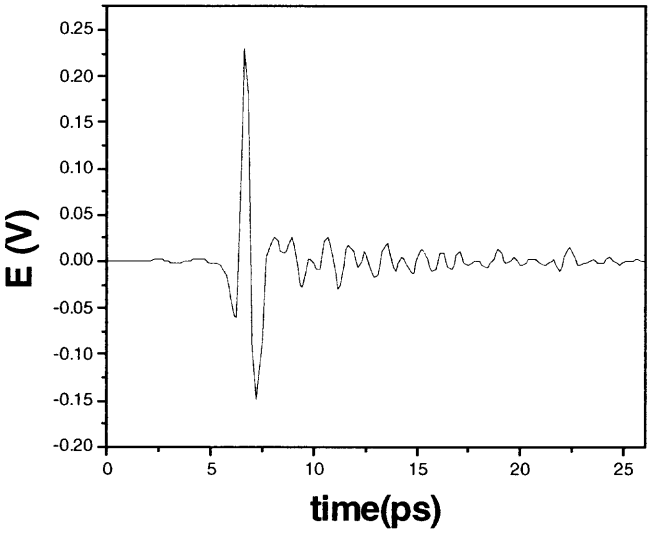

Figure B.1. THz through Air with the new set-up using ~100fs pulses from the Spectra-Physics *Tsunami Ti:Sapphire Laser* in B-15T.

B.2 Description of the Samples

Both CNT samples are assumed to be of the Single Wall variety. The difference being is that the ones grown on quartz are most probably in bundles while the ones grown in the

polymer are well separated (need SEM images to confirm). However, the CNT sample on quartz was pure black in color very similar in color to the MWCNT samples we previously had experimented on (see chapter 3), which suggests that it's not single wall but has multiwall tubes or contains a large amount of amorphous carbon. The CNTs in polymer were also dark, although since the CNTs were well dispersed this sample was still transparent to the eye. The original SWCNT sample for which we previously had seen results on was transparent to the eye. The Hexagonal-Silicon samples resemble a gold-like film on quartz. For all these samples, the substrate thickness was 1mm, and the nanomaterial layer thickness on top of the substrate was much less than the probing THz wavelength.

B.3 Experiments

Two types of experiments were done: THz-TDS under no visible excitation and visible pump/THz Probe spectroscopy. Figure B.2 and Figure B.3 show the THz transient field through each sample under no visible excitation, which was oriented at 45° with respect to probing THz radiation. This effectively reduces effects seen from Fabry-Perot type interference effects. As well, it enabled Visible-Pump/THz Probe spectroscopy to be performed so that the pump beam and the THz probe beam coincide at the same time on the nanomaterial surface.

From Figure B.2a, b we see that the THz field is far more attenuated compared to Figure B.2c, d. This is mainly due to the fact that the CNTs on quartz look much darker than the ones in the polymer. Comparatively, the transmission though hexagonal silicon

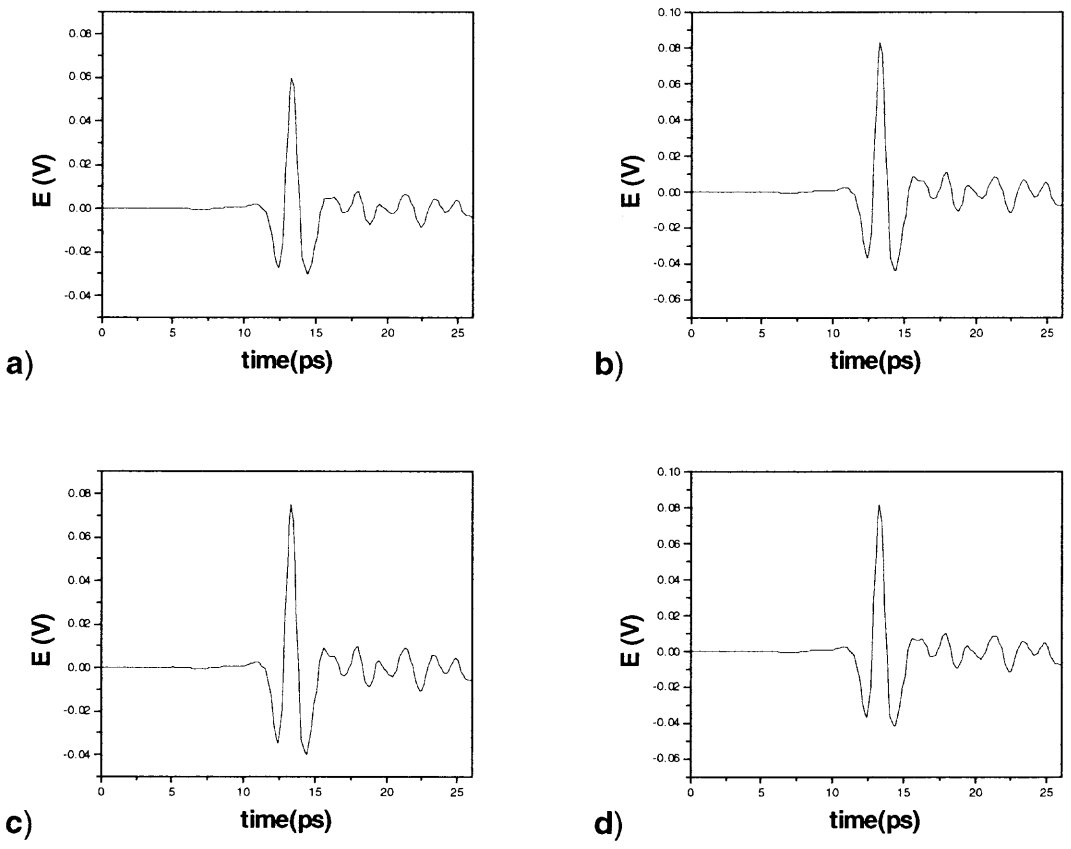

Figure B.2. THz E-field through the newly acquired CNT samples. a) CNTs on quartz, b) Quartz-only substrate, c) CNTs in polymer on quartz, d) Quartz-only Substrate with polymer.

was similar to that through quartz (Figure B.3).

All of the spectra was analyzed in the frequency domain and normalized to the transmission though the Quartz substrate (Figure B.4) to see any effects from 0.2 to 1 THz.

Before the samples could be examined under photo-excitation we had to find the point in time that both the THz Probe and visible pump pulse coincide. Again, as we had done previously, we accomplished this task with the aid of a piece of (LTG)-GaAs. And

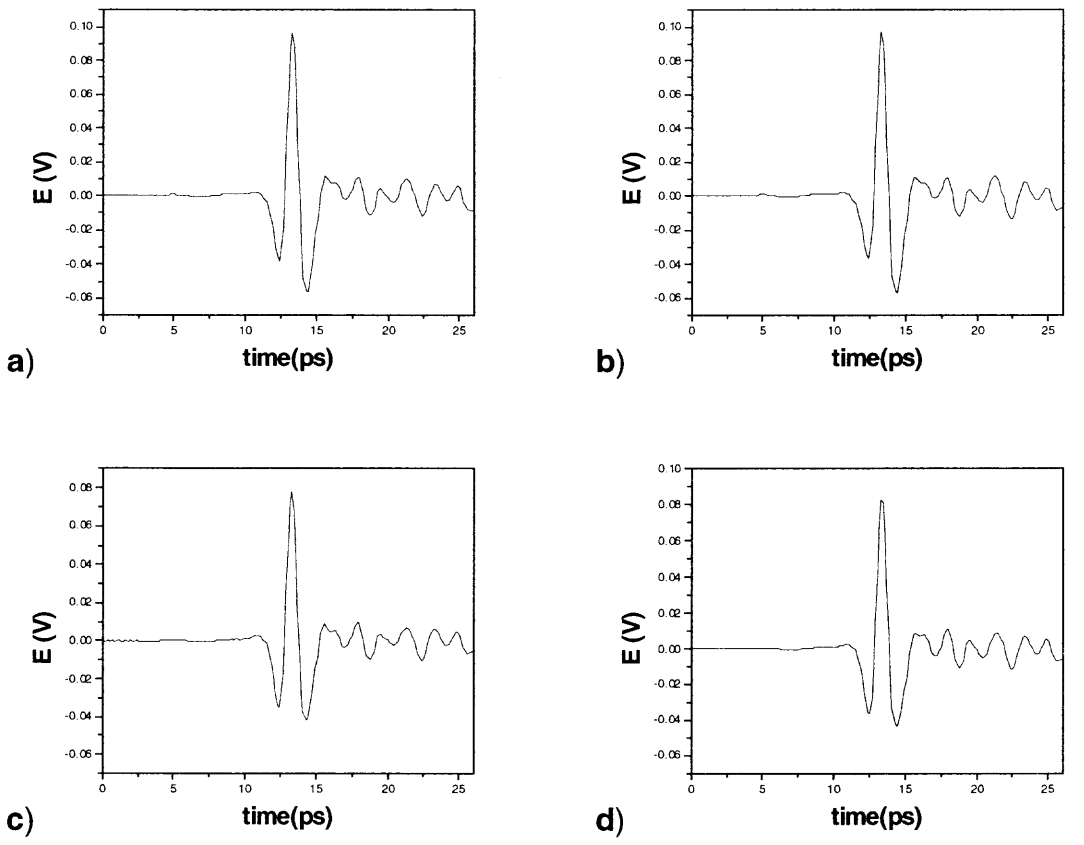

Figure B.3. THz E-field through the newly acquired Hexagonal Silicon samples on quartz. a) Hexagonal-Si on quartz, 1st measurement (Hex-Si A), b) Quartz-only substrate, c) Hex-Si on quartz, 2nd measurement (Hex-Si B), d) Quartz-only substrate.

compensated for the difference in thickness between this sample and the nanocomposites to predict the t = 0 point where the two pulses meet. The visible-pump beam diameter was ~1cm much larger than the THz probe beam diameter ~3mm.

The measurements done under photo-excitation were either an average of at least 3 scans where at each step the signal was integrated for at least 5 seconds though our digital lock-in or an average of 15 scans where at each step the signal was integrated for

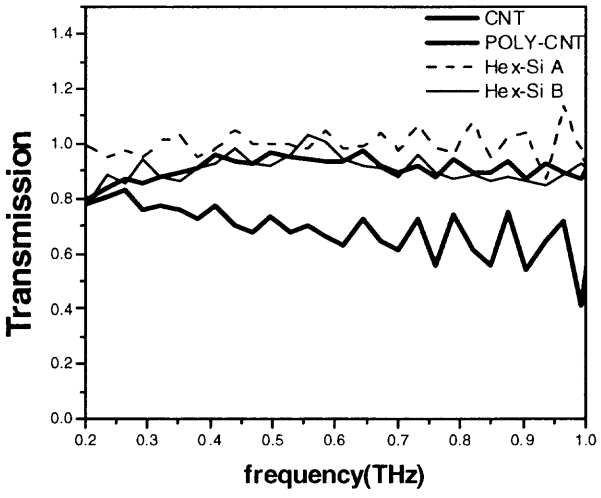

Figure B.4. Transmission under no visible pump through the CNTs on quartz (CNT) (lower solid curve) and in polymer on quartz (POLY-CNT) (upper solid curve) as well as two measurements for hexagonal silicon (Hex-Si A, Hex-Si B – upper dashed curves).

at least 1 second. The lock-in was referenced to the pump beam that was mechanically chopped at 2.5 kHz.

The measurements done in Figure B.5 show the change in the THz-E field with pump light on and off. This type of measurement is essentially like CW pumping since we always sit at the peak of the carrier generation and translate the THz probing picosecond pulse through this peak carrier density. Meaning if there is absorption due to free-carriers or bound charges we should observe the familiar shape of the THz-transient as was in Figures B.1, B.2, and B.3. As can be seen below, there was no response to the THz-probe pulse after visible pumping.

B.4 Analysis

Since the differential measurements did not reveal any information about the conductivity, we could only analyze the linear measurements (no visible excitation) as

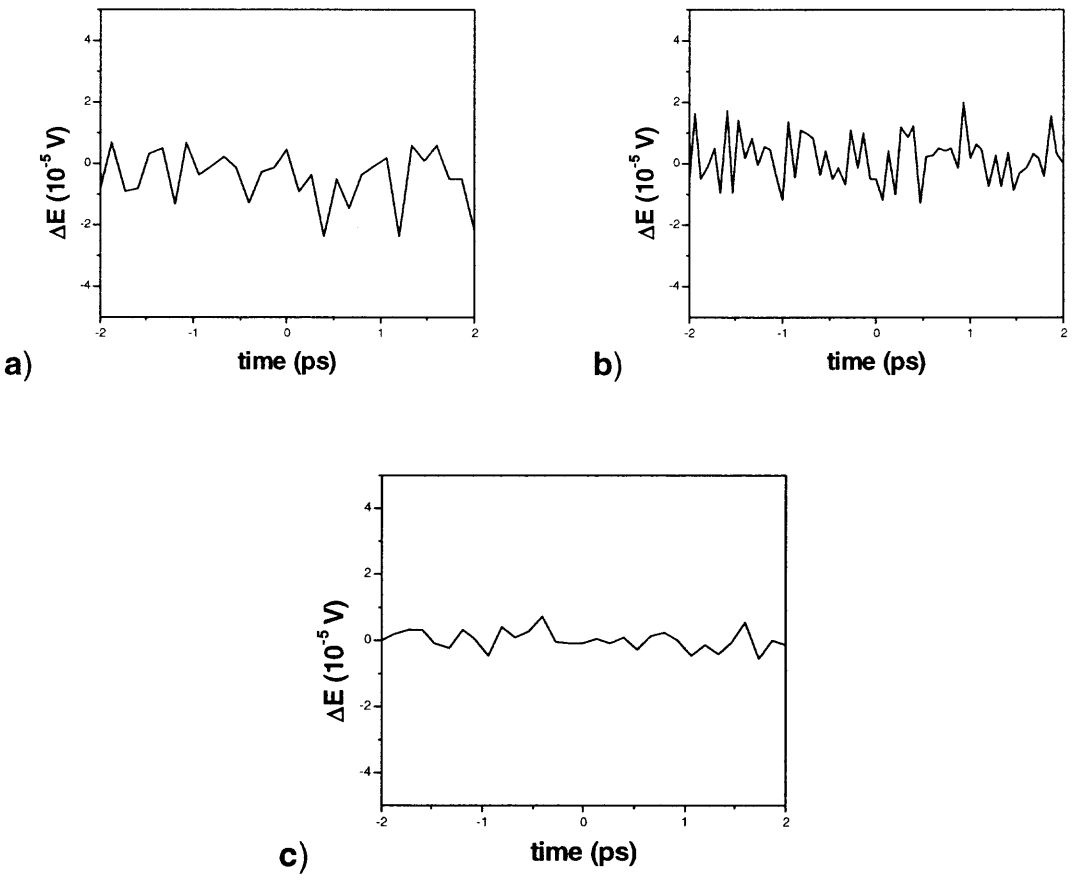

Figure B.5. Change in THz E-Field (pump on-pump off), pump pulses centered at λ=400 nm with Pav~35mW/cm^2 for a) CNTs on quartz, b) CNTs in polymer on quartz (shorter time-step), c) Hexagonal silicon on quartz.

shown in Figure B.4.

Barring a slight difference observed between the Hexagonal Silicon samples from both measurements, their transmission is nearly unity, which suggests that they hardly absorb any THz in our region of interest. This is also true for the CNTs in polymer. However, the CNTs on quartz show that the transmission is much less than the value of unity. While there are larger fluctuations at higher frequencies the linear decrease with higher frequency can not be easily explained. Either the medium is acting like a metal,

which would explain the large change from a transmission coefficient of unity (since the layer is so thin compared to the probing radiation) but would not explain the decrease at higher frequencies (if the linear decrease as observed in Figure B.4 is in fact true). Or the medium is acting like an insulator, for which there is a broad absorption at a frequency beyond our observable range. And since the visible pump/THz probe measurements reveal nothing it is difficult to say.

Another explanation could be that there are chemicals left over from the manufacturing processes which could absorb the THz at higher frequencies. These chemicals would have to be individually tested for such effects.

B.5 Discussion

THz-TDS under no excitation and Visible Pump/THz Probe experiments were performed on Hexagonal Silicon, CNTs, and CNTs in Polymer, all on quartz. Visible Pump/THz probe measurements revealed no evidence for absorption in our frequency range of interest (0.2 to 1 THz). Linear (unpumped) measurements showed that the transmission through hexagonal silicon, and CNTs in polymer were fairly flat, while the transmission through CNTs on quartz decreased towards higher frequencies. This decrease could be either due to the CNTs or to leftover chemicals or soot from the manufacturing process. The large difference between the CNTs in polymer and the CNTs on quartz is due to the relatively larger density of CNTs in the non-polymer sample as can be deduced by eye (the relative darkness of each sample). In future studies, these attributes could be further investigated.

REFERENCES

[1] de Pablo, P.J., Martínez, M.T., Colchero, J., Gómez-Herrero, J., Maser, W.K., Benito, A.M., Muñoz, E., and Baró, A.M, "Mechanical and Electrical Properties of Nanosized Contacts on Single-Walled Carbon Nanotubes," Advanced Materials, 12 (8), 573 – 576 (2000).

[2] Dai, H., Franklin, N., and Han, J., "Exploiting the Properties of Carbon Nanotube For Nanolithography," Appl. Phys. Lett., 73, 1508 (1998).

[3] Collin, R. E., "Field Theory of Guided Waves," (2nd Ed.). Series Ed., Dudley, D., The IEEE Press Series on Electromagnetic Theory, Wiley-Interscience-IEEE, New York, NY, 749-782 (1990).

[4] Stooky, S.D. and Araujo, R.J., "Selective polarization at light due to absorption by small elongated silver particles in glass," Applied Optics, 71, 777-779.(1968).

[5] Borrelli, N., Chodak, J.B., and Hares, G.B., "Optically induced anisotropy in photochromic glasses," Journal of Applied Physics, 50, 5978 (1985).

[6] Kaiser W.J., Logothetis, E.M, and Wegner, L.E., "Dielectric properties of small metal particle composites," J. Phys. C, 181, L837-L842 (1985).

[7] Lee S., Noh T.W., Gaines J.R., Ko Y., and Kreidler E.R., "Optical studies of porous glass media containing silver particles," Phys. Rev. B, 37, 2918 (1988).

[8] Barrera, R.G., Monsivais, G. and Mochan, L.W., "Renormalized polarizability in the Maxwell Garnett theory," Phys. Rev. B, 38, 5371 (1988).

[9] Grebel, H. and Chen, P., "Artificial dielectric polymeric waveguides: metallic embedded films," J. Opt. Soc. Am. 8, 615 (1991).

[10] Federici, J.F., and Grebel, H., "Characteristics of Nano-Scale Composites at THz and IR Spectral Regions," to appear in Sensing Science and Technology at THz Frequencies, Volume II. Emerging Scientific Applications & Novel Device Concepts, ed. D. Woodard, M. Shur, and W. Loerop (2003).

[11] Hu, B., de Souza, E.A., Knox, W.H., Cunningham, J.E., Nuss, M.C., Kuznetsov, A.V., and Chang, S.L., "Identifying the distinct phases of carrier transport in semiconductors with 10 fs resolution," Phys. Rev. Lett., 74, 1689 (1995).

[12] Vijayalakshmi, S., George, M., and Grebel, H., "Non-linear optical properties of silicon nanoclusters," Appl. Phys. Letts., 70(6), 708 (1997).

[13] Vijayalakshmi, S., Grebel, H., Iqbal, Z., and White, C.W., "Artificial dielectrics; non-linear properties of Si nano clusters formed by ion implantion in SiO_2 glassy matrix," J. Appl. Phys., 84, 6502 (1998).

[14] Iqbal, Z., Vijayalakshmi, S., Grebel, H., and White, C.W., "Microstructure and optical properties of nanostructured silicon thin films and artificial dielectrics," Nanostructured Materials, 12, 271 (1999).

[15] Kuzel, P. and Petzelt, J., "Time-resolved terahertz transmission spectroscopy of dielectrics," Ferroelectrics, 239 (1-4), 949-956 (2000).

[16] Kindt, J.T., and Schmuttenmaer, C.A., "Far-infrared dielectric properties of polar liquids probed by femtosecond terahertz pulse spectroscopy," J. Phys. Chem., 100 (24), 10 373-10 379 (1996).

[17] Harde, H., Katzenellenbogen, N., and Grischkowsky, D., "Terahertz coherent transients from methyl chloride vapour," J. Opt. Soc. Am. B, 11 (6), 1018-1030 (1994).

[18] van der Weide, D.W., "Electronic Sources and Detectors for Wideband Sensing in the Terahertz Regime," in *Sensing with Terahertz Radiatio*n, 85, Springer Series in Optical Sciences, D. M. Mittleman, Ed.: Springer, (2003).

[19] Mueller, E.R., "Submillimeter Wave Lasers," Wiley Encyclopedia of Electrical and Electronics Engineering, Volume 20, Editor: J. G. Webster, John Wiley & Sons, Inc., 597 – 615 (1999).

[20] Hovenier, J.N., de Kleijn, R.M., Klaassen, T.O., Wenckebach, W.T., Chamberlin, D.R., Bründermann, E., and Haller, E.E., "Mode-locked operation of the copper-doped germanium terahertz laser," Appl. Phys. Lett., 77, 3155-3157 (2000).

[21] Auston, D.H., Cheung, K.P., and Smith, P.R., "Picosecond photoconducting Hertzian dipoles," Appl. Phys. Lett., 45 (3), 284-286 (1984).

[22] Xu, L., Zhang, X.C., and Auston, D.H., "Terahertz beam generation by femtosecond optical pulses in electrooptic materials," Appl. Phys. Lett., 61 (15), 1784-1786 (1992).

[23] Leitenstorfer, A., Hunsche, S., Shah, J., Nuss, M.C., and Knox, W.H., "Detectors and sources for ultrabroadband electro-optic sampling: Experiment and theory," Appl. Phys. Lett., 74 (11), 1516-1518 (1999).

[24] Planken C. P. M., Nuss, M. C., Knox, W. H., Miller, D. A. B., and Goosen K. W., "THz pulses from the creation of polarized electron hole pairs in biased quantum wells," Appl. Phys. Lett., 61, 2009-2011 (1992).

[25] Prabhu, S.S., Ralph, S.E., Melloch, M.R., and Harmon, E.S., "Carrier dynamics of low-temperature-grown GaAs observed via THz spectroscopy," Appl. Phys. Lett., 70 (18), 2419-2421 (1997).

[26] Beard, M.C., Turner, G.M., and Schmuttenmaer, C.A., "Transient photoconductivity in GaAs as measured by time-resolved terahertz spectroscopy," Phys. Rev. B, 62 (23), 15 764-15 777 (2000).

[27] van Exter, M., and Grischkowsky, D., "Optical and electronic properties of doped silicon from 0.1 to 2 THz," Appl. Phys. Lett., 56 (17), 1694-1696 (1990).

[28] Saeta, P.N., Federici, J.F., Greene, B.I., and Dykaar, D.R., "Intervalley scattering in GaAs and InP probed by pulsed far-infrared transmission spectroscopy," Appl. Phys. Lett., 60 (23), 1477-1479 (1992).

[29] Nuss, M.C., Mankiewich, P.M., O'Malley, M.L., and Westerwick, E.H., "Dynamic conductivity and "coherence peak" in YBa2Cu3O7 supercondoctors," Phys. Rev. Lett., 66 (25), 3305-3308 (1991).

[30] Jeon, T.I., Grischkowsky, D., Mukherjee, A.K., and Menon, R., "Electrical characterization of conducting polypyrrole by THz time-domain spectroscopy," Appl. Phys. Lett., 77 (16), 2452-2454 (2000).

[31] Harde, H., Katzenellenbogen, N., and Grischkowsky, D., "Terahertz coherent transients from methyl chloride vapour," J. Opt. Soc. Am. B, 11 (6), 1018-1030 (1994).

[32] Cheville, R.A., and Grischkowsky, D., "Far-infrared terahertz time-domain spectroscopy of flames," Opt. Lett., 20 (15), 1646-1648 (1995).

[33] Zhang, X.C., Hu, B.B., Darrow, J.T., and Auston, D.H., "Generation of femtosecond electromagnetic pulses from semiconductor surfaces," Appl. Phys. Lett., 56 (11), 1011-1013 (1990).

[34] Mitrofanov, O., "Near-Field Imaging with THz pulses," Dissertation, NJIT, Newark, NJ (2001)

[35] Cai, Y., "Enhanced terahertz pulse generation and detection using electric-field singularities in photo-conducting antennas," Dissertation, NJIT, Newark, NJ (1998).

[36] Hummel, R.E., "Electronic Properties of Materials," 2nd Ed, Springer-Verlag (2003).

[37] Nemec, H., "Application of methods in time-domain terahertz spectroscopy for investigation of ultrafast dynamics in condensed matters," Diploma Thesis, Charles University in Prague, Czech Republic (2002).

[38] Planken, P.C.M., Nuss, M.C., Brener, I., and Goossen, K.W., "Terahertz emission in single quantum wells after coherent excitation of light hole and heavy hole excitons," Phys. Rev. Lett., 69 (26), 3800-3803 (1992).

[39] Zhang, X.C., and Auston, D.H., "Optoelectronic measurement of semiconductor surfaces and interfaces with femtosecond optics," J. Appl. Phys., 71 (1), 326-338 (1992).

[40] Kersting, R., Unterrainer, K., Strasser, G., Kaufmann, H.F., and Gornik, E., "Few cycle THz emission from cold plasma oscillations," Phys. Rev. Lett., 79 (16), 3038-3041 (1997).

[41] McLaughlin, R., Corchia, A., Johnston, M.B., Chen, Q., Ciesla, C.M., Arnone, D.D., Jones, G.A.C., Linfield, E.H., Davies, A.G., and Pepper, M., "Enhanced coherent terahertz emission from indium arsenide in the presence of a magnetic field," Appl. Phys. Lett., 76 (15), 2038-2040 (2000).

[42] Beard, M.C., Turner, G.M., and Schmuttenmaer, C.A., "Sub-picosecond carrier dynamics in low-temperature grown GaAs as measured by time-resolved THz spectroscopy." J. Appl. Phys., 90, 5915-5923 (2001).

[43] Beard, M.C., and Schmuttenmaer, C.A., "Using the Finite-Difference Time-Domain Pulse Propagation Method to Simulate Time-Resolved THz Experiments" J. Chem. Phys., 114, 2903 (2001).

[44] Woolard, D., Globus, T., Brown, E., Werbos, L., Gelmont, B., and Samuels, A., "Sensitivity limits and discrimination capability of THz transmission spectroscopy as a technique for biological agent detection," Proceedings to the 5th Joint Conference on Standoff Detection for Chemical and Biological Defense, Williamsburg, PA (2001).

[45] Mittleman, D.M., Gupta, M., Neelamani, R., Baraniuk, R.G., Rudd, J. V., and Koch, M., "Recent Advances in THz Imaging," Appl. Phys. B, 68, pp1085-1094 (1999).

[46] van Exter, M., Fattinger, C. and Grischkowsky, D., "TeraHz Time Domain Spectroscopy of Water Vapor", Optics Letters, Vol.14, 1128-1130 (1989).

[47] Markelz, A.G., Roitberg A., and Heilwell, E. J., "Pulsed THz Spectroscopy of DNA, bovine serum albumin and collagen between 0.1 and 2THz," Chem. Phys. Lett., 320, 42-48 (2000).

[48] Beard, M.C., Turner, G.M., Murphy, J.E., Micic, O.I., Hanna, M.C., Nozik, A.J., and Schmuttenmaer, C.A., "Electronic coupling in InP nanoparticle arrays," Nano Lett., 3, 1695 (2003).

[49] Drexler, K. E., "Molecular engineering: An approach to the development of general capabilities for molecular manipulation," Proc. Natnl. Acad. Sci. U.S.A., 78, 5275-5278 (1981).

[50] S. Fafard, R. Leon, D. Leonard, J.L.Merz, P.M. Petroff, "Visible photoluminescence from n-dot ensembles and the linewidth of ultrasmall AlInAs/AlGaAs quantum dots," Phys. Rev. B, 50, 8086 (1994).

[51] Kakkad, R., Smith, J., Lau, W.S., Fonash, S.J., and Kerns, R., "Crystallized Si films by low-temperature rapid thermal annealing of amorphous silicon," J. Appl. Phys., 65, 2069–2072 (1989).

[52] Searle, T.M., (Ed.), "Properties of Amorphous Silicon and its Alloy," EMIS Datareview Series, IEE, UK (1998).

[53] Pulickel M. Ajayan, Linda S. Schadler, Paul V. Braun, "Nanocomposite Science and Technology", Wiley, New York, NY (2003).

[54] Hilt, O., Brom, H.B., and Ahlskog, M., "Localized and delocalized charge transport in single-wall carbon-nanotube mats," Phys. Rev. B 61, 5129 (2000).

[55] Han, J., Zhu, Z., Liao, Y., Wang, Z., Yu, L., Zhang, L., Sun, L., and Wang, T., "Optical Conductivity of Single Walled Nanotube Films in the Terahertz Region," JETP Lett. 78, 904 (2003).

[56] Jeon, T., Kim, K., Kang, C., Oh, S., Son, J., An, K.H., Bae, D.J., Lee, Y.H., "Terahertz conductivity of anisotropic single walled carbon nanotube films," Appl. Phys. Lett. 80, 3403 (2002).

[57] Jepsen, U. P., Schairer, W., Libon, H. I., Lemmer, U., Hecker, E. N., Birkholz, M., Lips, K., and Schall, M., "Ultrafast carrier trapping in microcrystalline silicon observed in optical pump–terahertz probe measurements," Appl. Phys. Lett. 79, 9, 1291-1293 (2001).

[58] Beard, M.C., Turner, G.M., and Schmuttenmaer, C.A., "Sub-picosecond carrier dynamics in low-temperature grown GaAs as measured by time-resolved THz spectroscopy," J. Appl. Phys. 90, 5915 (2001).

[59] Kroto, H.W., Heath, J.R., O'Brien, S.C., Curl, R.F.,and Smalley, R.E., "C60: Buckminsterfullerene", Nature, 318, 162-163 (1985).

[60] Iijima, S., "Helical microtubules of graphitic carbon", Nature, 345, 56-58 (1991).

[61] Liu, Y, Jones, O. R., Zhao, X., and Ando, Y., "Carbon species confined inside carbon nanotubes: A density functional study," Phys. Rev. B. 68, 5413 (2003).

[62] Salvetat-Delmotte, J., Rubio, A., "Mechanical properties of carbon nanotubes: a fiber digest for beginners," Carbon 40, 1729-1734 (2001).

[63] Dresselhaus, M. S., Dresselhaus, G., and Eklund, P. C., "Science of Fullerenes and Carbon Nanotubes," Academic Press, San Diego (1996).

[64] Li, J., Stevens, R., Delzeit, L., Ng, H.T., Cassell, A., Han, J., and Meyyappan, M., "Electronic properties of multiwalled carbon nanotubes in an embedded vertical array," Appl. Phys. Lett. 81, 5, 910-912 (2002).

[65] Ebbesen, T W., Ajayan, P. M., "Large-scale synthesis of carbon nanotubes", Nature 358 (1992).

[66] Endo, M., "Grow carbon fibres in the vapour phase," Chemtech 18, 568 (1988).

[67] Endo, M., Takeuchi, K., Kobori, K., Takahashi, K., Kroto, H.W., and Sarkar, A., "Pyrolytic carbon nanotubes from vapor-grown carbon fibers," Carbon 33, 873 (1995).

[68] Thess, A., Lee, R., Nikolaev, P., Hongjie, D., Petit, P., Robert, J., Xu, C., Lee. Y. H., Kim, S. G., Rinzler, A. G., Colbert, D. T., Scuseria, G. E., Tománek, D., Fischer, J. E., Smalley, R. E., "Crystalline Ropes of Metallic Carbon Nanotubes," Science 273, 483 (1996).

[69] Rao, A.M., Chen, J., Richter, E., Schlecht, U., Eklund, P.C., Haddon, R.C., Venkateswaran, U.D., Kwon, Y.-K., and Tománek, D., "Effect of van der Waals Interactions on the Raman Modes in Single Walled Carbon Nanotubes," Appl. Phys. Lett. 86(17), 3895-3898 (2001).

[70] Lambin, P. H., Fonseca, A., Vigneron, J. P., Nagy, J. B., Lucas, A. A., "Structural and electronic properties of bent carbon nanotubes," Chem. Phys. Lett. 245 (1995).

[71] Ugawa, A., Rinzler, A.G., and Tanner, D.B., "Far-infrared gaps in single-wall Carbon nanotubes," Phys. Rev. B, 60, R11305 (1999).

[72] Ugawa, A., Hwang, J., Gommans, H.H., Tashiro, H., Rinzler, A.G., and Tanner, D.B., "Far-infrared to visible optical conductivity of single-wall Carbon nanotubes," Curr. Appl. Phys. 1, 45-49 (2001).

[73] Itkis, M.E., Niyogi, S., Meng, M.E., Hamon, M.A., Hu, H., and Haddon, R.C., "Spectroscopic Study of the Fermi Level Electronic Structure of Single-Walled Carbon Nanotubes," Nano. Lett. 2(2), 155-159 (2002).

[74] Kittel, C., "Quantum Theory of Solids", 2nd Revised Edition, Wiley, New York, NY (1987).

[75] Lebedkin, S., Arnold, K., Hennrich, F., Krupke, R., Renker, B., and Kappes, M.M., "FTIR-luminescence mapping of dispersed single-walled carbon nanotubes," New J. Phys. 5, 140 (2003).

[76] Hertel, T., Fasel, R., and Moos, G., "Charge-carrier dynamics in single-wall carbon nanotube bundles: a time-domain study," Appl. Phys. A 75, 449–465 (2002).

[77] Ghosh, S., Teredesai, P.V., and Sood, A.K., "Electrochemical tuning and mechanical resilience of single-wall carbon nanotubes," Pure Appl. Chem. 74(9), 1719 –1730 (2002).

[78] Xin, Z., Jianjun, Z., and Zhong-can, O.-Y., "Strain energy and Young's modulus of single-wall carbon nanotubes calculated from electronic energy-band theory." Physical Review B 32, 13692 (2000).

[79] Yildirim, T., Gulseren, O., Kiliç, and Ciraci., S., "Pressure-induced interlinking of carbon nanotubes," Physical Review B 62(19), 12648-12651 (2000).

[80] Lammert, P.E., Zhang, P., and Crespi, V.H., "Gapping by Squashing: Metal-Insulator and Insulator-Metal Transitions in Collapsed Carbon Nanotubes," Phys. Rev. Lett. 84, 11, 2453-2456 (2000).

[81] Borondics, F., Kamaras, K., Chen, Z., Rinzler, A.G., Nikolou, M., and Tanner, D.B., "Infrared Transmittance of free-standing single-wall Carbon nanotube films," XVIIth International Winter School on Electronic Properties of Novel Materials (2003).

[82] Lauret, J.S., Voisin, C., Cassabois, G., Roussignol, P., Delande, C., Capes, L., Valentin, E., Filoramo, A., Jost, O., "Photocreated carrier dynamics in isolated carbon nanotubes," Semicond. Sci. Technol. 19, S486-S488 (2004).

[83] Lan, A., Iqbal, Z., Aitouchen, A., Libera, M., Grebel, H., "Growth of single-wall carbon nanotubes within an ordered array of nanosize silica spheres," Appl. Phys. Lett., 81, 433 (2002).

[84] Fiory, A.T., Ravindra, N.M., "Light Emission from Silicon: Some Perspectives and Applications," J. Elec. Mat. 32, 1043 (2003).

[85] Dexheimer, S.L., and Lynn, K.G., "Novel Characterization Methods for Microcrystalline Silicon," NREL/SR-520-34949 (2003).

[86] Klimov, V.P., Schwarz, Ch. J., McBranch, D.W., and White, C.W., "Initial carrier relaxation dynamics in ion-implanted Si nanocrystals: Femtosecond transient absorption study," Appl. Phys. Lett. 73, 18, 2603 (1998).

[87] Grebel, H., Iqbal, Z., and Lan, A., "Detecting single-wall carbon nanotubes with surface-enhanced Raman scattering from metal-coated periodic structures," Chem. Phys. Lett. 348, 203 (2001).

[88] Han, H., Vijayalakshmi, S., Lan, A., Iqbal, Z., Grebel, H., Lalanne, E., and Johnson, A.M., "Linear and nonlinear optical properties of single-walled carbon nanotubes within an ordered array of nanosized silica spheres," Appl. Phys. Lett. 82, 1458 (2003).

[89] "Structure and Imperfections in Amorphous and Crystalline Silicon Dioxide," Ed. By R. A. B. Devine, J.-P. Duraud, E. Dooryhee, Semiconductors Series, Wiley, New York (2000).

[90] Vijayalakshmi, S., Grebel, H., Yaglioglu, G., Pino, R., Dornsville, R., White, C.W., "Nonlinear optical response of Si nanostructures in a silica matrix," J. Appl Phys. 88, 6418 (2000).

[91] Cohen, R.W., Cody, G.D., Coutts, M.D., Abeles, B., "Optical Properties of Granular Silver and Gold Films," Phys. Rev. B 8, 3689 (1973).

[92] Altan, H., Huang, F., Federici, J., Lan, A., and Grebel, H., "Characteristics of Nanocomposites by THz Spectroscopy," Proc. SPIE Vol. 5070, 53 (2003).

[93] Beard, M.C., Turner, G.M., and Schmuttenmaer, C.A., "Size-dependent photoconductivity in CdSe nanoparticles as measured by time-resolved terahertz spectroscopy," Nano Lett. 2, 983-987 (2002).

[94] Jeon, T., Kim, K., Kang, C., Maeng, I.H., Son, J., An, K.H., Lee, J.Y., and Lee, Y.H., "Optical and electrical properties of preferentially anisotropic single-walled carbon-nanotube films in terahertz region," J. Appl. Phys. 95, 5736-5740 (2004).

[95] Dürkop, T, Getty, S.A., Corbas, E., Fuhrer, M.S., "Extraordinary Mobility in Semiconducting Carbon Nanotubes," Nano Lett., 4, 35-39 (2004).

[96] Born, M., and Wolfe, E., "Principles of optics," *7th Ed*, Cambridge University Press, New York (1999).

[97] Sze, S.M., "VLSI Technology," 2nd Edition, McGraw Hill-New York (1988).

[98] Efros, A. L. and Efros, Al. L., "Interband absorption of light in a semiconductor sphere," Sov. Phys. Semicond. 16, 772-775 (1982).

[99] Brus, L. E., "Electron-electron and electron-hole interaction in small semiconductor crystallites. The size dependence of the lowest excited electronic state," J. Chem. Phys. 80, 4403-4409 (1984).

[100] Rao, A.M., Chen, J., Richter, E., Schlecht, U., Eklund, P.C., Haddon, R.C., Venkateswaran,U.D., Kwon, Y.K., and Tománek, D., "Effect of van der Waals Interactions on the Raman Modes in Single Walled Carbon Nanotubes," Phys. Rev. Lett. 86, 3895 (2001).

[101] Dresselhaus, M.S., Dresselhaus, G., Pimenta, M.A., Eklund, P.C., "Raman Scattering in Carbon Materials, in Analytical Applications of Raman Spectroscopy", M.J. Pelletier, Editor. Blackwell Science Ltd: Oxford, 367-434 (1999).

[102] Katzenellenbogen, N. and D. Grischkowsky, "Electrical Characterization to 4 THz of N and P Type GaAs Using THz Time-Domain Spectroscopy," Appl. Phys. Lett. 61, 840-842 (1992).

[103] Grischkowsky, D., Keiding, S., van Exter, M., and Fattinger, C., "Far-Infrared Time-Domain Spectroscopy with Terahertz Beams of Dielectrics and Semiconductors," JOSA-B 7, 2006-2015 (1990).

[104] Heyman, J.N., Neocleous, P., and Hebert, D., Crowell, P.A, Mueller, T., and Unterrainer, K., "Terahertz emission from GaAs and InAs in a magnetic field," Phys. Rev. B 64, 085202 (2001).

[105] Shimano, R., Ino, Y., Svirko, Y.P., and Kuwata-Gonokami, M., "Terahertz frequency Hall measurement by magneto-optical Kerr spectroscopy in InAs," Appl. Phys. Lett. 58, 199-201 (2002).

[106] Zhang, W., Azad, A.K., and Grischkowsky, D., "Terahertz studies of carrier dynamics and dielectric response of n-type, freestanding epitaxial GaN," Appl. Phys. Lett. 82, 2841-2843 (2003).

[107] Jeon, T., and Grischkowsky, D., "Characterization of Optically-Dense, Doped Semiconductors by Reflection THz Time-Domain Spectroscopy," Appl. Phys. Lett. 72, 3032-3034 (1998).

[108] Hashimshony, D., Geltner, I., Cohen, G., Avitzour, Y., Zigler, A., and Smith, C., "Characterization of the electrical properties and thickness of thin epitaxial semiconductor layers by THz reflection spectroscopy," Appl. Phys. Lett. 90, 5778-5781 (2001).

[109] Zhang, X.-C., and Auston, D.H., "Optoelectronic measurement of semiconductor surfaces and interfaces with femtosecond optics," J. Appl. Phys. 71 (1), 326-338 (1992).

[110] Inoue, K., Sakaki, H., "A New Highly-Conductive (AlGa)As/GaAs/(AlGa)As Selectively-Doped Double-Heterojunction Field-Effect Transistor (SD-DH-FET)," Jap. J. Appl. Phys 23, L61 (1984).

[111] Hoyt, J.L., Nayef, H.M., Eguchi, S., Aberg, I., Xia, G., Drake, T., Fitzgerald, E.A., Antoniadis, D.A., "Strained Silicon MOSFET Technology", IEDM Tech. Digest, p. 23 (2002).

[112] Richard, S., Aniel, F., Fishman, G., "Energy-band Structure in strained silicon: A 20-band K.P and Bir-Pikus Hamiltonian model," J. of Appl. Phys. 94, 3 (2003).

[113] Ismail, K., Nelson, S.F., Chu, J.O., and Meyerson, B.S., "Electron transport properties of Si/SiGe heterostructures: Measurements and device implications," Appl. Phys. Lett. 63, 660-662 (1993).

[114] Lee, M.L., Leitz, C.W., Cheng, Z., Pitera, A.J., Langdo, T., Currie, M.T., Taraschi, G., Fitzgerald, E.A., and Antoniadis, D.A., "Strained Ge channel p-type metal–oxide–semiconductor field-effect transistors grown on $Si_{1-x}Ge_x$/Si virtual substrates," Appl. Phys. Lett. 79, 3344-3346 (2001).

[115] Wong, H.-S.P., "Beyond the Conventional Transistor", IBM J. Res. & Dev. 46, 2/3 (2002).

[116] Lin, Y.-S., Puthenkovilakam, R., and Chang, J.P., "Dielectric property and thermal stability of HfO2 on silicon," Appl. Phys. Lett. 81, 2041-2043 (2002).

[117] "Properties of Silicon Germanium and SiGe: carbon,"Edited by Erich Kasper and Klara Lyutovich, The Electronic Materials Information Service (EMIS), IEE (1999).

[118] National Compound Semiconductor Roadmap (NCSR)-SiGe, Site details properties of SiGe. Retrieved October 1, 2004, from http://www.onr.navy.mil/sci_tech/information/312_electronics/ncsr/materials/sige.asp

[119] Patrini, M., Galli, M., Belotti, M., Andreani, L.C., Guizzetti, G., Pucker, G., Lui, A., Bellutti P., and Pavesi, L., "Optical response of one-dimensional $(Si/SiO_2)_m$ photonic crystals," J. Appl. Phys. 92, 1816-1820 (2002).

[120] Seshadri, S.R., "Fundementals of Transmission Lines and Electric Fields," p. 292, Addison-Wesley Pub. Co., (1971).

[121] Gusev, E.P., and D'Emic, C.P., "Charge detrapping in HfO_2 high- k gate dielectric stacks," Appl. Phys. Lett., 83, 5223-5225 (2003).

[122] Gusev, E.P., Buchanan, D.A., Cartier, E., Kumar, A., DiMaria, D., Guha, S., Callegari, A., Zafar, S., Jamison, S., Neumayer, D., Copel, M., Gribelyuk , M.A., Okorn-Schmidt, H., D'Emic, C.P., Kozlowski, P., Chan, K., Bojarczuk, N., Ragnarsson, L.-A., Ronsheim, P., Rim, K., Fleming, R.J., Mocuta, A., and Ajmera, A., "Ultrathin high-K gate stacks for advanced CMOS devices," IEDM Technical Digest (2001).

[123] Jomaah, J., Ghibaudo, G., Cristoloveanu, S., and Balestra, F., "Electrical Performances at low temperature of ultimate Si-based MOSFETs," Abs. 891, 204th Meeting, The Electrochemical Society, Inc. (2003).

[124] Schroder, D.K., "Carrier Lifetimes in Silicon," IEEE Transactions on Electron Devices 44, no. 1 (1997).

[125] Passlack, M., Zu, Y, et al., "Interface Charge and non-radiative carrier recombination...etc.," J. Vac, Sci. Tech. B., 17, 49 (1999).

[126] Jayakumar, R., Zeater, K., Ali, S., Gharghi, M., Stevens, G., Hammerbacher, M., and Sivoththaman, S., "Low thermal budget PECVD Silicon Nitride Passivation of Crystalline Silicon Devices," Eleventh Canadian Semiconductor Technology Conference,TP.48 (2003).

[127] Klein, P.B., Binari, S.C., Freitas Jr., J.A., and Wickenden, A.E., "Photoionization spectroscopy of traps in GaN metal-semiconductor field-effect transistors," J. Appl. Phys. 85(5), 2843 (2000).

[128] Schroder, D.K., "Trends in Lifetime Measurements," High Purity Silicon VI, C.L.Claeys, P. Rai-Choudhury, M. Watanabe, P. Stallhofer, and H.J. Dawson, eds., Electrochem. Soc., Pennington NJ, ECS PV2000-17, 365-382 (2000).

[129] Pankove, J. S., "Optical Processes in Semiconductors," Dover Publications Inc., New York (1971).

[130] Gilmore, A.S., Al-Kaoud, A., Kaydanov, V. and Ohno, T.R., "Mobility in SnO2:F Thin polycrystalline Films: Grain Boundary Effect and Scattering in the Grain Bulk," Proc. Spring Mat. Res. Soc. Symp., (2001).